MSc in Astrophysics

Exploring Demographic Drift of Type Ia SNe and its Impact on Cosmology

Jacob Osman Hjortlund

Supervised by Dr. Radoslaw Wojtak

August 2023

Jacob Osman Hjortlund
Exploring Demographic Drift of Type Ia SNe and its Impact on Cosmology
MSc in Astrophysics, August 15th, 2023
Supervisors: Dr. Radoslaw Wojtak
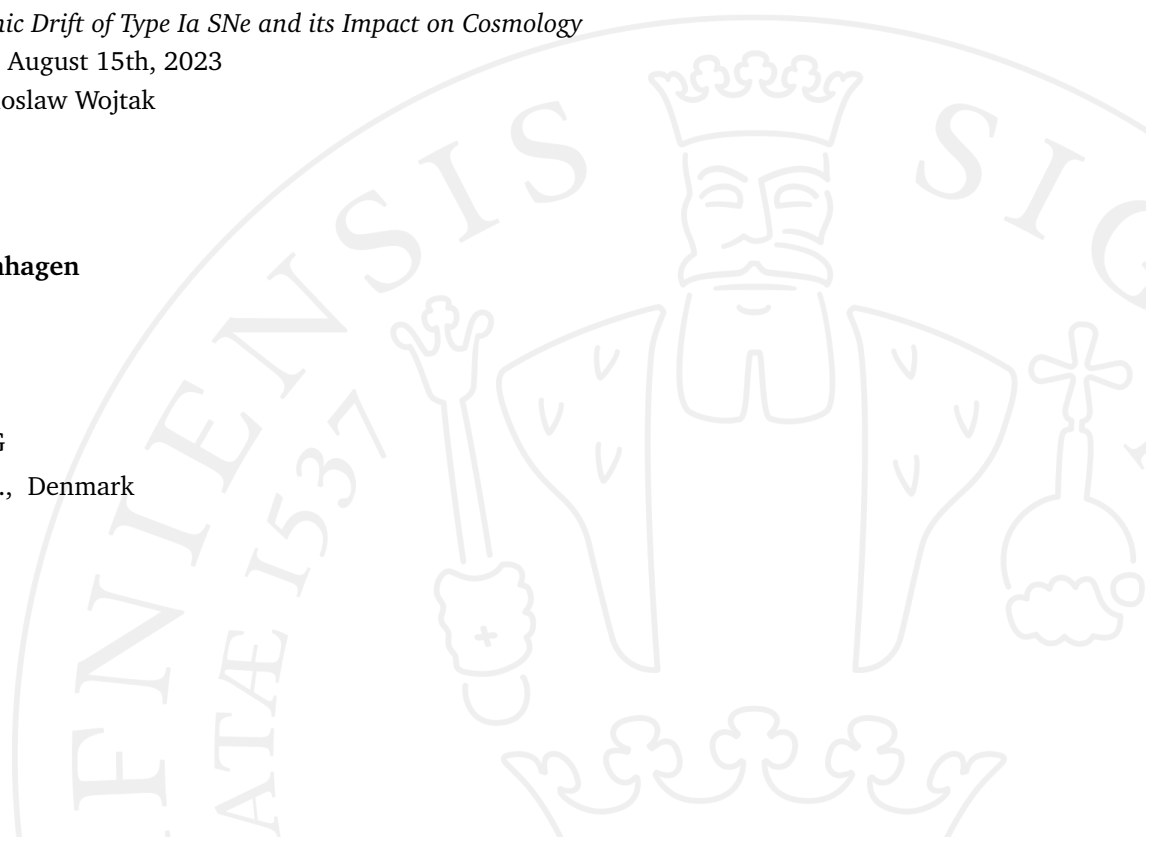

University of Copenhagen

Faculty of Science

Niels Bohr Institute

DARK

Jagtvej 128, Tower G

2200 Copenhagen N., Denmark

Abstract

Type Ia supernovae (SNe) have played a significant role in measuring the acceleration of the Universe's expansion and the existence of dark energy. However, understanding the nature of SNe and the impact of population, originating from two distinct progenitor channels (single- and double-degenerate), changes over cosmic time is crucial to accurately measuring these phenomena. In this talk, we present a novel Bayesian hierarchical two-population model of Type Ia SNe which enables us to measure the properties of the two populations, redshift evolution of their relative fractions and thus investigate the impact of these elements on the precision and accuracy of constraints on the cosmological parameters.

Our model builds on earlier work by accounting for the varying fraction of two distinct Type Ia supernova populations over cosmic time. By modeling the redshift dependence of the two populations, we can estimate their respective fractions at different epochs and explore the impact of these changes on measurements of cosmological parameters.

We apply our model to simulations and observational data from Pantheon+. We show that observational data has signatures of redshift dependent fractions of the supernova populations and discuss these results in the framework of basic expectations related to the star formation history. We find that this demographic drift has potential implications for measuring cosmological parameters, as it affects the derived distance and intrinsic properties of Type Ia SN.

We discuss the implications of our results for future observations and the study of cosmology. Our model provides a framework for incorporating demographic drift into the two population model of Type Ia SNe, which could lead to more accurate measurements of the properties of dark energy. We also highlight the importance of continued observational efforts to constrain the properties of Type Ia SNe and their progenitor scenarios. In conclusion, our Bayesian two-population model of Type Ia SNe provides a powerful tool for exploring the demographic drift of these popula-

tions and its implications for measuring cosmological parameters. By accounting for the changing fraction of the two populations over cosmic time, we can improve our understanding of the nature of Type Ia SNe and their use as cosmological probes.

Contents

List of Figures

List of Tables

Introduction

"*Space is big. You just won't believe how vastly, hugely, mind-bogglingly big it is. I mean, you may think it's a long way down the road to the chemist's, but that's just peanuts to space.*"

- Douglas Adams, The Hitchiker's Guide To The Galaxy

Astronomy and astrophysics are unique amongst the sciences due to the nature of what is being worked with. While other fields are able to probe nature within their laboratories or in the field, astronomers are limited to what they can deduce from observations of the sky. This poses unique challenges, one of them being the measurement of distances and scales. As an example, how does one measure the distance to a far-away galaxy without being able to put down a yardstick? This simple question is still up for debate to this day, and will be central to this thesis.

In this thesis we focus on the usage of Type Ia supernovae (SNe) as a tool for measuring distances on a cosmological scale. This is possible due to these SNe acting as standard candles (Tripp, n.d.). These SNe are the result of white dwarf stars igniting in runaway thermonuclear explosions (Hillebrandt *et al.*, 2013), resulting in explosions with a remarkable degree of uniformity amongst their luminosities. This property is what we refer to when we describe Type Ia SNe as standard candles, and allows us to measure relative distances between SNe. One can even measure absolute distances given a set of calibration SNe with independently measured distances (Riess *et al.*, 2022). Due to the large luminosity of these events, often exceeding the output of their host galaxies, Type Ia SNe can be used to measure distances at large scales. Scatter is still present in Type Ia SNe peak luminosities, despite attempts at standardization, implying that Type Ia SNe are imperfect candles or that some underlying physics is not being modelled (Wojtak *et al.*, 2023).

The fact that Type Ia SNe can be used to measure distances across large scales means that we can use them as a probe of cosmological models. These models aim to describe the evolution of the Universe across large time and distance scales, with the current standard model of cosmology being ΛCDM. Type Ia SNe proved instrumental as cosmological probes to discover cosmic acceleration due to the presence of dark energy (Riess *et al.*, 1998; Perlmutter *et al.*, 1999), the Λ component of ΛCDM.

The standard model of cosmology is of course not complete, and Type Ia SNe are expected to help find cosmological tensions that hopefully will lead to new physics. One such current tension is the Hubble tension. This refers to a roughly 5σ difference between the value of the Hubble constant H0 measured using Type Ia SNe Riess *et al.*, 2022 and that measured by using the cosmic microwave background (CMB). Upcoming all-sky surveys conducted with next-generation telescopes such as the Vera C. Rubin Observatoryand the Nany Grace Roman Space Telescopeare expected to probe other cosmological parameters such as the dark energy equation of state parameter and matter density of the Universe to percent-level precision. This level of precision is expected to reveal further tensions within the current standard model of cosmology.

The fact that future surveys aim to achieve percent-level precision means that we have to ensure current modelling efforts are free of any systematics or biases at this level. In spite of how central Type Ia SNe are to making these measurements, remarkably little is known about the explosion mechanisms and progenitor systems of Type Ia SNe (Maoz *et al.*, 2014). The fact that Type Ia SNe are not very well understood and with models requiring an intrinsic scatter means that some underlying physics is being glossed over, posing a chance for astrophysical biases to be introduced into cosmological measurements.

1.1 Cosmology

"The evolution of the world can be compared to a display of fireworks that has just ended: some few red wisps, ashes and smoke. Standing on a well-chilled cinder, we see the slow fading of the suns, and we try to recall the vanished brilliance of the origin of worlds."

- Georges Lemaître, The Primeval Atom, 1950

Cosmology is the study of the origin, evolution and fundamental properties of the Universe as a whole. Although the field is large in scope, it deals with fundamental questions that have been asked by humanity throughout history; "Where did everything come from?", "Is the world infinite in extent?" and "What is the ultimate fate of the world around us?". Considering the scope of the questions that cosmology deals with, one would be hard pressed to cover the whole field in a Msc thesis. Instead this chapter aims to only scratch the surface, introducing the core assumptions definitions that form the basis of our current best answer to these fundamental questions, the ΛCDM model.

1.1.1 The FLRW Metric

A single principle underlies the current paradigm of thought in cosmology, known as the Cosmological Principle. This principle states that, if viewed on sufficiently large scales, the properties of the Universe are the same for all observers. One can think of this as an generalisation of the Copernican principle, that humans are not "privileged observers", extending it to cover the Universe as a whole. Assuming the Cosmological Principle brings with it two predictions for the Universe: homogeniety and isotropy. The first of these, homogeniety, is the claim that the Universe is observably uniform at large scales. The second, isotropy, is the claim that there is no preferred direction in the Universe. The seemingly simple assumption of the Cosmological Principle has large ramifications for how we describe the Universe around us. Using this assumption, a metric can be derived that describes a maximally symmetric Universe that can expand or contract as a function of time. This metric is known as the Friedmann-Lemaître-Robertson-Walker (FLRW) metric and is defined as

$$ds^2 = -c^2 dt^2 + a(t)^2 \left[dr^2 + S_\kappa(r)^2 d\Omega^2 \right], \qquad (1.1)$$

where we elegantly skip an introduction to GR and the metric's derivation. Here ds is the spacetime separation between two events, t is known as the proper time, r is a spherical spatial coordinate with $d\Omega(\theta, \phi)$ encompassing the remaining two coordinates, and

$$S_\kappa(r) = \begin{cases} R_0 \sin(r/R_0) & \text{if } \kappa = +1 \\ r & \text{if } \kappa = 0 \\ R_0 \sinh(r/R_0) & \text{if } \kappa = -1 \end{cases} \qquad (1.2)$$

Eq. 1.2 describes the geometry of an isotropic and homogenous Universe. $\kappa \in \{+1, 0, -1\}$ denotes the curvature with the three values representing a positively curved, flat and negatively curved Universe, respectively, and the constant R_0 denotes the radius of curvature. Finally, the function $a(t)$ is known as the scale factor. As the name implies, the scale factor describes the scaling of the Universe as a function of time, and is defined to be $a(t_0) = 1$, where t_0 is the current age of the Universe. From this one can define the distance between two points equivalent to the distance between them which would be measured with rulers at the time they are being observed, as

$$D_p(t) = a(t) \int_0^r dr = a(t)r, \qquad (1.3)$$

known as the proper distance. From this, the rate of change in proper distance can be written as,

$$\dot{D}_p = \dot{a}r = \frac{\dot{a}}{a}D_p = H(t)D_p, \tag{1.4}$$

where $H(t)$ is known as the Hubble parameter. Eq. 1.4 describes the recession velocity between two points due to evolution of the Universe via the scale factor. Expansion / contraction of the Universe via the scale factor would incur red / blueshift of light travelling between two points. This cosmological redshift is given by

$$a(t) = \frac{1}{1 + z(t)}. \tag{1.5}$$

From this we conclude that if we observe a galaxy with cosmological redshift $z = 2$, then we would in fact be observing it as it was at the time t_e when light was emitted and the Universe had a scale factor $a(t_e) = 1/3$.

1.1.2 A Dynamical Universe

Evaluating Eq. 1.4 at $t = t_0$, one gets $v = H_0 D$, where H_0 is known as the Hubble constant. This linear relation between distance and recession velocity was first observationally confirmed by Edwin Hubble in 1929, and the equation has come to be known as Hubble's law. This was a turning point of a discovery, as the fact that $H_0 > 0$ implies that the Universe is expanding over time. This in turn means that the Universe is dynamical, evolving as a function of time. The dependence ofthe scale factor on time, $a(t)$, is needed to describe a dynamical Universe. To calculate it, three equations are needed: the Friedman equation, the fluid equation and the equation of state. The first of these is defined as

$$1 - \Omega(t) = -\frac{\kappa c^2}{R_0^2 a(t) H(t)^2} \tag{1.6}$$

where $\Omega(t) = \frac{\epsilon(t)}{\epsilon_c}$ is the ratio between the energy density ϵ and the critical energy density ϵ_c corresponding to a flat Universe. In the Newtonian regime, this equation can be interpreted as describing energy conservation, with the potential and kinetic energy of expansion being constant. This equation allows us to link the different components of the FLRW metric, but does not by itself allow us to solve for the scale factor's dependence on time. We must introduce the second of the three equations, the fluid equation. By assuming that the content of the Universe at large scales

has the properties of a fluid, one can write the first law of thermodynamics in an expanding / contracting Universe as

$$\dot{\epsilon} + 3H(t)(\epsilon + P) = 0, \tag{1.7}$$

where P is the pressure associated with the material that fills the Universe. We can combine Eq. 1.6 and Eq. 1.7 to define the acceleration equation,

$$\frac{\ddot{a}}{a} = \frac{4\pi G}{3c^2}(\epsilon + 3P). \tag{1.8}$$

This equation shows that a positive energy density decelerates the Universe. If the material in the Universe contributes a negative pressure $P < -\frac{1}{3}\epsilon$, the Universe instead expands at an accelerating pace. Such a component is commonly referred to as dark energy.

The last equation needed to be able to describe a dynamic Universe is the equation of state, which relates the pressure and energy density $P = P(\epsilon)$. Assuming dilute gases, this can be written simply as $P = w\epsilon$, where w is a dimensionless scaling constant. It can be shown that $w = 0$ corresponds to the non-relativistic matter component of the Universe, while $w = 1/3$ corresponds to the relativistic component, such as photons / radiation. An especially interesting case is if a component exists that has $w < -1/3$. Such a component would provide a positive acceleration to the Universe, leading to expansion. The special case of $w = -1$ leads to a constant density of this component. Given these equations, one can (albeit not analytically) describe the dynamics of a Universe with, given values for the different constants described.

Assuming the Universe contains non-relativistic matter, radiation, curvature and a negative pressure component with energy density ϵ_Λ and equation-of-state $w_0 < 0.$, the Friedmann equation can be rewritten as

$$H(a) = H_0\sqrt{\frac{\Omega_{r,0}}{a^4} + \frac{\Omega_{m,0}}{a^3} + \frac{\Omega_{\Lambda,0}}{a^{3(1+w_0)}} + \frac{1 - \Omega_0}{a^2}} = H_0 E(a), \tag{1.9}$$

where $\Omega_{m,0} = \epsilon_{m,0}/\epsilon_c(0)$, $\Omega_{r,0} = \epsilon_{r,0}/\epsilon_c(0)$, $\Omega_{\Lambda,0} = \epsilon_{\Lambda,0}/\epsilon_c(0)$ and $\Omega_0 = \Omega_{m,0} + \Omega_{r,0} + \Omega_{\Lambda,0}$ are the energy density parameters for matter, radiation, dark energy and curvature respectively. We have reduced Eq. 1.6 to a differential equation in the scale factor (with the time dependence being implicit in Eq. 1.6), which can be solved numerically given values for the constants in Eq. 1.9.

Using Eq. 1.9, predictions can be made regarding the expansion, structure and evolution of the observable Universe, which in turn can be used to place constraints on the parameters of our model: H_0, $\Omega_{m,0}$, $\Omega_{r,0}$, $\Omega_{\Lambda,0}$ and w_0. Current constraints have $\Omega_{m,0} \approx 0.3$, $\Omega_{r,0} \approx 0$, $\Omega_{\Lambda,0} \approx 0.7$ and $w_0 = -1$. This is the current standard model

of cosmology, known as ΛCDM. This model contains a cosmological constant corresponding to dark energy, Λ, that leads to the observed expansion of the Universe, as well as a large component of non-relativistic matter that only interacts via gravity, known as cold dark matter (CDM). This model fits remarkably well with observations, but is incomplete. The earlier mentioned Hubble tension is a 5σ difference in measurements of the Hubble constant from probes in the early and late Universe. Similar tensions exist in other parameters relating to structure formation (Di Valentino *et al.*, 2021).

1.1.3 Distance Measures

In Eq. 1.3 we introduced the proper distance. To measure this distance would require an adequately long ruler and a method of measuring said distance in an instant. Experimentalists have not figured out how to hit the pause button on the Universe, and as such we need to introduce different, observable distance measures when working on cosmological scales.

We first introduce the line-of-sight comoving distance D_C. From Eq. 1.5 we have that both that $dz = da$. Eq. 1.3 that $dz/E(z)$ is proportional to the travel time of a photon over the redshift-interval dz divided by a. This is equivalent to the proper distance divided by the the scale factor, and by integrating we get

$$D_C = \frac{c}{H_0} \int_0^z E^{-1}(z') dz' = D_H \int_0^z E^{-1}(z') dz', \tag{1.10}$$

where D_H is the Hubble distance. This distance corresponds to the constant (over time) distance between two objects moving with the Hubble flow. We have defined in terms of redshift instead of scale factor, as we can observe cosmological redshift by observing distance objects that are less impacted by peculiar motion relative to us. If instead we have two objects at the same redshift but separated by some angle $d\theta$, we define the separation to be the transverse comoving distance,

$$D_M = \begin{cases} \frac{D_H}{\sqrt{1-\Omega_0}} \sinh\left(\frac{\sqrt{1-\Omega_0} D_C}{D_H}\right) & \text{for } 1 - \Omega_0 > 0 \\ D_C & \text{for } 1 - \Omega_0 = 0 \\ \frac{D_H}{\sqrt{|1-\Omega_0|}} \sinh\left(\frac{\sqrt{|1-\Omega_0|} D_C}{D_H}\right) & \text{for } 1 - \Omega_0 < 0 \end{cases} \tag{1.11}$$

This distance is defined using $S_\kappa(r)$ from the FLRW metric and Eq. 1.9, which gives a curvature radius of $R_0 = \frac{D_H}{\sqrt{|1-\Omega_0|}}$.

With these definitions in place, we can now relate cosmological distance measures to observable distances. This work focuses on SNe Ia which are point-like sources. For

such objects, the luminosity distance is a typical distance measure. It is defined as the relationship between bolometric flux F and luminosity L,

$$D_L = \sqrt{\frac{L}{4\pi F}}.$$ (1.12)

Alternatively, it can be defined in terms of apparent and absolute magnitudes m and M as

$$m - M = 5\log\left(\frac{d_L}{10}\right).$$ (1.13)

In an expanding Universe the energy per photon will decrease due to cosmological redshift, reducing the observed flux F by a factor of $(1+z)$. Additionally, the time between emission of two photons will be increased by a factor of $(1+z)$. This decreases the rate of photons and thereby the flux is decreased by a total factor of $(1+z)^2$. In a flat, static Universe $D_L = D_M$, but in the general case where the flux is decreased by a factor $(1+z)^2$ this would become

$$D_L = (1+z)D_M.$$ (1.14)

Using Eq. 1.14 we can relate observable distances to the underlying cosmological model, assuming that the observed redshift is purely due to expansion of the Universe. We will in the next section explore how SNe Ia can be used to constrain the underlying cosmology using this relation.

1.2 Type Ia Supernovae as Cosmological Probes

"Because I have contemplated explaining what I think, not only about the location and movement of this light, but also about its substance and origin, and believing that I have found an explanation that, for lack of evident contradictions, may well be true, I have finally arrived at the belief of being capable of knowing something about this wonder, beyond the point where pure conjecture ends."

- Galileo Galilei, letter to O. Castelli regarding the Stella Nova of 1604

The observations of the supernovae (SNe) of 1572 and 1604, and the attempts, by Tycho, Kepler, Galileo, and others, to understand their natures and locations, were transformational events in the history of science. These attempts can be viewed as signaling the beginnings of modern astrophysics. Among the handful of historical

SN events in the Galaxy recorded over the past two millennia, we now know that at least some were core-collapse (CC) SNe, involving the explosion of massive (M > 8M$_\odot$) stars, while others were the thermonuclear explosions of lower-mass stars, now known as Type-Ia supernovae (SNe Ia). These stellar infernos have captured our attention since the time of Galileo, continuing to illuminate the Universe around us. With advancements in technology and our understanding of physics, the study of supernovae has evolved into a multidisciplinary endeavor, intertwining astronomy, astrophysics, nuclear physics, and even cosmology. SNe Ia have proven themselves especially useful in the field of cosmology due to their remarkable uniform luminosity, earning the title of "standard candles". These standard candles will be the focus of this chapter.

SNe Ia are distinguished from CC SNe based on their spectroscopic features: the absence of hydrogen absorption lines and the presence of strong silicon lines in the epochs up to and including peak luminosity. These spectral features, combined with the measured energetics, are what first lead astrophysicists to propose the idea that SNe Ia are degenerate stellar cores undergoing thermonuclear combustion (Hoyle, n.d.). The combination of observed spectral features and the presence of SNe Ia in older stellar populations further indicate that this degenerate core is a carbon-oxygen white dwarf (Nugent *et al.*, 2011; Bloom *et al.*, 2012). Singular white dwarfs are stable objects, raising the question of what leads white dwarfs to ignite. This has been attributed to the accretion of mass onto the white dwarf from a binary companion, until the white dwarf reaches roughly the Chandrasekhar mass $M_{Ch} = 1.44$ M$_\odot$. At this mass the the white dwarf reaches a temperature and pressure such that carbon ignites, leading to the runaway thermonuclear explosion (Maoz *et al.*, 2014).

The fact that SNe Ia are most likely always caused by the thermonuclear detonation of a C/O white dwarf with $M \sim M_{Ch}$ is a natural explanation for the observed homogeniety and status as standard candles. This property has led to SNe Ia have playing an instrumental role in the discovery of the accelerating expansion of the Universe (Riess *et al.*, 1998; Perlmutter *et al.*, 1999), and they continue to be one of the most prominent probes for constraining cosmological models described in the previous Section. SNe Ia are interesting objects of astrophysical study in-and-of themselves, being major contributors to the evolution of galaxies, contributing to the chemical enrichment of the Universe and influencing subsequent generations of stars (Hillebrandt *et al.*, 2013).

Due to their important role both in astrophysics and cosmology, multiple generations of surveys have been dedicated to the study of SNe Ia. As a result, the number of observed SNe Ia, as well as our understanding of the physics that drive them, has increased dramatically since the time of Tycho, Kepler and Galileo. Although

we have deepened our understanding of SNe Ia, many questions about these stellar explosions remain. In this section we will provide a short review of SNe Ia, their usage in cosmology, as well as an overview of some of the main problems in the field.

1.2.1 Standard Candles

The Tripp Calibration

When a SNe Ia is observed, a light-curve is recovered together with a spectra if observational resources are available. The light-curve shows the evolution in brightness for a given band over time. These light-curves are modelled in different ways to extract information from them, with one of the most common being the SALT model. This model compresses the light-curve down to three observables: the peak apparent B-band magnitude m_B, the stretch x_1 which is related to the decline rate, and an apparent $B - V$ color c_{app}. Examples of B-band light-curves are shown in the left of Fig. 1.1, where we compare the B-band light curves of multiple SNe Ia. As
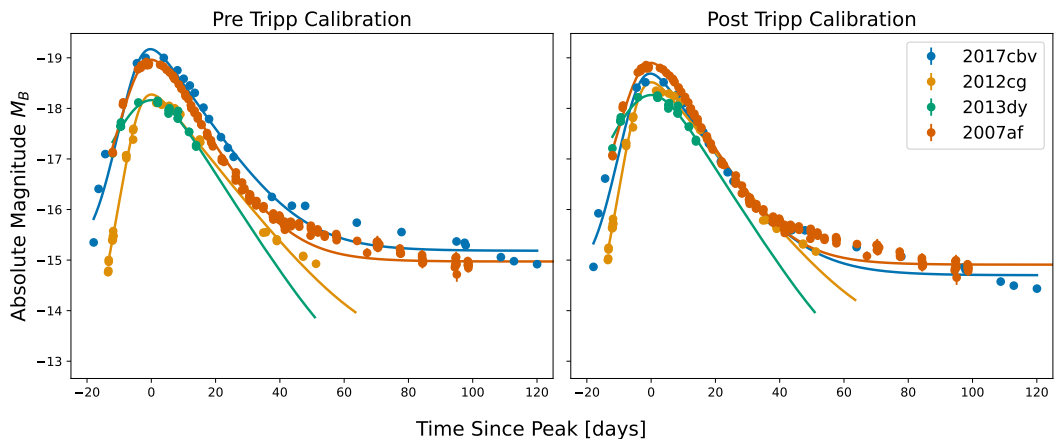
FIGURE 1.1.
Comparison of B-band absolute magnitude light-curves for 4 SNe Ia. Light-curve fits are Bazin models shown for illustrative purposes. *Left*: Light-curves before the Tripp calibration is applied. *Right*: SNe Ia after the Tripp calibration is applied. Values used are the standard fiducial values $\alpha = 0.148$ and $\beta = 3.122$.

mentioned earlier, SNe Ia are known as standard candles due to the observed homogeniety in luminosity across SNe. This homogeneity is due to the majority of SNe Ia being the result of thermonuclear detonation of C/O white dwarfs with roughly $M \sim M_{Ch}$. The peak absolute B-band magnitudes of SNe Ia have an intrinsic dispersion of $\sigma_{int} = \sigma(M_B^{int}) \sim 0.3$ (Hamuy *et al.*, 1996), where M_B^{int} is the corrected, intrinsic absolute magnitude. This scatter is visible in when comparing the peak absolute magnitudes of the light-curves shown in Fig. 1.1. Reducing the dispersion in

SNe Ia peak magnitudes is paramount to their usage as standard candles. Empirical correlations between the peak absolute magnitude and SN properties can be used to calibrate the observed light curves, such that dispersion is decreased. The first of these empirical relations is between the peak absolute magnitude and the width / rate of decline of the SNe Ia light curve, known as the Phillips relation (Phillips, 1993): brighter SNe have light curves that are wider / slower evolving. A second correlation that has become standard in the SNe Ia literature is the color correction, based on the observation that SNe Ia with redder observed colors are fainter (Tripp, n.d.). These empirical correlations can be combined into what is known as the Tripp calibration (Tripp, n.d.),

$$M_B = M_B^{int} + \alpha X_1 + \beta c_{app}. \tag{1.15}$$

Here M_B is the observed peak absolute B-band magnitude. X_1 denotes the width, also known as stretch, with α parameterizing the Phillips relation. In the last term c_{app} is the $B - V$ color at peak luminosity and β parameterizes the color correction. This calibration can be rewritten into it's more commonly used form

$$m_B = M_B^{int} + \alpha X_1 + \beta c_{app} + \mu(z), \tag{1.16}$$

where m_B is the observed apparent B-band magnitude and $\mu(z)$ is the distance modulus. Eq. 1.16 shows how SNe Ia can be used to constrain cosmological parameters, since the distance modulus depends on the underlying cosmology,

$$\mu(z) = m_B - M_B = 5 \log_{10} \left(\frac{D_L(z)}{10 \text{ pc}} \right), \tag{1.17}$$

where D_L is the luminosity distance defined in Eq. 1.14. From this we see that relative distances of SNe Ia should be able to provide constraints on the component densities in cosmological model, e.g. $\Omega_{m,0}$, $\Omega_{\Lambda,0}$ and the likes from Section 1.1. One would have to define an absolute distance scale to constrain the Hubble constant, which enters Eq. 1.14 as an additive constant. This is done using the cosmic distance ladder, where different steps or rungs of known distance indicators are used to calibrate indicates further away (Riess *et al.*, 2022). A typically used approach is using parallax measurements (first rung) to calibrate the period-luminosity relation for Cepheids (second rung), wich in turn is used to calibrate extragalactic SNe Ia (the third rung). Applying the Tripp calibration to SNe has led to reduction of the intrinsic dispersion from $\sigma_{int} \sim 0.3$ to $\sigma_{int} \lesssim 0.15$. The right side of Fig. 1.1 shows the intrinsic peak B-band magnitudes $M_{B,i}^{int}$ for the example SNe Ia, where fiducial values $\alpha = 0.148$ and $\beta = 3.122$ have been chosen (Riess *et al.*, 2022; Brout *et al.*, 2022a)

Dust and Intrinsic Dispersion

As the light of SNe Ia leaves its host galaxy, it passes through a random column of dust in the interstellar medium. This dust absorbs and scatters light in a wavelength-dependent process, leading to extinction (dimming) and reddening (shifting colors to positive values). The change in rest-frame $B - V$ color is known as dust reddenning and is denoted $E(B-V)$. The resulting extinction in the B-band, A_B, is proportional to the dust reddening $A_B = R_B E(B - V)$, where R_B is known as the extinction coefficient. Since dust only dims, $E(B - V) \geq 0$. Likewise, R_B can be related to dust grain size and has the constraint $R_B \geq 0$, with some theoretical studies placing higher lower bounds such as $R_B > 2$ (Draine, 2003).

The color-luminosity relation in Eq. 1.16 relates the observed apparent color to the SNe Ia luminosity. If the intrinsic SNe Ia color is $c_{int} = 0$ then this relation can be understood as being entirely due to the effects of dust. In this case, one would expect $\beta = R_B$ and $c_{app} = E(B - V)$. This does not hold, however, if there are non-zero intrinsic SNe Ia colors or a variation in them. SNe Ia analyses using the Tripp calibration presented in Eq. 1.16 find R_B varying between $2 - 4$ depending on the sample and specific methodology used (Mandel *et al.*, 2017). These values are inconsistent with values measured in the Milky Way (MW), varying between $2.1 - 5.8$ with a typical value of $R_B \approx 4.3$ (Schlafly *et al.*, 2016).

From the previous section we also know that intrinsic dispersion still exists, with $\sigma_{int} \lesssim 0.15$. This is also visible in the right side of Fig. 1.1. Assuming SNe Ia are truly standardizable, this dispersion can be thought of as a fudge factor to account for missing physics in the chosen model. All of this suggests that accounting for extinction and dust reddening can lead to a more physical SNe Ia calibration. In this case, the observed apparent color would be a convolution of the distributions describing intrinsic SNe Ia colors and extrinsic extinction due to dust. To account for this, (Mandel *et al.*, 2017) introduced hierarchical models (see Section **??**) that extend Eq. 1.16,

$$m_B = M_B^{int} + \alpha X_1 + \beta c_{int} + R_B E(B - V) + \mu(z), \tag{1.18}$$

$$c_{app} = c_{int} + E(B - V), \tag{1.19}$$

where c_{int} is the intrinsic SNe Ia color. Using this approach (Mandel *et al.*, 2017) find $R_B = 3.8 \pm 0.3$, consistent with the normal MW value. Similar work by (Brout *et al.*, 2021) find a reduced intrinsic dispersion of $\sigma_{int} \approx 0.08$. As we can see, SNe Ia become better standard candles when applying physically motivated models instead of purely empirical relations.

Impact of Host Galaxy Properties

In the previous section we introduced the Tripp calibration and its extension to include dust properties. This extension led to a reduction in intrinsic scatter by making the calibration more physical, but did not succeed in fully removing the dispersion. Although more physical, the calibration is still largely driven by empirical relations between observables. Additional correlations between SNe Ia luminosities and properties of their host galaxies have been observed (Kelly, 2007), and have become a common extension of Eq. 1.16 in the SNe Ia literature. The observed correlation for host stellar mass can be seen in Fig. 1.2, where we plot SNe Ia absolute magnitudes M_B from Pantheon+ (see Section 3.3) versus the global stellar mass of their host galaxies, including a mass cut $S_{M_*} = 10.$. This correlation is often referred to as
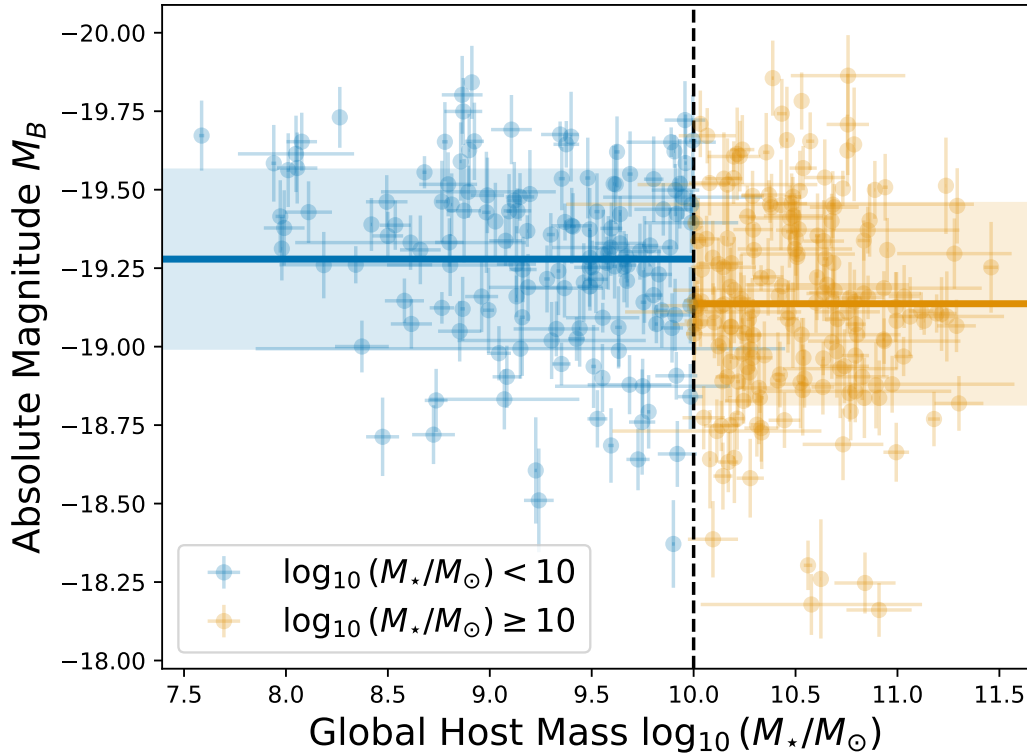
FIGURE 1.2.
SNe Ia absolute B-band magnitudes after applying Eq. 1.16 versus host galaxy mass. A cut is made at $S_{M_*} = 10.$, with low mass SNe Ia shown in blue and high mass SNe Ia shown in orange. Average magnitudes $\hat{M}_B^{low} = -19.28 \pm 0.02$ mag and $\hat{M}_B^{high} = -19.14 \pm 0.02$ mag are shown by the solid lines. The shaded regions show the 3σ scatter around the mean. The value of the observed mass step is $\Delta M_* = 0.14 \pm 0.03$ mag.

the mass step, due to the approximately step-like change in luminosity between low- and high-mass galaxies. This step parameterizes the observed relation that SNe Ia in

more massive galaxies appear dimmer after standardization, compared to SNe Ia in lower mass galaxies. This step is typically parameterized as (Scolnic *et al.*, 2022)

$$\delta_{M_*} = \Delta M_* \left[\frac{1}{2} - \left(1 + \exp\left((M_* - S_{M_*})/\tau_{M_*}\right)\right)^{-1} \right], \qquad (1.20)$$

where ΔM_* is the magnitude of the SN Ia luminosity difference between SNe above and below the step value S_{M_*} for the host mass M_*. This is equivalent to a smooth sigmoid transition from a value of $-\Delta M_*/2$ for $M_* \ll S_{M_*}$ and $\Delta M_*/2$ for $M_* \gg S_{M_*}$. Applying this to Tripp calibration, we get an extended calibration given by

$$m_B = M_B^{int} + \alpha x_1 + \beta c_{app} + \mu(z) + \delta_{M_*}. \qquad (1.21)$$

(Mandel *et al.*, 2017) explore the dependence between the host mass step and dust properties as a potential explanation for the observed correlation between host mass and SNe Ia luminosity. They allow for differing distributions of dust reddening $E(B-V)$ between low- and high-mass host galaxies, and find that roughly a third of the observed mass step can be explained by differences in dust distribution between the two populations of galaxies. Similarly (Brout *et al.*, 2021) allow for differing $E(B-V)$ and R_B between low- and high-mass host galaxies, finding mean values $R_B = 3.94$ and $R_B = 2.85$ for low- and high mass galaxies respectively. In their study they find that the majority of the observed mass step is explained by differences in dust properties and distribution between low- and high mass galaxies. As noted by (Brout *et al.*, 2021), similar results have been found by (Wang *et al.*, 2009) when splitting SNe Ia on velocities derived from spectra, which imply differences driven by intrinsic SNe Ia properties.

Similar empirical correlations and step functions have been applied to other host properties, both to the local SNe Ia environment and the global host environment. Examples of properties studied include local/global specific star-formation rate (LsSFR / sSFR), rest-frame U-V color and morphological type (Rigault *et al.*, 2020; Jones *et al.*, 2015; Pruzhinskaya *et al.*, 2020). Results vary across the cited studies due to (amongs other things) differences in the samples used, and the physical explanation for the observed correlations is still a topic of debate. A potential explanation to these observed correlations will be explored in the following section.

1.2.2 The Progenitor Problem

In the previous section we introduced how SNe Ia can be used as standard candles due to the observed homogeniety in peak luminosity. We introduced the Tripp calibration used to reduce intrinsic dispersion in observed luminosities, as well as physical and empirical extensions to reduce this intrinsic dispersion. As mentioned previously,

this intrinsic dispersion can be understood as a fudge factor that accounts for unmodelled astrophysics. It may come as a surprise to the reader, but one such unmodelled aspect is the progenitor of SNe Ia. We have previously described how SNe Ia are the result of runaway thermonuclear detonation of a C/O WD, with the detonation most likely being caused due to accretion of mass up to the Chandrasekhar limit of $M_{Ch} = 1.44$ M$_\odot$. The specifics of how the SNe Ia accretes this mass, what kind of binary partner (or donor) provides this mass and how the detonation starts, is currently an open question (Liu *et al.*, 2023; Maoz *et al.*, 2014; Hillebrandt *et al.*, 2013) This is known as the Progenitor Problem. Multiple different progenitor scenarios and explosion mechanisms have been proposed by theoreticians and computational astrophysicists. These scenarios can generally be divided into two main categories: the single-degenerate (SD) and double-degenerate scenarios, which we will explore in this section.

The Single-Degenerate Scenario

In the single-degenerate scenario, a WD accretes material from a non-degenerate donor / companion star via a Roche-lobe overflow or stellar wind(Liu *et al.*, 2023). By accreting material from the donor star, the WD's mass continues to grow until it reaches the Chandrasekhar mass M_{Ch}, at which point thermonuclear detonation begins. This scenario is illustrated in the top of Fig. 1.3. Although this scenario would explain the observed homogeniety of SNe Ia, due to detonation occurring at a homogenous stage of accretion, observations pose some challenges. For the WD to retain the accreted material and grow in mass, a narrow range of accretion rates on the order of $10^{-8} - 10^{-7}$ M$_\odot$ yr-1 are required. This in turn reduces the predicted SNe Ia rate, which is in conflict with the observed no. of SNe Ia (Liu *et al.*, 2023). Numerical simulations of SNe Ia reproduce the expected behaviour of homogeniety, although one may say that it does so *too* well. Although simulations reproduce homogeniety, they struggle to reproduce the observed scatter in SNe Ia decline rate / stretch and luminosity (Liu *et al.*, 2023; Hillebrandt *et al.*, 2013). Finally, most subclasses of the SD scenario predict that the donor star survives the explosion. No such surviving companion stars have been found at the time of writing.

The Double-Degenerate Scenario

In the double-degenerate scenario, two C/O WDs in a binary system are brought into contact by the emission of gravitational waves (Maoz *et al.*, 2014), illustrated in the bottom of Fig. 1.3. At the point of contact, the binary pair merges via tidal interaction, triggering the thermonuclear explosion if their combined mass exceeds M_{Ch}. Multiple evolutionary paths can lead to this scenario (see Fig. 2 in (Liu *et al.*,
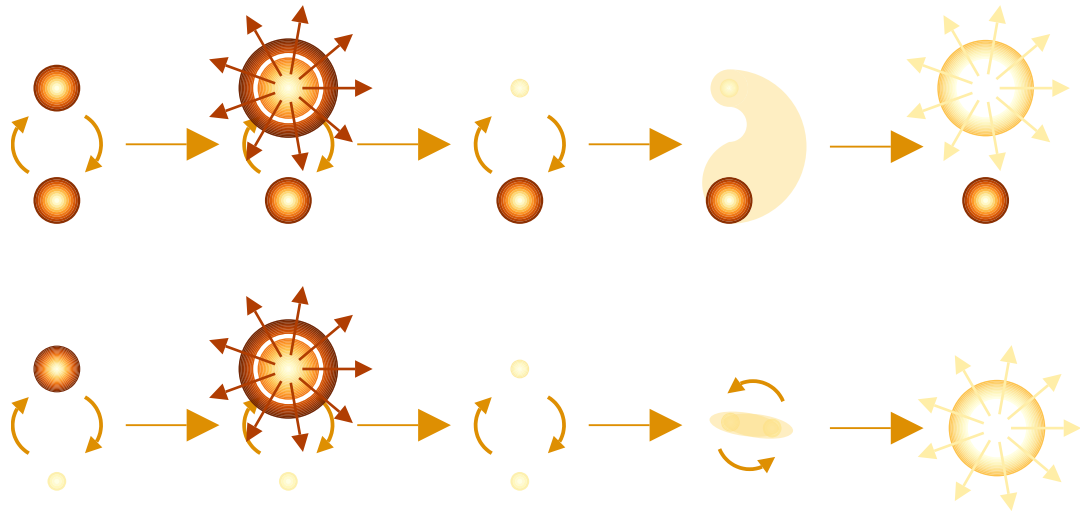
FIGURE 1.3.

Upper: Evolutionary path for the single-degenerate progenitor scenarios. 1) A binary pair of stars. 2) The main binary star reaches the asymptotic giant branch, growing in size and shedding outer layers. 3) The main binary continues along it's evolutionary path, cooling into a white dwarf. 4) The white dwarf begins accreting mass from the donor star. 4) The white dwarf reaches the Chandrasekhar mass M_{Ch} and undergoes runaway thermonuclear fusion, leading to a SNe Ia. *Lower*: Evolutionary path for a double-degenerate path. 1) A binary pair of a white dwarf and a star. 2) The stellar companion reaches the asymptotic giant branch, growing in size and shedding outer layers. 3) The stellar companion continues along it's evolutionary path, cooling into a white dwarf. 4) The white dwarfs spiral closer due to gravitational wave emission, potentially allowing for accretion. 5) The two white dwarfs either merge or begin burning He, leading runaway thermonuclear fusion, leading to a SNe Ia. The donor white dwarf may or may not survive this event.

2023)), but the key question is if it can lead to a SNe Ia explosion. Different studies have indicated that the merger could lead to off-center carbon-burning, with the predicted result that the merger would lead to a neutron star instead of a SNe Ia. As with the SD scenario, sub-classes of the DD scenario exist that circumvent this issue. One of these is the "double detonation" model, where the binary consists of a C/O WD and a He donor WD (Maoz *et al.*, 2014). In this scenario an initial He detonation can be triggered by accumulating a He shell on top of the C/O WD, which in turn can trigger the burning of carbon and the runaway thermonuclear explosion. This scenario has the added benefit that sub-Chandrasekhar mass WDs can lead to SNe Ia, alleviating some of the tension between theoretical and observed SN Ia rates. The DD scenario would also explain the lack of detected companion stars in SNe Ia that the SD scenario predicts. Finally, recent detection of high-velocity WDs by (El-Badry *et al.*, 2023) are a smoking gun of this double detonation model, with the high velocity and chemical composition indicative of the double detonation model.

The DD scenario is however not without issues. Simulations predict a relatively wide range of explosion masses, making reproduction of the observed SNe Ia homogeniety hard to reproduce. Additionally, observations with Gaia [CITE GAIA STUDIES] have attempted to identify WD binaries that are expected to merge within a Hubble time.

150 DD systems have been detected so far, but only about 10 of these systems are predicted to merge within a Hubble time, in direct conflict with observed SNe Ia rates.

Relation to Observations

Of the two proposed proposed progenitor scenarios, neither agree fully with observations. In fact, the current line-of-thought is that a combination of different progenitor scenarios is needed to fully explain current SNe Ia observations, known as the $A+B$ model (Maoz *et al.*, 2014). This model originates from early observations of a correlation between the observed SNe Ia rates and the host-galaxy color, morphology and sSFR (Mannucci *et al.*, 2005; Li *et al.*, 2011; Smith *et al.*, 2012). This model proposes the existence of two populations of SNe Ia progenitor systems, with the rate of occurence for population A SNe being proportional to the host stellar mass and the rate for population B SNe being proportional to the host SFR. These have also been described as delayed and prompt populations, referring to the amount of time that passes between a burst of star-formation and a SNe Ia for each of these progenitor populations.

The possibility that multiple progenitor channels contribute to observed SNe Ia poses a simple explanation to the observed intrinsic dispersion and to empirical correlations between SNe Ia luminosity and host properties. As (Brout *et al.*, 2021) show, the impact of extrinsic environmental properties can not be ignored, but inclusion of such extrinsic effects like dust do not fully remove intrinsic dispersion. Instead one could explain this dispersion as being due to the implicit assumption in Eq. 1.16 that all SNe Ia stem from a single progenitor channel. (Rigault *et al.*, 2020) explore this via correlations between SNe Ia luminosity and LsSFR, finding the strongest-to-date measured luminosity step $\delta_{LsSFR} = 0.163 \pm 0.029$ mag. LsSFR is used, as the authors argue that it is a a relatively pure tracer of SNe Ia progentior ages, making it a useful probe for identifying differences in SNe Ia due to underlying progenitor differences. Using the LsSFR cut $S_{LsSFR} = -10.8$, one can clearly observe a bimodality in the distribution of SNe Ia stretch, as shown in Fig. 1.4. This bimodality in SNe Ia stretch is well-known in the literature, but as of yet unexplained. The proposed impact of multiple progenitor channels can also be used to explain the luminosity steps observed with host properties other than LsSFR. (Briday *et al.*, 2022) simulate SNe Ia with extinction coefficients R_B that vary between young and old host galaxies as well as a difference in intrinsic luminosity between young and old progenitor systems and use different host property tracers to model the differences. They find that local specific star formation rate (lsSFR) is a relatively pure tracer of the galaxy age difference, but can not rule out any intrinsic difference in SNe Ia luminosity
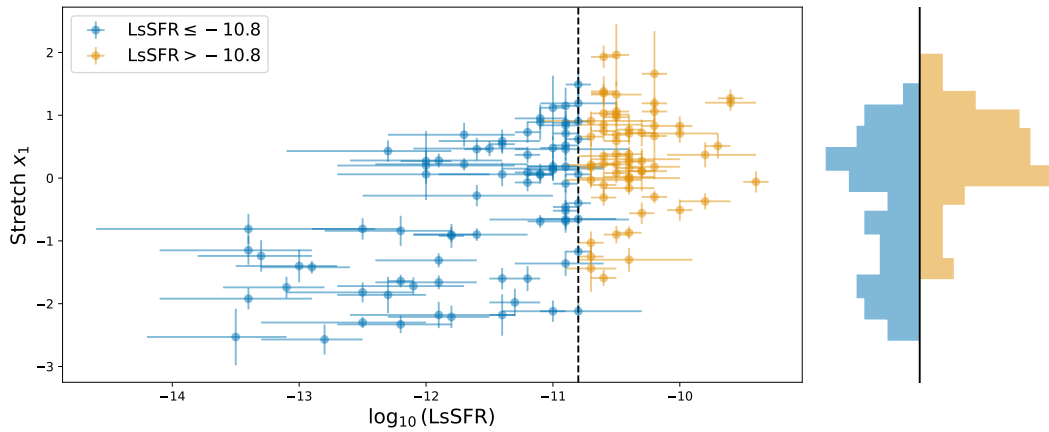
FIGURE 1.4.
Recreation of Fig. 4 in (Rigault *et al.*, 2020). *Left*: SNe Ia stretch versus local specific star-formation rate, with a cut $S_{\mathrm{LsSFR}} = -10.8$. *Right*: Normalized distribution of stretch parameters for SNe Ia below and above S_{LsSFR}, respectively.

the case of multiple properties driving the observed differences. The authors also explore other local and global properties as tracers of these differences, finding that the simulated differences lead to correlations and luminosity steps similar to those described in the previous section.

As we saw in the previous section, increasing the physicality of the Tripp calibration lead to better SNe Ia standardisation and reduced intrinsic dispersion. Work by theoreticians such as (Maoz *et al.*, 2014; Hillebrandt *et al.*, 2013) and observers (Rigault *et al.*, 2020; Wiseman *et al.*, 2023) indicate that improved constraints on SNe Ia progenitors will lead to improved constrains on SNe Ia standardization, and thus better cosmological constrains. In the next section we will explore how such constraints can be obtained.

1.2.3 SNe Ia Rates

In the previous section we introduced the progenitor problem, the fact that the nature and identity of SNe Ia progenitor systems are not yet well understood. We also introduced the single- and double-degenerate progenitor models, the two main progenitor channels for SNe Ia discussed in the literature. These progenitor channels have different characteristic timescales between formation of the binary pair and the resulting SN Ia detonations. This delay between a burst of star-formation and the eventual SNe is known as the delay-time, τ. The distribution over the SN rate versus delay-time that would follow a brief burst of star formation leading to a unit total mass of stars is known as the delay-time distribution, or DTD. One can think of this as the response function to star formation that embodies physical information about the system. The DTD is directly linked to the lifetimes of the stars leading up to

SNe Ia detonation and can thus be used to differentiate between different progenitor models. Theoretical DTDs have been derived using binary population synthesis models, forward modelling the formation and evolution of SD and DD binary populations leading up to detonation. Others approaches include physically motivated parametric models and ad-hoc functions to best fit the observed rate of SNe Ia.

Generic features can be derived for the DD and SD models from physical considerations. For example, a power law distribution is generic to progenitor models characterized by gravitational wave driven mergers. This can be found by first considering the dynamics of a system driven by gravitational waves as in the DD progenitor model, where the time τ until merger is given by

$$\tau \sim a^4, \tag{1.22}$$

where a is the initial separation. If the distribution of a follows a power law

$$\frac{dN}{da} \sim a^\epsilon \tag{1.23}$$

the the rate of SNe Ia is given by

$$\frac{dN}{d\tau} = \frac{dN}{da}\frac{da}{d\tau} \sim \tau^{(\epsilon-3)/4}. \tag{1.24}$$

For $\epsilon \approx -1$ the DTD for the DD progenitor model will have an exponent close to -1. This is in agreement with observed separations between non-interacting binaries and binary population synthesis models, although in reality the behaviour is likely to be more complex. If one instead assumes that the delay-time between the formation of a WD and a SN Ia detonation is always brief compared to the formation time of the WD, a simple proxy for the SD progenitor model, then the DTD will simply be proportional to the formation rate of WDs. Assuming that the main sequence lifetime depends on a stars mass

$$\tau \sim m^\delta, \tag{1.25}$$

and a power law initial mass function,

$$\frac{dN}{dM_*} \sim M_*^\lambda, \tag{1.26}$$

then the WD rate, and by extension the DTD, is given by

$$\frac{dN}{d\tau} = \frac{dN}{dm}\frac{dm}{d\tau} \sim \tau^{(1+\lambda-\delta)/\delta}. \tag{1.27}$$

Using $\delta = -2.5$ from stellar evolution models and the Salpeter slope $\lambda = -2.35$ (Maoz *et al.*, 2012), the DTD exponent is $\sim -1/2$. Eq. 1.24 and Eq. 1.27 can be

combined as a broken power law such that the $-1/2$ slope represents a bottleneck in the formation of progenitor systems up to some time t_c, after which the gravitational wave driven mergers take over as the main driver of mergers. One such choice could be $\tau = 500$ Myr corresponding to the lifetime of $3M_\odot$ stars, after which the supply of new SD progenitor systems goes to zero, letting the -1 slope dominate (Maoz *et al.*, 2012). Different approaches have been used to further describe the SD progenitor model, but the general trend is that of a sharp drop in SNe Ia rate after a few Gyrs. Measurements of the DTD derived from observations are shown in Fig. 8 in (Maoz *et al.*, 2012) together with a scaled τ^{-1} power law, showing good agreeance especially at higher delay times. At lower delay times the picture is less clear, and the presence of a $\tau^{-1/2}$ component is not clear.

A typical parameterization of the combined DTD for the SD and DD progenitor models is given by (Rodney *et al.*, 2014). This parameterization is a broken power law describing prompt and delayed SNe Ia, corresponding to the simple SD and DD progenitor models listed earlier, referring to the time it takes from formation of the binary to detonation. (Rodney *et al.*, 2014) assume a constant DTD for the prompt SNe Ia component due to lacking observational constraints for early delay times (Maoz *et al.*, 2014; Liu *et al.*, 2023). This DTD is given as

$$\Psi(\tau) = \begin{cases} 0 & \text{for } \tau < \tau_0, \\ K\eta\frac{f_p}{1-f_p} & \text{for } \tau_0 \leq \tau < \tau_1, \\ \eta\tau^{-1} & \text{for } \tau_1 \leq \tau \leq \tau_{max}, \end{cases} \tag{1.28}$$

where η denotes the efficiency of generating SN Ia after a burst of star formation, in units of $\frac{N_{Ia}}{\text{yr}M_\odot}$, and f_p sets the fraction of all SNe Ia that arise from the prompt channel. The constant K is defined by the chosen time-thresholds,

$$K = \frac{\log\left(\tau_{max}/\tau_1\right)}{\tau_1 - \tau_0}, \tag{1.29}$$

As in (Rodney *et al.*, 2014) we choose $\tau_0 = 40$ Myr equivalent to the shortest possible time to create a SNe Ia explosion [CITE Belczynski 2005], $\tau_1 = 500$ Myr marking the transition from a constant DTD to a τ^{-1} power law as earlier, and τ_{max} equal to the age of the Universe for the chosen cosmology.

Constraining the DTD observationally can give valuable insight into the progenitor systems of SNe Ia. One such way is by measuring volumetric SNe Ia rates by binning SNe Ia from untargeted / wide-field surveys by redshift and normalizing the number of SNe Ia to the rest-frame volume and duration of observation. An example of such observations from (Wojtak *et al.*, 2019) can be seen in Fig. 1.5.

The DTD can be converted to the volumetric SNe Ia rate via a convolution with a parameterized representation of the cosmic star-formation history (cSFH), $\chi(z)$,

$$R_{Ia}(t) = \int_0^t \chi\left(f^{-1}(t-\tau)\right)\Psi(\tau)d\tau, \tag{1.30}$$

where t is the input age of the Universe, $f(z)$ is the function mapping a given redshift to the corresponding age of the universe, and f^{-1} is the inverse mapping from age to redshift. This conversion is necessary as most cSFHs are expressed in terms of redshift. As mentioned earlier, the rate of SNe Ia can be understood as a response (in the form of the DTD) to a burst of star-formation (as a function of redshift / time via the cSFH). In this work we use the (Madau *et al.*, 2014) cSFH determined from ultraviolet (UV) and infrared (IR) observations,

$$\chi(z) = 0.015\frac{(1+z)^{2.7}}{1+[(1+z)/2.9]^{5.6}} \quad \mathrm{h}_{70}\,\mathrm{M}_\odot\,\mathrm{yr}^{-1}\,\mathrm{Mpc}^{-3}. \tag{1.31}$$

The volumetric SNe Ia rate can be decomposed into the volumetric rate of SNe Ia originating from the prompt or delayed channel as

$$R_{Ia}^P(t) = K\eta\frac{f_p}{1-f_p}\int_{\tau_0}^{\tau_1}\chi\left(f^{-1}(t-\tau)\right)d\tau, \tag{1.32}$$

$$R_{Ia}^D(t) = \eta\int_{\tau_1}^t\frac{\chi\left(f^{-1}(t-\tau)\right)}{\tau}d\tau. \tag{1.33}$$

Fig. 1.5 shows the total, prompt and delayed progenitor channel volumetric SNe Ia rates, where we use $\eta = 1.02^{+0.27}_{-0.15}\times10^{-4}h_{70}^2\,\mathrm{yr}^{-1}\,\mathrm{M}_\odot^{-1}$ and $f_p = 0.63^{+0.07}_{-0.11}$ from (Wojtak *et al.*, 2019).

Physical scenarios have been proposed that can leard to a correlation between diverse host galaxy properties such as stellar mass, specific star-formation rate (sSFR) or morphology (and thus the delay time distribution) and intrinsic SN properties such as stretch and luminosity. Although mechanisms have been proposed, none are currently preferred and current constraints on the DTD do not take the well-known (see Section 1.2.2) bimodality in stretch into account. Linking SNe observables to progenitor models via observations poses an opportunity towards constraining and driving theoretical progenitor models.
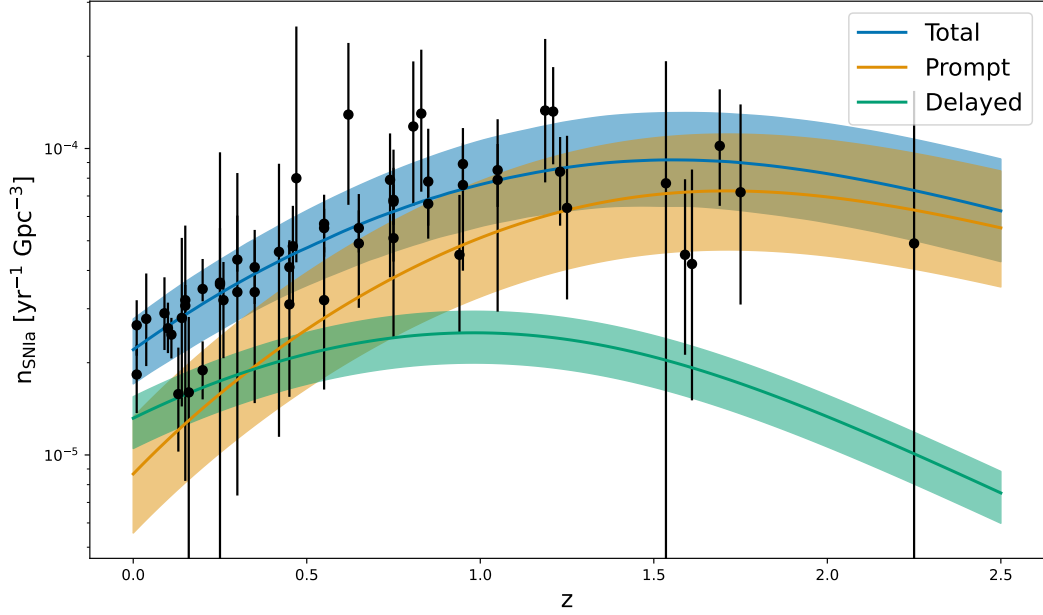
Figure 1.5.
Volumetric SNe Ia rate given by Eq. 1.32 and Eq. 1.33 compared with observations compiled in (Wojtak *et al.*, 2019). $\eta = 1.02^{+0.27}_{-0.15} \times 10^{-4} h_{70}^2 \text{ yr}^{-1} \text{ M}_\odot^{-1}$ and $f_p = 0.63^{+0.07}_{-0.11}$ from (Wojtak *et al.*, 2019) are used, with the shaded regions showing the 68% confidence interval.

1.3 Bayesian Inference in Cosmology

"... there is a valid defense for using non-Bayesian methods, namely incompetence."

- John Skilling, Fundamentals of MaxEnt in data analysis, 1991

Observational cosmology seeks to understand the universe and its evolution through the analysis of observational data. Bayesian statistics, a powerful framework for probabilistic reasoning, has become the approach of choice in much of astronomy and astrophysics throughout the last decades. It provides a consistent framework for incorporating prior information and updating beliefs in a principled manner. This is particularly valuable in situations where data are scarce, and prior knowledge can help guide the analysis. As such, an understanding of Bayesian statistics is necessary before we dive into current results from SNe Ia cosmology.

The primary objective of this chapter is to provide a comprehensive introduction to Bayesian statistics and its applications to inference problems, which forms the foundation for all subsequent modeling and analysis in this thesis. Section 1.3.1 will introduce the cornerstone of Bayesian statistics - Bayes' Theorem. We will explore its mathematical formulation and discuss how it underpins the entire Bayesian framework, allowing us to calculate posterior probabilities of a given model based on prior knowledge and observations. This section will build heavily on (Thrane

et al., 2019). The focus of Section 1.3.3 is model comparison within the Bayesian framework. Model comparison is a critical aspect in any inference problem as it enables researchers to evaluate competing hypotheses and different models given observed data. Two relatively recent developments in Bayesian inference and model comparison, suspicion and Bayesian model dimensionality, will be introduced in this section.

1.3.1 Bayes' Theorem

Suppose some data d has been observed, which we are attempting to describe using a model parameterized by the parameters θ. The goal is then to determine the probability distribution over parameters θ given the observed data. To determine this we start with the joint probability of observing d and θ, $p(d, \theta)$, given by

$$p(d, \theta) = p(d|\theta)p(\theta) = p(\theta|d)p(d), \tag{1.34}$$

where $p(d|\theta)$ is the conditional probability of observing d given some θ, and $p(\theta)$ ($p()$ is the prior distribution over parameters (data). We can rewrite this as

$$p(\theta|d) = \frac{p(d|\theta)p(\theta)}{p(d)} = \frac{\mathcal{L}(d|\theta)\pi(\theta)}{\mathcal{Z}}. \tag{1.35}$$

Eq. 1.35 is known as Bayes' Theorem, the central equation in Bayesian statistics and inference. The notation for each factor of Bayes' Theorem used in this work is shown on the right-hand-side of Eq. 1.35. The factors can be interpreted as follows:

- $\pi(\theta)$ is the prior distribution on the model parameters θ. This represents any prior knowledge, such as physical constraints, on the chosen model.

- $\mathcal{L}(d|\theta)$ is the likelihood function or likelihood. The likelihood is a probability distribution over the data d given some choice of the model parameters θ.

- $\mathcal{Z}$ is known as the (Bayesian) evidence and can be considered as a normalizing constant to ensure that Bayes' Theorem produces a valid distribution.

- $p(\theta|d)$ is the posterior distribution over the model parameters θ, that is the probability density over the chosen model given the observed data and prior knowledge.

If we have N independent observations $\mathbf{d} = d_1, \dots d_N$, then the posterior can be written as

$$p(\theta|\mathbf{d}) = \frac{\mathcal{L}(\mathbf{d}|\theta)\pi(\theta)}{\mathcal{Z}} = \frac{\pi(\theta)}{\mathcal{Z}} \prod_i^N \mathcal{L}(d_i|\theta). \qquad (1.36)$$

Given the definitions of the factors, the power of Bayes' Theorem in inference becomes clear. Bayes' Theorem provides a way of incorporating prior knowledge into statistical analysis, which in turn allows us to update our beliefs when new observations are made.

Baye's Theorem has subjectivity built into it via the choice of model and corresponding priors, which means one must be careful when choosing priors. When little or no information is available, the standard approach is to choose uninformative priors. These are often chosen to be uniform priors across a large range. Another choice is the maximum entropy distribution. In this case one picks the prior distribution $\pi(\theta)$ that maximizes the entropy given by

$$H(\pi) = \int_\theta \pi(\theta) \log(\pi(\theta)) d\theta \qquad (1.37)$$

given some chosen constraints on π, such as $\int_\theta \pi(\theta) d\theta = 1$ and $\pi(\theta) \geq 0 \, \forall \, \theta$. Information contained in the prior is minimized by maximizing the entropy. In this way, one can construct uninformative priors even in cases where some information is known, such as the case where $\theta \geq 0$.

It is rarely simple or tractable to sample from the posterior distribution defined by Bayes' theorem. Instead computationally intensive methods such as Markov Chain Monte Carlo (MCMC) and nested sampling must be used to sample from the posterior.

1.3.2 Hierarchical Models

As more and more SNe Ia are observed, it is increasingly interesting to study population properties when it comes to standardisation. These are properties common to all of the SNe Ia, such as the distributions of intrinsic luminosity, stretch and apparent color. Hierarchical Bayesian Inference is a formalism that allows inference of population-scale properties from individual observations.

To put this more concretely, let us again assume that we have N observations $\mathbf{d}$ that we try to describe using a model parameterized by θ. Sampling the posterior given each observation individually may yield different parameter predictions θ_i, which we

denote as the vector $\boldsymbol{\theta}$, also known as the latent parameters. In order to probe the population properties of an ensemble of events, we make the prior for θ dependent on a set of hyper-parameters ϕ, such that

$$\pi(\theta) = \pi(\theta|\phi). \tag{1.38}$$

The hyper-parameters ϕ parameterize the prior on the latent parameters θ. Assigning a prior to the hyper-parameters, known as the hyper-prior, we can rewrite Eq. 1.35 as

$$p(\boldsymbol{\theta}, \phi|\mathbf{d}) = \prod_i^N \frac{\mathcal{L}(d_i|\theta_i)\pi(\theta_i|\phi)\pi(\phi)}{\mathcal{Z}}. \tag{1.39}$$

The latent variables are typically not of interest and can in many cases lead to complications when sampling due to complicated posterior geometry and the curse of dimensionality (Betancourt, n.d.). The former is due to the relationship between hyper- and latent parameters leading to geometries such as Neal's Funnel, while the latter is due to dimensionality increasing as $\mathcal{O}(N)$ since each observation has a corresponding set of latent parameters θ_i. To circumvent this the latent parameters are marginalized over when possible, such that

$$p(\phi|\mathbf{d}) = \prod_i^N \int_\theta \frac{\mathcal{L}(d_i|\theta_i')\pi(\theta_i'|\phi)\pi(\phi)}{\mathcal{Z}} d\theta_i'. \tag{1.40}$$

In most cases this marginalization is not analytically tractable, and other methods must be taken into use, such as numerical integration, pseudo-marginalized methods or expectation propagation, see (Alenlöv *et al.*, 2019) and (Vehtari *et al.*, 2019).

1.3.3 Model Comparison

Within the Bayesian framework, hypotheses are defined via the likelihood and the chosen model parameterization. A necessary component for science is hypothesis testing, that is comparing, accepting and rejecting hypotheses based on observations. The equivalent of hypothesis testing in the Bayesian framework is model comparison. This methodology can also be extended to the case of dataset comparison to determine if two datasets can be combined, which is especially relevant in Section 4. In

this section we introduce different methods for model and dataset comparison used in this work, expanding both benefits and caveats with each approach.

Evidence & Bayes' Factors

The most commonly used approach for model comparison is via the Bayesian evidence and the Bayes' factor. For a given model M the Bayesian evidence is defined as

$$\mathcal{Z} = \int_\theta \mathcal{L}(d|\theta', M)\pi(\theta'|M)d\theta' = \mathcal{L}(d|M),\tag{1.41}$$

which we recognize as the normalizing constant from Eq. 1.35, where we have explicitly denoted the dependence on the chosen model. This describes the marginalized probability of the observed data given the chosen model parameterization, equivalent to the likelihood of the data given the model. Using the Bayesian evidence one can define how many more times M_1 is than M_2 between two models, known as the odds ratio, as

$$\frac{p(M_1|d)}{p(M_2|d} = \frac{\mathcal{L}(d|M_1)\pi(M_1)}{\mathcal{L}(d|M_2)\pi(M_2)} = \frac{\mathcal{Z}_1\pi(M_1)}{\mathcal{Z}_2\pi(M_2)} = B_{12}\frac{\pi(M_1)}{\pi(M_2)}.\tag{1.42}$$

Here B_{12} is the ratio of model evidences, known as the Bayes' factor, and $\pi(M_i)$ is the prior probability of the ith model. One can interpret the Bayes' factor as being the degree to which we update our relative belief in the chosen models after having observed data. The model priors can be chosen as $\pi(M_1) = \pi(M_2)$ if no prior information on model preference is assumed before observing data, which results in the Bayes' factor being equal to the odds ratio. In this case the Bayes' factor can be used directly to compare the two models. When $B_{12} = 1$ the models are equally supported by the data, while $B_{12} > 1$ shows support for M_1 and likewise $B_{12} < 1$ shows support for M_2.

Although the interpretation of the Bayes' factor is clear, the scale or significance of the Bayes' factor is more complicated. Model choice via the Bayes' factor is typically done using the Jeffrey's scale Nesseris *et al.*, 2013, shown in Table 1.1.

Log$_{10}$ Range	Strength of Evidence
$0 \leq \log_{10} B_{ij} < 1$	Weak
$1 \leq \log_{10} B_{ij} < 3$	Definite
$3 \leq \log_{10} B_{ij} < 5$	Strong
$5 \leq \log_{10} B_{ij}$	Very Strong

TABLE **1.1.**
Jeffrey's scale for logarithmic Bayes' factors between models i and j.

Although commonly used in the literature, both the Bayes' factor and the Jeffrey's scale exhibit pathologies that make their usage non-trivial. Nesseris *et al.*, 2013 show that the Bayes' factor is not necessarily a quantitative Occam's razor as is typically assumed, but instead a measure of model predictiveness. The study shows that given data from a simple model, the bounds given by the Jeffrey's scale fail to distinguish between the simple model and an over-parameterized model as one would otherwise expect. Related to this (Joachimi *et al.*, 2021) and (Keeley *et al.*, 2022) show that the evidence is dependent on the observed data, with the distribution of possible resulting Bayes' factors being able to exceed that of the Jeffrey's scale, making model comparison an inherently noisy process. (Llorente *et al.*, 2023) also highlight that the Bayes' factor is prior dependent since the log evidence is the expectation value of the likelihood with respect to the prior. If the bulk of the prior contains regions of low likelihood the evidence will be correspondingly lower, meaning that sufficiently diffuse priors can hide preference of a model by the data.

We will in this work make use of the Jeffrey's scale (Table 1.1), since the improved methodology presented (Joachimi *et al.*, 2021) and (Keeley *et al.*, 2022) is currently out of scope. In the next two sections we introduce metrics from (Handley *et al.*, 2019a) and (Handley *et al.*, 2019b)that, in addition to Bayes' factor, are designed to alleviate the Occam's razor issue as well as extend the framework to comparison of datasets.

Bayesian Model Dimensionality

One of the pathologies with the Bayes' factor is the misinterpretation of it a as a strict quantitative Occam's razor, as shown in (Nesseris *et al.*, 2013). Although the prior volume does increase with increasing number of parameters, this can be compensated for by overfitting from the additional parameters. To break this degeneracy one can make use of the Bayesian Model Dimensionality (BMD), fist introduced by

(Handley *et al.*, 2019a). The BMD, denoted by $\tilde{d}$ is a measure of the effective number of constrained parameters of a model that a given dataset can support.

The BMD is defined in (Handley *et al.*, 2019a) as

$$\frac{1}{2}\tilde{d} = \int_\theta p(\theta'|d) \left(\log \frac{p(\theta'|d)}{\pi(\theta')} - \mathcal{D} \right)^2 d\theta', \tag{1.43}$$

where $\mathcal{D}$ is the Kullback-Leibler divergence over the posterior with respect to the prior

$$\mathcal{D} = \int_\theta p(\theta'|d) \log \frac{p(\theta'|d)}{\pi(\theta')} d\theta'. \tag{1.44}$$

The Kullback-Leibler divergence can be understood as a quantification of the information provided by the observed data d, and is correspondingly the mean of the Shannon information. The Shannon information,

$$\mathcal{I}(\theta) = \log \frac{p(\theta|d)}{\pi(\theta)}, \tag{1.45}$$

represents the amount of information gained when moving from the prior to the posterior. It is clear that the Kullback-Liebler divergence is the mean of the Shannon information by definition, but that it does not contain any individual parameter information due to the marginalization over θ. This is why the BMD defined in Eq. 1.43 is given by the variance of the posterior Shannon information, with the special case of a Gaussian posterior giving $d = \tilde{d}$. A benefit of this definition is that it is weakly dependent on the choice of priors compared to the Bayesian evidence and the Kullback-Leibler divergence.

Another benefit of the BMD is that it can be used to break the previously mentioned degeneracy where a simple model M_1 and a correspondingly more complex model M_2 exhibit $\log_{10} B_{12} \sim 0$. If $\tilde{d}_1 > \tilde{d}_2$ then M_2 would be preferred by the data. (Handley *et al.*, 2019a) propose doing so by applying a post-hoc model prior

$$\pi(M_i) = e^{-\tilde{d}_i}. \tag{1.46}$$

Although not fully Bayesian due to $\pi(M_i)$ being computed from the data and thus not being a true prior, the addition directly introduces an Occam's razor penalty when comparing models.

Suspicion

In this work we will make use of two SNe Ia catalogs, SuperCal (Scolnic *et al.*, 2015) and Pantheon+ (Scolnic *et al.*, 2022) (see Sections 3.2 and 3.3). The focus of this work is the Pantheon+ catalog, but the SuperCal catalog is included for comparison's sake with the work done in W23. The Pantheon+ catalog can be viewed as a modern version of the SuperCal catalog, with an increased number of SNe Ia and updated preprocessing / data-reduction pipelines. This means it is prudent to compare results from the two datasets and gauge if any potential changes are due to the inclusion of new SNe Ia, systematics in new included surveys or the updated preprocessing pipelines. That is, we aim to quantify consistency between the two SNe Ia catalogs.

The Bayesian suspiciousness, introduced by (Handley *et al.*, 2019b), is a relatively new metric used to quantify consistency (or inversely, tension) between two datasets in a Bayesian manner. Assume two independent datasets A and B are observed, and a model parameterized by θ is chosen. The log Bayes' factor between the model given the combined datasets and the model given each dataset independently is

$$\log R_{AB} = \log \mathcal{Z}_{AB} - \log \mathcal{Z}_A - \log \mathcal{Z}_B. \tag{1.47}$$

We here use R_{ij} instead of B_{ij} (with i,j being alphabetic instead of numeric) to differentiate between Bayes' factors used for model comparison and dataset comparison. One can interpret this Bayes' factor as the relative confidence in dataset A after having observed B, compared to having only observed A. That is if $R_{AB} > 1$ then B strengthens the conclusions of A, while $R_{AB} << 1$ implies either a problem with the assumed model or a problem with either or both of the datasets, which prohibits combining them. As mentioned earlier, the Bayes' factor is prior dependent, and this is also the case for R_{ij}. Assuming A and B are consistent, increasing the width of parameter priors would lead to an increase in R_{ij} as it is then *a priori* less likely that parameters constrained by the datasets should be similar. Based on this argument, (Handley *et al.*, 2019b) argue that if any physically reasonable priors which do not significantly alter the posterior bulk that renders $R_{ij} < 1$, then the given datasets should be considered in tension. The Bayesian suspicion S removes this prior dependence by making use of the Kullback-Leibler divergence definend in Eq. 1.44, and is defined as

$$\log S_{ij} = \log R_{ij} + \mathcal{D}_{ij} - \mathcal{D}_i - \mathcal{D}_j = \log R_{ij} - \log I_{ij}. \tag{1.48}$$

Here $\log I_{ij} = \mathcal{D}_i + \mathcal{D}_j - \mathcal{D}_{ij}$ is the information ratio between the chosen model on A and B independently versus the combined data AB. Note that for $\mathcal{D}_i$ the subscript here denotes the dataset and not the model as in Eq 1.44. The suspiciousness S_{ij} has the qualities of the Bayes' factor R_{ij} while remaining insensitive to priors, assuming

the chosen priors do not dramatically change the posterior bulk. In the case of a Gaussian likelihood with d parameters and uniform priors (Handley *et al.*, 2019b) show that $\tilde{d} - 2\log S$ is χ^2-distributed, where $\tilde{d} = \tilde{d}_i + \tilde{d}_j - \tilde{ij}$ given by the BMD defined in Eq. 1.43. Using this a tension probability can be derived, given by

$$P = \int_d^\infty \chi_d^2(x)dx, \tag{1.49}$$

where χ^2 is chi-squared distribution and, meaning a χ^2-like test can be used to determine the tension. If $P \lesssim 0.05$ then the datasets in question should be considered in moderate tension and if $P \lesssim 0.003$ then they should be considered in strong tension, with the limits corresponding to 2σ and 3σ Gaussian standard deviations. It is emphasized in (Handley *et al.*, 2019b) that for non-Gaussian likelihoods only extremely small values of P should be regarded as indicators of tension.

It is important to highlight that this tension metric is derived for the case where data is uncorrelated. The method is extended to correlated datasets in (Lemos *et al.*, 2020), which requires taking into account a full covariance matrix between the datasets being compared. The model outlined in Section 2 is not yet capable of handling such an input, and the extension is deemed out of scope due to time constraints. Instead we will (incorrectly) assume datasets being compared are independent and leave a complete covariance matrix analysis for future work.

1.4 Current SNe Ia Results and Limitations

"One of the simplest reconcilings of the Hubble constant values is that some measurement is incorrect. Indeed, in the nearly 100 year history of the Hubble constant this has always been the answer..."

- Eric V. Linder, A Whole Cosmology View of the Hubble Constant, 2023

SNe Ia are most likely the best-established late-time (or low redshift) probes for testing and constraining cosmological models. The status of SNe Ia dates back to the measurement of the accelerating expansion of the Universe by Riess *et al.*, 1998 and Perlmutter *et al.*, 1999, which they have maintained since. Today, SNe Ia are perhaps more well known for the Hubble tension. This refers to a tension between measurement of H_0 using the cosmic microwave background (CMB) [CITE PLANCK] and late-time measurements of, such as SNe Ia standardized using the distance ladder. This tension began with the release of the 2013 Planck results [CITE PLANCK 13] and has since grown to a $4-6\sigma$ tension, depending on the dataset and methodology used.

This is shown in Fig. 1.6, comparing results derived from [CITE PLANCK 18] and the the largest cosmological SNe Ia catalog so far, Pantheon+ (Scolnic *et al.*, 2022). It is still debated whether this tension is due to physics beyond ΛCDM or as-of-yet-unaccounted-for systematics in either the CMB or SNe Ia measurements.
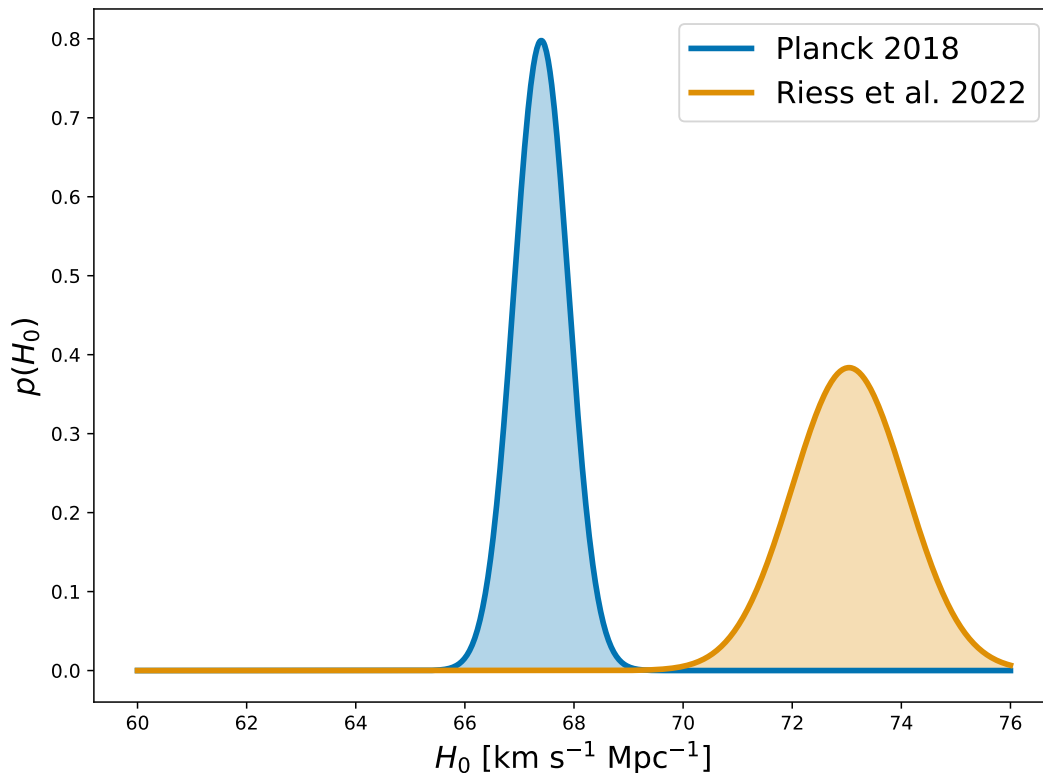
FIGURE 1.6.
Comparison of the Planck 2018 [CITE] and Riess *et al.*, 2022 measurements of the Hubble constant. Assymetric errors have been symmetrized for visualization purposes.

Disregarding the distance ladder, relative SNe Ia distances have been used as a complementary constraint on the matter density $\Omega_{m,0}$ and dark energy equation-of-state parameter w_0. Constraints on these parameters are orthogonal to those derived from early-time observations of the CMB and baryon acoustic oscillations, leading to overall tighter constraints. Pantheon+ combines both low- and high-redshift SNe Ia, allowing for joint constraints on H_0, $\Omega_{m,0}$ and w_0. This joint approach leads to tighter constraints, but also raises questions regarding the impact of systematics. *If systematics contribute to the Hubble tension, what impact may they have on cosmological constraints using either relative SNe Ia distances or a joint distance-ladder analysis?* That is the focus of this section, were we present the latest constraints for H_0, $\Omega_{m,0}$ and w_0 using SNe Ia in Section 1.4.1. After having introduced these results, we will discuss both the potential for new physics as well as potential impacts of systematics. The former is the focus of Section **??**, and the latter is covered Section 1.4.2.

1.4.1 SH0ES+Pantheon+ Constraints

The Pantheon+ catalog is the state-of-the-art compilation of type Ia SNe surveys, and underlies the to-date most stringent late-time constraints on the cosmological parameters H_0, $\Omega_{m,0}$ and w_0. This catalog combines SNe Ia from a multitude of different targeted and untargeted surveys (see Section 3.3), resulting in a single commonly-calibrated catalog that spans the redshift rang $0.001 < z < 2.26$. Within this range the Pantheon catalog contains 1550 distinct SNe Ia, including 42 calibrator SNe Ia from the SH0ES team (Scolnic *et al.*, 2022). The SH0ES (or Supernova H_0 for Equation of State) team focuses on increasing precision and reducing systematics in the cosmic distance latter, such as by detection of new calibrator SNe Ia. In addition to this the SH0ES Team focuses on better constraints on the first and second rungs of the distance ladder (cepheids and their calibration), as well as alternate calibration methods such as TRGB The joint efforts of the Pantheon+ and SH0ES teams have resulted in the landmark measurement $H_0 = 73.04 \pm 0.99$ km s^{-1} Mpc^{-1} presented in Riess *et al.*, 2022 and visualized in Fig. 1.6. This result was determined by making use of 277 Hubble flow SNe Ia ($0.023 < z < 0.15$) from Pantheon+ in combination with the 42 SH0ES calibrator SNe Ia. Work has continued to refine this measurement, attempting to eliminate both potential systematics in the distance ladder as well as in the SNe Ia themselves. The most recent is presented in Murakami *et al.*, 2023, where spectroscopically similar SNe Ia are used to improve constraints, giving $H_0 = 73.29 \pm 0.90$ km s^{-1} Mpc^{-1} and a Hubble tension of 5.7σ.

Brout *et al.*, 2022a perform joint cosmological analyses of the parameters H_0, $\Omega_{m,0}$ and w_0 as well as more exotic models using the full Pantheon+ catalog. The aim of this is two-fold: quantify the impact of and constraints on cosmological models with increased freedom compared to ΛCDM, and determine the impact of SNe Ia systematics on H_0. Brout *et al.*, 2022a investigate four cosmological models:

- FlatΛCDM: $\Omega_{m,0}$ is free to vary, while $w_0 = -1$ and $\Omega_{m,0} + \Omega_{\Lambda,0} = 1$.

- ΛCDM: $\Omega_{m,0}$ and $\Omega_{\Lambda,0}$ are free to vary, with $w_0 = -1$.

- Flat$w$CDM: w_0 and $\Omega_{m,0}$ are free to vary, with the constraint $\Omega_{m,0} + \Omega_{\Lambda,0} = 1$.

- Flat$w_0 w_a$CDM: Redshift-dependent dark energy equation-of-state model, also known as CPL cosmology (Brout *et al.*, 2022a), where $w(z) = w_0 + w_a(1 + z)$. The free parameters in this model are $\Omega_{m,0}$, w_0 and w_a, subject to the constraint that $\Omega_{m,0} + \Omega_{\Lambda,0} = 1$.

In this work we will be focusing on the FlatΛCDM and Flat$w$CDM models (see Chapter 7), and we present the Pantheon+ results here for comparison. For a FlatΛCDM model using only Pantheon+ SNe Ia, Brout *et al.*, 2022a find $\Omega_{m,0} = 0.326 \pm 0.016$, consistent with results found in the H_0 analysis by Riess *et al.*, 2022. For the Flat$w$CDM model, Brout *et al.*, 2022a find $\Omega_{m,0} = 0.309^{+0.063}_{-0.069}$ and $w_0 = -0.90 \pm 0.14$. These results are consistent with a cosmological constant, $w_0 = -1.$ as described in Section 1.1. It is interesting to note the change in matter density between the FlatΛCDM and Flat$w$CDM. This degeneracy via Eq. 1.6, where we see that $w_0 > -1.$ will lead to increased contribution from the dark energy component at higher redshift, compared to the case where $w_0 = -1$. In Table 3 and Fig. 9 of Brout *et al.*, 2022a results for joint analysis of Pantheon+ and other probes are shown. Pantheon+ is analysed with SH0ES and Planck independently, owing to the incompatibility of these datasets due to the aforementioned Hubble tension. Interestingly, a roughly 2σ tension is found between $\Omega_{m,0}$ measurements for a Flat$w$CDM, with $\Omega_{m,0} = 0.325^{+0.010}_{-0.008}$ and $\Omega_{m,0} = 0.309^{+0.063}_{-0.069}$ for Planck and SH0ES, respectively. No tension in w_0 is mentioned, owing to larger uncertainties for the Pantheon+ & SH0ES measurement. Based on simulations in (Popovic *et al.*, 2021), Brout *et al.*, 2022a report that systematic errors are a minor component of the overall error budget.

1.4.2 Potential Issues and Systematics

Presence or lack-there-of of systematics in SNe Ia analyses is topic of hot debate within the SNe Ia community. In this section we will describe some of the latest developments in this debate, and how they relate both to the Hubble tension as well as constrains on FlatΛCDM and Flat$w$CDM models described in the previous section.

In the context of the Hubble tension, the presence of systematics can be split roughly into two sectors, the distance ladder sector and the SNe Ia sector. The former relates to potential systematics and biases in the first rungs of the distance ladder, the most prominent being potential systematics in cepheid distances. Large effort has gone into showing that the systematic contribution from this rung is minor, with the most recent work using JWST to test the validity of the cephied period-luminosity relation. The latter, the SNe Ia sector, is the main focus of this work. As described in Section 1.2.2, knowledge on SNe Ia progenitors and explosion mechanisms are lacking and may contribute to systematics in cosmological analyses. Different approaches have been used to quantify this impact, e.g Popovic *et al.*, 2021 who's work is used to quantify systematics in Brout *et al.*, 2022a. Popovic *et al.*, 2021 use SNe Ia observations to constrain an assumed single asymmetric parent population in intrinsic color and stretch, which afterwards is used as input for simulations to determine selection

effectsand systematics in Brout *et al.*, 2022a. To capture any redshift dependence, Popovic *et al.*, 2021 split SNe Ia into low- and high-redshift bins and model population distributions separately. They report a bimodality in stretch in the low-redshift bin, which their assumed single component asymmetric distribution can not describe. Instead they adopt a two-component mixture of asymmetric distributions to better describe this bimodality at low redshift. This binning approach may miss redshift-dependent evolution in SNe Ia observables within a given bin. Such an unmodelled evolution could lead to biased distance estimates in studies such as Pantheon+ that cover a large redshift range.

To address a potential redshift evolution, Nicolas *et al.*, 2021 use LsSFR, which they argue is a tracer of progenitor age, to model redshift evolution of SNe Ia stretch. This approach ascribes a physical model to the observed bimodality and evolution in SNe Ia observables based on the two progenitor models described in Section 1.2.2. Although promising in the sense that it ascribes a physical explanation for the bimodality and evolution, LsSFR measurements are not available for high-redshift catalogs like Pantheon+. In a similar vein, Wojtak *et al.*, 2023 attempt to model observed bimodalities as well as reduce intrinsic dispersion by employing a two-population hierarchical model for SNe Ia light-curve observables. This model is parameterized as a mixture of two distributions, with a normalizing weighting parameterizing the amplitude of each component. Wojtak *et al.*, 2023 focus on SNe Ia in the Hubble flow, where a constant weighting can be assumed. They report strong support for a two component model compared to a single component model, finding that the observed SNe Ia can be described by a mixture of low-stretch / redder and high-stretch / bluer parent populations. Like Nicolas *et al.*, 2021, Wojtak *et al.*, 2023 argue that these potential sub-populations on SNe Ia light-curve observables could be due to two underlying progenitor channels. These results are an interesting addition to the debate on SNe Ia systematics, as Wojtak *et al.*, 2023 manage to fully remove the need for intrinsic dispersion. The model can not be applied, however, to high-redshift surveys in it's current state due to the assumption

This two-population model has the potential to solve multiple issues in SNe Ia cosmology. The first of these is regarding the Hubble tension. If a systematic bias towards one population was present in the calibration sample of SNe Ia during calibration with the second rung of the distance ladder, but a mixture of populations is present in the cosmological sample, biases may be incurred in inferred parameters such as the Hubble constant. Wojtak *et al.*, 2022 hints at this, finding an intrinsic tension in color between the calibration and cosmological samples. This model may also be applicable to high-redshift surveys. Wojtak *et al.*, 2023 assume a constant weighting between populations, which is an acceptable approximation in the Hubble flow. As outlined in Section1.2.2 and 1.2.3, theoretical models point at populations of SNe Ia

progenitors changing as a function of redshift. Over the next few chapters we will explore how we can extend the two-population model to include progenitor evolution, and apply it across a wider redshift range.

BayeSNova

2

"*Since all models are wrong the scientist must be alert to what is importantly wrong. It is inappropriate to be concerned about mice when there are tigers abroad.*"

<div style="text-align: right;">George Box, Science and Statistics, 1976</div>

The main product of this thesis is the Python package BAYESNOVA, an extension and standardisation of the work done in (Wojtak *et al.*, 2023). The purpose of this extension is to tackle issues and limitations pointed out in Section 1.4.2 and 1.2.1, enabling the usage of SNe Ia at high redshifts to constrain cosmological parameters. BAYESNOVA is built using the probabilistic programming language PYAUTOFIT (Nightingale *et al.*, 2021), which allows for modular construction of hierarchical models and ease-of-access to different sampling algorithms for MCMC and nested sampling. BAYESNOVA provides a set of model components implementing different variations and extensions of the Tripp calibration as well as for related data such as host properties, allowing users to construct models across a range of complexity to describe observed data.

We will first outline and describe the hierarchical model used in (Wojtak *et al.*, 2023), complementing the rationale described in Section 1.4.2. Consider a single SNe Ia with lightcurve observables given by $\mathbf{X}_i = \{m_{B,i}, x_{1,i}, c_i\}$ and observational covariance matrix $\mathbf{\Sigma}_i$. These observables can be further decomposed into intrinsic and extrinsic parameters $\boldsymbol{\theta}_i = \{M_{B,i}, X_{1,i}, c_{int,i}, E(B-V)_i, \alpha_i, \beta_i, R_{B,i}\}$ via the extended Tripp calibration introduced in Eq. 1.18:

$$\mathbf{X}_i(\boldsymbol{\theta}_i) = \begin{bmatrix} M_{B,i} + \alpha_i X_{x,i} + \beta_i c_{int,i} + R_{B,i} E(B-V)_i + \mu(z_i) \\ X_{1,i} \\ c_{int,i} + E(B-V)_i \end{bmatrix}. \qquad (2.1)$$

The intrinsic noise-free (latent) SNe Ia parameters are the peak absolute magnitude $M_{B,i}$, the light curve stretch $X_{1,i}$ and the intrinsic $B-V$ color $c_{int,i}$. The intrinsic parameters provide a phenomological description of the physical processes underlying the observed SNe Ia light curves. The extrinsic parameters are the dust reddening $E(B-V)_i$ and the extinction coefficient $R_{B,i}$, both of which are related to the SNe

Ia environment. Using this a Gaussian likelihood for the i'th SNe Ia can be written as

$$\mathcal{L}(\mathbf{X}_i|\boldsymbol{\theta}_i) = \mathcal{G}(\mathbf{X}_i|\mathbf{X}_i(\boldsymbol{\theta}_i), \boldsymbol{\Sigma}_i). \tag{2.2}$$

(Wojtak *et al.*, 2023) propose a hierarchichal model which describes the latent parameters as being generated by an underlying two-population distribution. This is given by the prior

$$\pi(\boldsymbol{\theta}_i|\boldsymbol{\phi}) = f_1\pi(\boldsymbol{\theta}_i|\boldsymbol{\phi}_1) + (1 - f_1)\pi(\boldsymbol{\theta}_i|\boldsymbol{\phi}_2), \tag{2.3}$$

where $f_1 \in [0, 1]$ is a normalizing weight parameter and $\phi = \phi_1 \cup \phi_2 \cup \{f_1\}$ is the full set of hyper-parameters that parameterize the priors on the latent parameters $\boldsymbol{\theta}_i$. (Wojtak *et al.*, 2023) assume independent Gaussian priors for the SNe Ia intrinsic properties as well as the extinction coefficient and the distance modulus,

$$\pi_j(M_{B,i}|\hat{M}_{B,j}, \sigma_{int,j}) = \mathcal{G}(M_{B,i}|\hat{M}_{B,j}, \sigma_{int,j}), \tag{2.4}$$

$$\pi_j(X_{1,i}|\hat{X}_{1,j}, \sigma_{X_{int,j}}) = \mathcal{G}(X_{1,i}|\hat{X}_{1,j}, \sigma_{X_{int,j}}), \tag{2.5}$$

$$\pi_j(c_{int,i}|\hat{c}_{int,j}, \sigma_{c_{int,j}}) = \mathcal{G}(c_{int,i}|\hat{c}_{int,j}, \sigma_{c_{int,j}}), \tag{2.6}$$

$$\pi_j(R_{B,i}|\hat{R}_{B,j}, \sigma_{R_B,j}) = \mathcal{G}, (R_{B,i}|\hat{R}_{B,j}, \sigma_{R_B,j}) \tag{2.7}$$

$$\pi_j(\mu_i|\hat{\mu}_j, \sigma_{\mu,j}) = \mathcal{G}(\mu_i|\hat{\mu}_j, \sigma_{\mu,j}), \tag{2.8}$$

where the subscript $j \in \{1, 2\}$ denotes the population. Delta distributions are assumed for the calibration parameters α and β,

$$\pi_j(\alpha_i|\hat{\alpha}_j) = \delta(\alpha_i, \hat{\alpha}_j) \tag{2.9}$$

$$\pi_j(\beta_i|\hat{\beta}_j) = \delta(\beta_i, \hat{\beta}_j). \tag{2.10}$$

The prior distribution for the dust reddening $E(B - V)_i$ is chosen to be a gamma distribution, parameterized by

$$\pi_j\left(y_{i,j} = E(B - V)_i/\tau_j\right) = \frac{y_{i,j}^{\gamma-1}\exp\{-y_{i,j}\}}{\Gamma(\gamma)}, \tag{2.11}$$

where $E(B-V)_i$ has been reparameterized using the scales τ_j of the prior gamma distributions for numerical stability. The latent-marginalized likelihood is then given by

$$\mathcal{L}(\mathbf{X}_i|\boldsymbol{\phi}) = \int_0^\infty f_1 \mathcal{G}(\mathbf{X}_i|\mathbf{X}_i(\boldsymbol{\phi}_1), \boldsymbol{\Sigma}_{i,1}) \pi_j (y_{i,1}) \, dy_1 + \tag{2.12}$$
$$\int_0^\infty (1-f_1)\mathcal{G}(\mathbf{X}_i|\mathbf{X}_i(\boldsymbol{\phi}_2), \boldsymbol{\Sigma}_{i,2}) \pi_j (y_{i,2}) \, dy_2,$$

where all latent parameters except $E(B-V)$ have been marginalized out analytically giving

$$\mathbf{X}_i(\boldsymbol{\phi}_j) = \begin{bmatrix} \hat{M}_{B,j} + \hat{\alpha}_j \hat{X}_{1,j} + \hat{\beta}_j \hat{c}_{int,j} + \hat{R}_{B,j} \tau_j y_j + \hat{\mu}(z_i) \\ \hat{X}_{1,j} \\ \hat{c}_{int,j} + \tau_j y_j \end{bmatrix} \tag{2.13}$$

and

$$\boldsymbol{\Sigma}_{i,j} = \boldsymbol{\Sigma}_i + \begin{bmatrix} \sigma_{int,j}^2 + \sigma_{\mu,i}^2 + \hat{\alpha}_j^2 \sigma_{X_1,j}^2 + \hat{\beta}_j^2 \sigma_{c_{int},j}^2 + y_j^2 \tau_j^2 \sigma_{R_B,j}^2 & \hat{\alpha}_j \sigma_{X_1,j}^2 & \hat{\beta}_j \sigma_{c_{int},j}^2 \\ \hat{\alpha}_j \sigma_{X_1,j}^2 & \sigma_{X_1,j}^2 & 0 \\ \hat{\beta}_j \sigma_{c_{int},j}^2 & 0 & \sigma_{c_{int},j}^2 \end{bmatrix}. \tag{2.14}$$

For cosmological SNe Ia in the Hubble flow the distance modulus $\hat{\mu}$ is given by the chosen cosmology. In this regime peculiar velocities are the dominant source of uncertainty in $\hat{\mu}$, and the corresponding uncertainty is given by

$$\sigma_\mu = \frac{5}{\log 10} \frac{\sigma_v}{c} \frac{1}{z_i}, \tag{2.15}$$

where (Wojtak *et al.*, 2023) assume $\sigma_v = 200$ km s^{-1}. The posterior distribution of population hyper-parameters $\boldsymbol{\phi}$ given N observed SNe Ia is then

$$p(\boldsymbol{\phi}|\boldsymbol{X}) \propto \prod_{i=1}^N \mathcal{L}(\mathbf{X}_i|\boldsymbol{\phi})\pi(\boldsymbol{\phi},) \tag{2.16}$$

where the proportionality is due to the unknown evidence $\mathcal{Z}$ and $\pi(\boldsymbol{\phi})$ are the hyper-priors for the hyper-parameters.

Throughout this work, we will refer to a baseline model, which corresponds to the baseline two-population model presented in (Wojtak *et al.*, 2023). We make use of the same hyperpriors as Wojtak *et al.*, 2023. For any new hyperparameters introduced, we make use of wide, uniform priors $U(\theta| - 100, 100)$ where applicable. If thes hyperparameters are strictly positive, which is the case for any uncertainties σ, we use the strictly uniform priors $U(\theta|0, 10)$.

2.1 Duplicate SNe Handling

Current SNe Ia analyses are based on compiled catalogs that combine observations from different surveys to obtain higher statistics, better coverage and reach higher redshifts. This work is no different, and as a consequence the case of duplicate observations of a single SNe Ia from different surveys and instruments must be considered. The two-population model from (Wojtak *et al.*, 2023), shown in Eq. 2.13, implicitly assumes that all observations are independent SNe Ia. If a catalog containing a large number of duplicate observations then the inferred population distributions may be biased towards certain regions of parameter space.

(Wojtak *et al.*, 2023) makes use of the SuperCal catalog, see Section 3.2, which contains a relatively low number of duplicate SNe Ia observation, and the authors assume that the number of duplicates does not have a major impact on the inferred results. This assumption does not hold for thee main focus of this work, the Pantheon+ catalog described in Section 3.3, which contains on the order of 10^3 duplicate observations. (Brout *et al.*, 2022a) perform their analysis on an N_{obs}-dimensional Gaussian where N_{obs} is the total number of SNe Ia observations, as opposed to the number of unique SNe Ia. The covariance between duplicate observations, as well as systematics related to photometric cross-calibration are given by a $N_{obs} \times N_{obs}$ covariance matrix. Although this approach would be an ideal extension of the two-population model, extension of the hierarchical likelihood to this case is non-trivial and deemed out-of-scope. We instead adopt an approach that combines duplicate observations into a single effective observation of the unique SN Ia. Consider the latent likelihood for the i'th unique SN Ia, defined in Eq. 2.2. Furthermore assume that M_i independent observations of this SN Ia are present in the catalog being used. Then the likelihood can be written as

$$\mathcal{L}(\tilde{\mathbf{X}}_i|\theta_i) = C_i \mathcal{G}(\tilde{\mathbf{X}}_i|\mathbf{X}_i(\boldsymbol{\theta}_i), \tilde{\boldsymbol{\Sigma}}_i) = \prod_{k=1}^{M_i} \mathcal{G}(\mathbf{X}_{i,k}|\mathbf{X}_i(\boldsymbol{\theta}_i), \boldsymbol{\Sigma}_{i,k}), \qquad (2.17)$$

where $\tilde{\mathbf{X}}_i$ and $\tilde{\boldsymbol{\Sigma}}_i$ denote the effective observation $\mathbf{X}$ and covariance $\boldsymbol{\Sigma}$ that corresponds to the combination of the M_i duplicate observations, and C_i is a normalization constant. This factorization assumes that all observations are independent, which we know is not the case based on (Brout *et al.*, 2022a). Furthermore we assume a singular redshift for all observations such that $\mathbf{X}_i(\boldsymbol{\theta}_i)$ is the same for all duplicate observations. Values for $\tilde{\mathbf{X}}_i$, $\tilde{\boldsymbol{\Sigma}}_i$ and C_i can be derived as follows. Given fixed observations we can rewrite Eq. 2.17 as

$$\prod_{k=1}^{M_i} \mathcal{G}(\mathbf{X}_i|\mathbf{X}_i(\boldsymbol{\theta}_i), \boldsymbol{\Sigma}_i) = \prod_{k=1}^{M_i} \mathcal{G}(\mathbf{X}_i(\boldsymbol{\theta}_i)|\mathbf{X}_i, \boldsymbol{\Sigma}_i), \qquad (2.18)$$

due to the Gaussian distribution being symmetric in the mean $\mathbf{X}_i(\boldsymbol{\theta}_i)$. Rewriting to canonical form we get

$$\prod_{k=1}^{M_i} \mathcal{G}(\mathbf{X}_i(\boldsymbol{\theta}_i)|\mathbf{X}_i, \boldsymbol{\Sigma}_i) = \prod_{k=1}^{M_i} \exp\left(\epsilon_{i,k} - \frac{1}{2}\mathbf{X}_i^T(\boldsymbol{\theta}_i)\boldsymbol{\Lambda}_{i,k}\mathbf{X}_i(\boldsymbol{\theta}_i) + \boldsymbol{\eta}_{i,k}^T\mathbf{X}_i(\boldsymbol{\theta}_i)\right) \quad (2.19)$$

$$= \exp\left(\sum_{k=1}^{M_i} \epsilon_{i,k} - \frac{1}{2}\mathbf{X}_i^T(\boldsymbol{\theta}_i)\left(\sum_{k=1}^{M_i}\boldsymbol{\Lambda}_{i,k}\right)\mathbf{X}_i(\boldsymbol{\theta}_i) + \left(\sum_{k=1}^{M_i}\boldsymbol{\eta}_{i,k}^T\right)\mathbf{X}_i(\boldsymbol{\theta}_i)\right),$$

where

$$\boldsymbol{\Lambda}_{i,k} = \boldsymbol{\Sigma}_{i,k}^{-1}, \quad \boldsymbol{\eta}_{i,k} = \boldsymbol{\Lambda}_{i,k}\mathbf{X}_{i,k}, \quad \epsilon_{i,k} = -\frac{1}{2}\left(\log|2\pi\boldsymbol{\Lambda}_{i,k}| + \boldsymbol{\eta}_{i,k}^T\boldsymbol{\Lambda}_{i,k}^{-1}\boldsymbol{\eta}_{i,k}\cdot\right) \quad (2.20)$$

By redefining

$$\tilde{\boldsymbol{\Lambda}}_i = \sum_{k=1}^{M_i}\boldsymbol{\Lambda}_{i,k}, \quad \tilde{\boldsymbol{\eta}}_i = \tilde{\boldsymbol{\Lambda}}_i\tilde{\boldsymbol{X}}_i, = \sum_{k=1}^{M_i}\boldsymbol{\eta}_{i,k}, \quad (2.21)$$

$$\tilde{\epsilon}_i = -\frac{1}{2}\left(\log|2\pi\tilde{\boldsymbol{\Lambda}}_i| + \tilde{\boldsymbol{\eta}}_i^T\tilde{\boldsymbol{\Lambda}}_i^{-1}\tilde{\boldsymbol{\eta}}_i\right), \quad \epsilon_i = \sum_{k=1}^{M_i}\epsilon_{i,k},$$

we can rewrite Eq. 2.20 as

$$\prod_{k=1}^{M_i} \mathcal{G}(\mathbf{X}_i(\boldsymbol{\theta}_i)|\mathbf{X}_i, \boldsymbol{\Sigma}_i) = \exp\left(\epsilon_i - \tilde{\epsilon}_i + \tilde{\epsilon}_i - \frac{1}{2}\mathbf{X}_i^T(\boldsymbol{\theta}_i)\tilde{\boldsymbol{\Lambda}}_i\mathbf{X}_i(\boldsymbol{\theta}_i) + \tilde{\boldsymbol{\eta}}_i^T\mathbf{X}_i(\boldsymbol{\theta}_i)\right) \quad (2.22)$$

$$= \exp\left(\epsilon_i - \tilde{\epsilon}_i\right)\exp\left(\tilde{\epsilon}_i - \frac{1}{2}\mathbf{X}_i^T(\boldsymbol{\theta}_i)\tilde{\boldsymbol{\Lambda}}_i\mathbf{X}_i(\boldsymbol{\theta}_i) + \tilde{\boldsymbol{\eta}}_i^T\mathbf{X}_i(\boldsymbol{\theta}_i)\right)$$

$$= C_i\mathcal{G}(\mathbf{X}_i(\boldsymbol{\theta}_i)|\tilde{\mathbf{X}}_i\tilde{\boldsymbol{\Sigma}}_i)$$

$$= C_i\mathcal{G}(\tilde{\mathbf{X}}_i|\mathbf{X}_i(\boldsymbol{\theta}_i), \tilde{\boldsymbol{\Sigma}}_i) \quad (2.23)$$

where

$$\tilde{\boldsymbol{\Sigma}}_i = \tilde{\boldsymbol{\Lambda}}_i^{-1} = \left[\sum_{k=1}^{M_i}\boldsymbol{\Lambda}_{i,k}\right]^{-1} = \left[\sum_{k=1}^{M_i}\boldsymbol{\Sigma}_{i,k}^{-1}\right]^{-1}, \quad (2.24)$$

$$\tilde{\mathbf{X}}_i = \tilde{\boldsymbol{\Lambda}}_i^{-1}\tilde{\boldsymbol{\eta}}_i = \left[\sum_{k=1}^{M_i}\boldsymbol{\Sigma}_{i,k}^{-1}\right]^{-1} \cdot \left[\sum_{k=1}^{M_i}\boldsymbol{\Sigma}_{i,k}^{-1}\mathbf{X}_{i,k}\right], \quad (2.25)$$

$$\log C_i = -\frac{1}{2}\left[\sum_{k=1}^{M_i}\left(\log|2\pi\boldsymbol{\Sigma}_{i,k}^{-1}| + \mathbf{X}_{i,k}^T\boldsymbol{\Sigma}_{i,k}^{-1}\mathbf{X}_{i,k}\cdot\right) + \log|2\pi\tilde{\boldsymbol{\Sigma}}_i| - \tilde{\mathbf{X}}_i^T\tilde{\boldsymbol{\Sigma}}_i\tilde{\mathbf{X}}_i\right]. \quad (2.26)$$

From this derivation we see that, under the assumption of independent duplicate observations and a singular redshift, the duplicate observations can be reduced down to a single effective observation $\tilde{\mathbf{X}}_i$ with covariance $\tilde{\boldsymbol{\Sigma}}_i$ given by Eq. 2.24 and Eq. 2.25. This reduction of observations is equivalent to a weighted average of multivariate ob-

servations with corresponding covariance. Eq. 2.26 gives the normalizing constant needed to ensure proper weighting of each unique SNe Ia observation.

As mentioned, we know *a priori* that the assumption of independence between duplicate observations does not hold. We leave extending the two-population model to the full light-curve covariance for future work. The assumption of singular redshift values for duplicates works for current data since the majority of SNe Ia have spectroscopically confirmed redshifts. Future large scale surveys will rely heavily on photometry due to the large number of observations, which could increase redshift uncertainties and covariances due to the usage of photometric and host galaxy redshifts. We leave extension of the model for non-singular redshifts for future work as well.

2.2 New Prior Options

The two-population model is hierarchical, and as such the choice of priors on latent variables has a significant impact on the shape of the prior. In this section we will introduce extensions made to the latent priors used in (Wojtak *et al.*, 2023), with the aim of increasing flexibility as well as physicality of the model.

2.2.1 Selective Extinction Prior

As outlined in Section 1.4.2, the two-population model proposes two major extensions compared to typical SNe Ia analyses: the introduction of two sub-populations of SNe Ia, and the usage of a Gamma distribution prior for the selective extinction $E(B-V)_i$. The selective extinction, or reddening, is a positively defined parameter (i.e line-of-sight dust does not make an object appear bluer), and the standard approach in SNe Ia analyses has been to model this using an exponential distribution (Mandel *et al.*, 2017; Brout *et al.*, 2021). This prior choice respects that $E(B-V)_i \geq 0$, but assigns majority of the probability mass close to 0, as seen in the left of Fig. 2.1. Intuitively this seems situation seems impropable, as it implies that the majority of SNe Ia are to be found in regions with a low amount of dust in the line-of-sight. (Wojtak *et al.*, 2023) propose a more flexible prior in the form of the Gamma distribution, shown in Eq. 2.11, parameterized by the shape parameter γ and scale τ. The gamma distribution is the maximum entropy distribution for positively defined variables with constrained means of the variable and it's logarithmic counterpart. As outlined in Section 1.3.1, the maximum entropy requirement is desirable for priors when constraints (such as $E(B-V)_i \geq 0$) are available. Furthermore the exponential distribution typically used in the literature is a special case of the
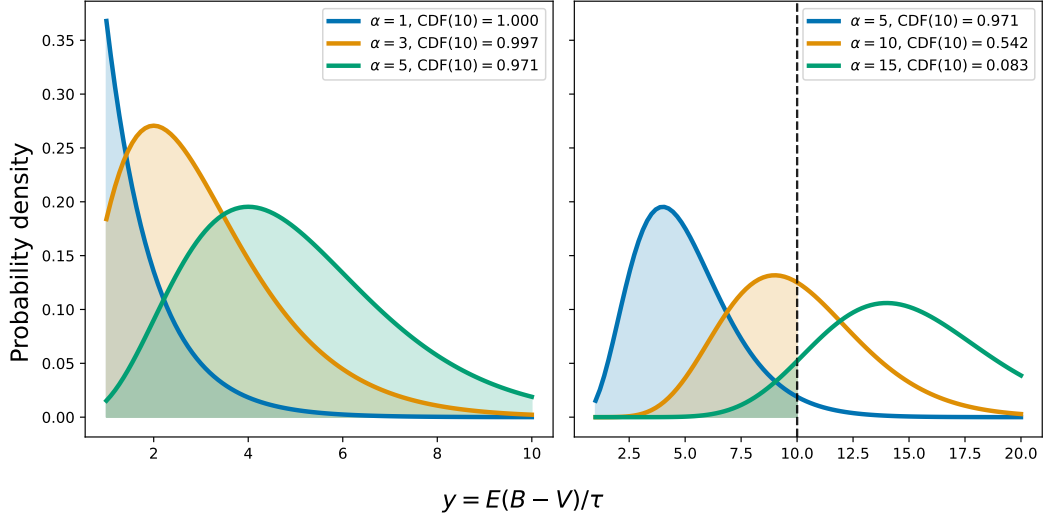
FIGURE 2.1.
Left: Comparison of different Gamma distributions with varying shape parameters γ. *Right*: Comparison of probability mass for different Gamma distributions integrated up to the limit $y = 10$, showing that values of high γ have correspondingly lower probability mass for a constant integration limit.

gamma distribution when $\gamma = 1$. For $\gamma > 1$ the Gamma distribution is peaked at $y = E(B - V)/\tau > 0$. This is shown in the right of Fig. 2.1.

The use of this prior is also why $E(B - V)_i$ in Eq. 2.13 must be marginalized numerically. In (Wojtak *et al.*, 2023) this is done in the range $0 \leq y \leq 10$, after which the distribution is renormalized, for numerical stability. We argue that this choice can bias the derived value of γ low due to low probability mass of distributions within the range $0 \leq y \leq 10$. for high values of γ. This can in turn impact other parameters such as R_B, c_{int} and β due to the relations shown in Eq. 2.1. Our proposed solution is to make use of a variable integration cutoff y_{max} that satisfies

$$P_{max} = \frac{1}{\Gamma(\gamma)} \int_0^{y_{max}} y^{\gamma-1} \exp\{-y\} dy, \tag{2.27}$$

where $P_{max} \leq 1$ is the chosen cutoff in probability mass. In practice this is done by precomputing a set of pairs $\{(y_{max}^1, \gamma^1) \dots (y_{max}^N, \gamma^N)\}$ within the hyper-prior range $\gamma \in [\gamma_{min}, \gamma_{max}]$, and then matching the sampled γ to an integration bound. Here N is given by $N = \frac{\gamma_{max} - \gamma_{min}}{\Delta\gamma}$ where $\Delta\gamma$ is some chosen resolution. The default setting in this work and in BAYESNOVA is $P_{max} = 0.995$ and $\Delta\gamma = 0.01$. The impact of this extension is shown in Section 4.

2.2.2 Extinction Coefficient Prior

(Wojtak *et al.*, 2023) use a Gaussian distribution $\mathcal{G}(R_B|\hat{R}_B, \sigma_{R_B})$ as a prior for the latent extinction coefficient R_B. The extinction coefficient can be related theoretically to dust grain size, which imposes constraints on the value of R_B, with (Draine, 2003) giving a lower expected limit of $R_B = 2.2$ for Rayleigh scattering. Although (Wojtak *et al.*, 2023) find that only low 2σ limits of their best fit model is comparable with this lower limit, concluding negligible influence, we will this section we will explore alternative priors that respect this theoretical limit.

The general constraint that $R_B \geq R_B^{min} > 0$, together with the assumption of a well localised mean implied by the choice of a Gaussian prior, makes the Gamma distribution a good candidate for a maximum entropy prior. Although such an approach would be ideal, it would incur large numerical costs due to needing to numerically integrate over two dimensions for every evaluation of the likelihood. Instead we follow the methodology used elsewhere in the SNe Ia literature (Brout *et al.*, 2021; Thorp *et al.*, 2021) and include a truncated Gaussian prior given by

$$\pi(R_B|\hat{R}_B, \sigma_{R_B}, R_B^{min}) = \begin{cases} \frac{\mathcal{G}R_B|\hat{R}_B, \sigma_{R_B})}{1-\Phi(R_B^{min})} & \text{if} R_B \geq R_B^{min} \\ 0 & \text{if} R_B < R_B^{min} \end{cases}, \tag{2.28}$$

where $\Phi(R_B^{min})$ denotes the CDF evaluated at R_B^{min} for the one-dimensional Gaussian $\mathcal{G}R_B|\hat{R}_B, \sigma_{R_B})$. Using this we can re-derive the marginalized likelihood given in Eq. 2.13. We start by assuming all other latent variables besides the dust reddening $E(B-V)_i$ and extinction coefficient $R_{B,i}$ have been marginalized analytically, such that we can define partially model subtracted observables for the j'th population

$$\mathbf{X}_{i,j}^P = \begin{bmatrix} m_{B,i} - \hat{M}_{B,j} - \hat{\alpha}\hat{X}_{1,j} - \hat{\beta}\hat{c}_{int,j} - \hat{\mu}(z_i) \\ x_{1,i} - \hat{X}_{1,j} \\ c_i - \hat{c}_{int,j} - E(B-V)_i \end{bmatrix} \tag{2.29}$$

$$\mathbf{\Sigma}_{i,j}^P = \mathbf{\Sigma}_i + \begin{bmatrix} \sigma_{int,j}^2 + \sigma_{\mu,i}^2 + \hat{\alpha}_j^2\sigma_{X_1,j}^2 + \hat{\beta}_j^2\sigma_{c_{int,j}}^2 & \hat{\alpha}_j\sigma_{X_1,j}^2 & \hat{\beta}_j\sigma_{c_{int,j}}^2 \\ \hat{\alpha}_j\sigma_{X_1,j}^2 & \sigma_{X_1,j}^2 & 0 \\ \hat{\beta}_j\sigma_{c_{int,j}}^2 & 0 & \sigma_{c_{int,j}}^2 \end{bmatrix},$$

and partially marginalized posterior

$$L_p(\mathbf{X}_{i,j}^P|R_{B,i}, E(B-V)_i) = \mathcal{G}(\mathbf{X}_{i,j}^P|\mathbf{M}_i \cdot \boldsymbol{R}_{\boldsymbol{B},\boldsymbol{i}}, \mathbf{\Sigma}_{i,j}^P), \tag{2.30}$$

where

$$
\boldsymbol{M}_i = \begin{bmatrix} E(B-V)_i \\ 0 \\ 0 \end{bmatrix}
$$

$$
\boldsymbol{R_{B,i}} = \begin{bmatrix} R_{B,i} \end{bmatrix}. \tag{2.31}
$$

Using the methodology described in (Hogg *et al.*, 2020), we can analytically marginalize the latent parameter $R_{B,i}$,

$$
\begin{aligned}
L_p(\mathbf{X}_{i,j}^P|\hat{R}_{B,j}, E(B-V)_i) &= \int_{-\infty}^{\infty} L_p(\mathbf{X}_{i,j}^P|R_{B,i}, E(B-V)_i)\pi(R_B|\hat{R}_B, \sigma_{R_B}, R_B^{min})dR_{B,i} \\
&= \frac{1}{1-\Phi(R_B^{min})} \int_{R_B^{min}}^{\infty} \mathcal{G}(\mathbf{X}_{i,j}^P|\mathbf{M}_i \cdot \boldsymbol{R_{B,i}}, \boldsymbol{\Sigma}_{i,j}^P)\mathcal{G}R_B|\hat{R}_B, \sigma_{R_B})dR_{B,i} \\
&= \frac{\mathcal{G}(\mathbf{X}_{ij}^P|\mathbf{b}, \mathbf{B})}{1-\Phi(R_B^{min})} \int_{R_B^{min}}^{\infty} \mathcal{G}(\boldsymbol{R_{B,i}}|\mathbf{a}, \mathbf{A})dR_{B,i} \\
&= \frac{1-\Phi_a(R_B^{min})}{1-\Phi(R_B^{min})}\mathcal{G}(\mathbf{X}_{ij}^P|\mathbf{b}, \mathbf{B})dR_{B,i}, \tag{2.32}
\end{aligned}
$$

where

$$
\mathbf{A}_{i,j}^{-1} = \frac{1}{\sigma_{R_{B,j}}^2} + \mathbf{M}_i^T \boldsymbol{\Sigma}_{i,j}^{P^{-1}} \mathbf{M}_i \tag{2.33}
$$

$$
\mathbf{a}_{i,j} = \mathbf{A}_{i,j} \cdot \left(\frac{1}{\sigma_{R_{B,j}}^2}\hat{R}_{B,j} + \mathbf{M}_i^T \Sigma_{i,j}^{P^{-1}}\mathbf{X}_{i,j}^P \right) \tag{2.34}
$$

$$
\mathbf{B}_{ij} = \boldsymbol{\Sigma}_{i,j}^P + \begin{bmatrix} \hat{R}_{B,i}^2 E^2(B-V)_i & 0 & 0 \\ 0 & 0 & 0 \\ 0 & 0 & 0 \end{bmatrix} \tag{2.35}
$$

$$
\mathbf{b}_{ij} = \hat{R}_{B,j}E(B-V)_i \tag{2.36}
$$

and $\Phi_a(R_B^{min})$ corresponds to the CDF of the 1D Gaussian $\mathcal{G}(\mathbf{R_{B},j}|\mathbf{a}, \mathbf{A})$ evaluated at R_B^{min}. We see from Eq. 2.32 that the latent-marginalized likelihood $\mathcal{L}_T(\mathbf{X}_i|\phi)$ using a truncated Gaussian prior on the latent parameter $R_{B,i}$ is given by

$$
\mathcal{L}_T(\mathbf{X}_i|\phi) = \frac{1-\Phi_a(R_B^{min})}{1-\Phi(R_B^{min})}\mathcal{L}(\mathbf{X}_i|\phi), \tag{2.37}
$$

where $\mathcal{L}(\mathbf{X}_i|\phi)$ is the latent-marginalized likelihood shown in Eq. 2.13. The introduction of a truncated Gaussian prior on $R_{B,i}$ modifies the likelihood by a scaling factor dependent on the observables as well as the hyper-parameters being sampled. R_B^{min} can be left as a free parameter, but the value used in this work and the default value for BAYESNOVA is chosen to be $R_B^{min} = 1.5$ in line with (Brout *et al.*, 2021).

2.3 Host Property Inclusion

As outlined in Section 1.2.1, empirical relations between host properties such as
global stellar mass have been used to improve calibration of SNe Ia. SNe Ia in mas-
sive, passive, older environments appear dimer after having been standardized by
their light-curve properties, leading to a step in luminosity that depends on host
properties. These steps are typically parameterized as (Scolnic *et al.*, 2022)

$$\delta_h = \Delta h \left[\frac{1}{2} - \left(1 + \exp\left((h - S_h)/\tau_h\right)\right)^{-1} \right], \tag{2.38}$$

where Δh is the magnitude of the SN Ia luminosity difference between SNe above
and below the step value S_h for the host property h. This is equivalent to a smooth
sigmoid transition of from a value of $-\Delta h/2$ for $h << S_h$ and $\Delta h/2$ for $h >> S_h$.
As described in Sections ?? multiple studies have shown correlations between local
and global host properties other than global stellar mass and differences in SNe Ia
properties. (Wiseman *et al.*, 2023) simulate SNe Ia with extinction coefficient R_V
that varies between young and old host galaxies as well as a difference in intrinsic
luminosity between young and old progenitor systems and use different host property
tracers to model the differences. They find that local specific star formation rate
(lsSFR) is a relatively pure tracer of the galaxy age difference, but can not rule out
any intrinsic difference in SNe Ia luminosity the case of multiple drivers. This serves
as an argument for using multiple local and global host properties as tracers of any
extrinsic and intrinsic differences in SNe Ia.

The two-population model introduced in (Wojtak *et al.*, 2023) attempts to model
the observed difference in SNe Ia apparent magnitude as being caused by two sub-
populations with distinct intrinsic and extrinsic properties and is purely driven by
light-curve observables. To include host properties in this framework the canonical
step approach must be reconsidered. We aim to describe the joint distribution over
SNe Ia light curve and host property observables, $\mathcal{L}(\mathbf{X}_i^{\mathrm{SN}}, \mathbf{X}_i^{\mathrm{H}} | \boldsymbol{\theta}_i^{\mathrm{SN}}, \boldsymbol{\theta}_i^{\mathrm{H}})$, where SNe Ia
/ host observable and latent variables are denoted by the superscripts SN and H. The
simplest approach to constructing such a model would be to extend the Tripp model

from Eq. 2.1 to $3 + N_H$ dimensions, where N_H denotes the number of host properties being considered

$$\mathbf{X}_i(\boldsymbol{\theta}_i) = \begin{bmatrix} \mathbf{X}_i^{\mathrm{SN}}(\boldsymbol{\theta}_i^{\mathrm{SN}}) \\ \mathbf{X}_i^{\mathrm{H}}(\boldsymbol{\theta}_i^{\mathrm{H}}) \end{bmatrix} \tag{2.39}$$

$$= \begin{bmatrix} M_{B,i} + \alpha_i X_{1,i} + \beta_i c_{int,i} + R_{B,i} E(B-V)_i + \mu(z_i) \\ X_{1,i} \\ c_{int,i} + E(B-V)_i \\ H_1, \\ \vdots \\ H_{N_H} \end{bmatrix}. \tag{2.40}$$

Here the host observables are $\mathbf{X}_i^{\mathrm{H}} = \{h_1, \ldots, h_{N_H}\}$ and the host latent variables are $\boldsymbol{\theta}_i^{\mathrm{H}} = \{H_1, \ldots, H_{N_H}\}$. We can then redefine the latent prior from Eq. 2.3 as

$$\begin{aligned} \pi(\boldsymbol{\theta}_i|\boldsymbol{\phi}) &= \pi(\boldsymbol{\theta}_i^{\mathrm{SN}}|\boldsymbol{\phi}^{\mathrm{SN}})\pi(\boldsymbol{\theta}_i^{\mathrm{H}}|\boldsymbol{\phi}^{\mathrm{H}}) \\ &= f_1\pi(\boldsymbol{\theta}_i^{\mathrm{SN}}|\boldsymbol{\phi}_1^{\mathrm{SN}})\pi(\boldsymbol{\theta}_i^{\mathrm{H}}|\boldsymbol{\phi}_1^{\mathrm{H}}) + (1-f_1)\pi(\boldsymbol{\theta}_i^{\mathrm{SN}}|\boldsymbol{\phi}_2^{\mathrm{SN}})\pi(\boldsymbol{\theta}_i^{\mathrm{H}}|\boldsymbol{\phi}_2^{\mathrm{H}}), \end{aligned} \tag{2.41}$$

where we assume Gaussian priors on the latent host variables,

$$\pi(H_{1,j}) = \mathcal{G}(H_1|\hat{H}_{1,j}, \sigma_{H_{1,j}})$$
$$\vdots \tag{2.42}$$
$$\pi(H_{N_H,j}) = \mathcal{G}(H_1|\hat{H}_{1,j}, \sigma_{H_{N_H,j}}).$$

This modified Tripp model and prior treats host properties as additional intrinsic properties that are independent of the light-curve observables. Having defined the likelihood and prior, the latent-marginalized likelihood can be constructed as in Eq. 2.2. The reasoning for this extension comes from the fact that host-property correlations are expressed as a step function. These steps can be considered binary approximations to two underlying groups / populations, eq. low vs high mass, star-forming vs quiescent, blue vs red. If $\phi_1 \neq \phi_2$ in Eq. 2.42 then each population of SNe Ia light-curve observables is associated with a corresponding population of host property observables. With this construction the goal is to further constrain the intrinsic and extrinsic properties by making use of the underlying correlations between bimodalities in light-curve and host observables. This model has been implemented in BAYESNOVA, see Chapter 5 for application to observational data.

As in (Wojtak *et al.*, 2023), this extended model can be used for typing of SNe Ia via the odds ratio of the mixture components. Following the same derivation,

$$\frac{p(\mathrm{SN}_{i,1}, \mathrm{H}_{i,1})}{p(\mathrm{SN}_{i,2}, \mathrm{H}_{i,2})} = \frac{p(\mathrm{SN}_{i,1})p(\mathrm{H}_{i,1})}{p(\mathrm{SN}_{i,2})p(\mathrm{H}_{i,2})}$$
$$= \frac{f_1 \int \mathcal{L}(\mathbf{X}_i^{\mathrm{SN}}|\phi_1^{\mathrm{SN}})\pi(\phi_1^{\mathrm{SN}})d\phi_1^{\mathrm{SN}} \int \mathcal{L}(\mathbf{X}_i^{\mathrm{H}}|\phi_1^{\mathrm{H}})\pi(\phi_1^{\mathrm{H}})d\phi_1^{\mathrm{H}}}{(1-f_1) \int \mathcal{L}(\mathbf{X}_i^{\mathrm{SN}}|\phi_2^{\mathrm{SN}})\pi(\phi_2^{\mathrm{SN}})d\phi_2^{\mathrm{SN}} \int \mathcal{L}(\mathbf{X}_i^{\mathrm{H}}|\phi_2^{\mathrm{H}})\pi(\phi_2^{\mathrm{H}})d\phi_2^{\mathrm{H}}} \quad (2.43)$$

where we note that $p(\mathrm{SN}_{i,j}, \mathrm{H}_{i,j})$ is separable due to the assumption of independence in Eq. 2.40. The benefit of Eq. 2.43 is that the SNe Ia observables can be marginalized over, giving a probabilistic typing

$$\frac{p(\mathrm{SN}_{i,1}, \mathrm{H}_{i,1})}{p(\mathrm{SN}_{i,2}, \mathrm{H}_{i,2})} \propto \frac{p(\mathrm{H}_{i,1})}{p(\mathrm{H}_{i,2})} = \frac{f_1 \int \mathcal{L}(\mathbf{X}_i^{\mathrm{H}}|\phi_1^{\mathrm{H}})\pi(\phi_1^{\mathrm{H}})d\phi_1^{\mathrm{H}}}{(1-f_1) \int \mathcal{L}(\mathbf{X}_i^{\mathrm{H}}|\phi_2^{\mathrm{H}})\pi(\phi_2^{\mathrm{H}})d\phi_2^{\mathrm{H}}} \quad (2.44)$$

which can be evaluated even when SNe Ia are not observed in a galaxy. We explore the relationship between light-curve and host-based typing in Chapter 5.

An issue with this method is that we assume the same weighting f_1 and $(1-f_1)$ can be applied between the two SNe Ia and host populations in Eq. 2.42. As (Briday *et al.*, 2022) discuss, global and local host properties are not necessarily perfect tracers of the underlying process leading to intrinsic dispersion in SNe Ia. This means that Eq. 2.42 may lead to shifts in both SNe Ia and host hyperparameters ϕ^{SN} and ϕ^H to best fit both sets of populations. An extreme edge-case would be where one host property is heavily weighted towards one population while not being fully unimodal, with the remaining SNe Ia and host populations being bimodal, which would artificially lower f_1. An alternative prior that addresses this issue is

$$\pi(\boldsymbol{\theta}_i|\boldsymbol{\phi}) = f_1\pi(\boldsymbol{\theta}_i|\phi_1^{\mathrm{SN}})\pi(\boldsymbol{\theta}_i|\phi_1^{\mathrm{H}}) + f_2\pi(\boldsymbol{\theta}_i|\phi_2^{\mathrm{SN}})\pi(\boldsymbol{\theta}_i|\phi_2^{\mathrm{H}})$$
$$+ f_3\pi(\boldsymbol{\theta}_i|\phi_1^{\mathrm{SN}})\pi(\boldsymbol{\theta}_i|\phi_2^{\mathrm{H}}) + f_4\pi(\boldsymbol{\theta}_i|\phi_2^{\mathrm{SN}})\pi(\boldsymbol{\theta}_i|\phi_1^{\mathrm{H}}), \quad (2.45)$$

where $\sum f_i = 1$. Compared to Eq. 2.42, this prior definition allows for cross-association between the SNe Ia and host property populations, breaking the strong assumption of equal weighting between the SNe Ia and host mixtures. Akin to Eq. 2.43, we can define the probabilistic typing for this prior as between SNe Ia given light-curve and host observables is

$$\frac{p(SN_{i,1})}{p(SN_{i,2})} = \frac{(f_1 + f_3) \int \mathcal{L}(\mathbf{X}_i^{\mathrm{SN}}|\phi_1^{\mathrm{SN}})\pi(\phi_1^{\mathrm{SN}})d\phi_1^{\mathrm{SN}}}{(f_2 + f_4) \int \mathcal{L}(\mathbf{X}_i^{\mathrm{SN}}|\phi_2^{\mathrm{SN}})\pi(\phi_2^{\mathrm{SN}})d\phi_2^{\mathrm{SN}}}, \quad (2.46)$$

where we have marginalized over the host property distributions. Note that $(f_1 + f_3)/(f_2 + f_4) = f_1^{SN}/(1 - f_1^{SN})$ from Eq. 2.13. This prior also allows for an baseline model where SNe Ia and host properties are fully independent,

$$
\begin{aligned}
\pi(\boldsymbol{\theta}_i|\boldsymbol{\phi}) = &\left[f_1^{\mathrm{SN}} \pi(\boldsymbol{\theta}_i|\boldsymbol{\phi}_1^{\mathrm{SN}}) + (1 - f_1^{\mathrm{SN}}) \pi(\boldsymbol{\theta}_i|\boldsymbol{\phi}_2^{\mathrm{SN}}) \right] \\
&\times \left[f_1^{\mathrm{H}} \pi(\boldsymbol{\theta}_i|\boldsymbol{\phi}_1^{\mathrm{H}}) + (1 - f_1^{\mathrm{H}}) \pi(\boldsymbol{\theta}_i|\boldsymbol{\phi}_2^{\mathrm{H}}) \right] .
\end{aligned}
\tag{2.47}
$$

This can be extendend further to break with the assumption that all host properties follow the same bimodal distribution, at the cost of increased model complexity. Due to the increased model complexity for Eq. 2.45, this proposed approach has not been explored during this work and is instead left for future work.

2.4 Redshift Dependent Populations

As outlined in Section 1.4, requires taking evolution of SNe Ia populations into account. This has previously been explored by Nicolas *et al.*, 2021, who use the redshift evolution of LsSFR to model and constrain the evolution of intrinsic SNe Ia stretch. In this work we propose a similar strategy to implement a redshift-dependent population weight $f_1^{SN}(z)$, replacing the constant f_1^{SN} used in (Wojtak *et al.*, 2023) and shown in Eq. 2.13, by making use of the volumetric SNe Ia rate introduced in Section 1.2.3. In Eq. 1.32 and Eq. 1.33 we decomposed the total volumetric SNe Ia rate into the rate of SNe Ia from the prompt and delayed channels, respectively. A redshift-dependent population weight can be constructed by taking the ratio between the delayed rate R_{Ia}^D and total rate R_{Ia},

$$
f_1^{SN}(z) = \frac{R_{Ia}^D(t(z))}{R_{Ia}(t(z))} = \frac{\int_{\tau_1}^t \frac{\chi(f^{-1}(t-\tau))}{\tau} d\tau.}{K \frac{f_p}{1-f_p} \int_{\tau_0}^{\tau_1} \chi\left(f^{-1}(t-\tau)\right) d\tau + \int_{\tau_1}^t \frac{\chi(f^{-1}(t-\tau))}{\tau} d\tau}
\tag{2.48}
$$

This choice of parameterization assumes a direct link between any bimodality in intrinsic (extrinsic) SNe (environment) properties and the theoretical two-channel progenitor framework used to define the volumetric SNe Ia rate. Although the normalization parameter η cancels in Eq. 2.48, we see that the prompt fraction f_p remains. This means that Eq. 2.48 can at least partially constrain the DTD introduced in Section 1.2.3 using purely SNe Ia observables. Such a model is highly sought-after in the literature due to the potential for linking SNe Ia explosions to specific progenitor models and guiding theory on how progenitor channels impact explosion mechanisms (Maoz *et al.*, 2012). We show an example of the redshift-dependent SNe Ia fraction $f_1^{SN}(z)$ in the right of Fig. 2.2, where we use $\eta = 1.02^{+0.27}_{-0.15} \times 10^{-4} h_{70}^2$ yr^{-1} M$_\odot^{-1}$ and $f_p = 0.63^{+0.07}_{-0.11}$ from (Wojtak *et al.*, 2019).
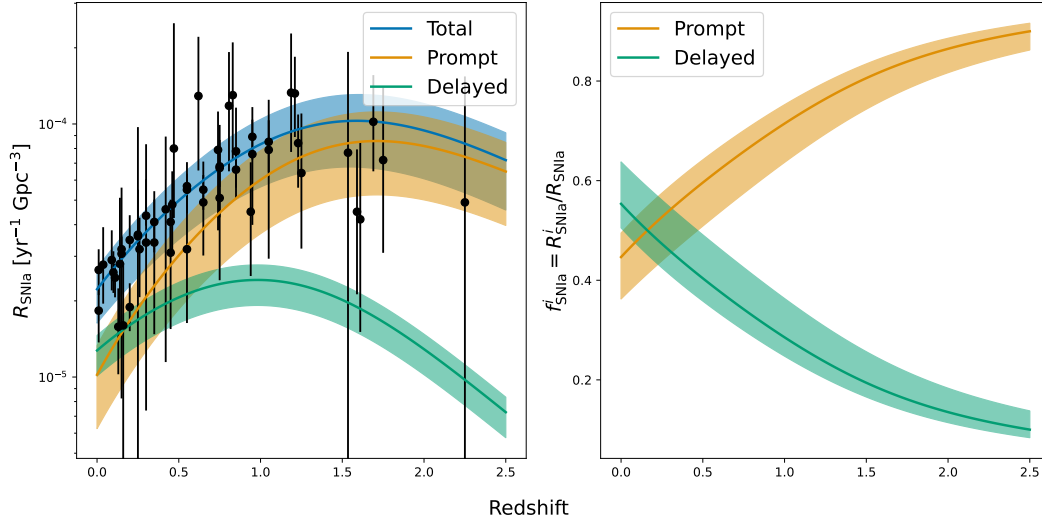
FIGURE 2.2.

Left: Volumetric SNe Ia rate given by Eq. 1.32 and Eq. 1.33 compared with observations compiled in (Wojtak *et al.*, 2019). $\eta = 1.02^{+0.27}_{-0.15} \times 10^{-4} h^2_{70}$ yr^{-1} M$_\odot^{-1}$ and $f_p = 0.63^{+0.07}_{-0.11}$ from (Wojtak *et al.*, 2019) are used, with the shaded regions showing the 68% confidence interval. *Right*: Redshift-dependent SNe Ia population fraction $f_1^{SN}(z)$ given by Eq. 2.48, using the same DTD parameters as in earlier.

With this choice of parameters we see that the majority of SNe Ia come from the prompt channel, with SNe Ia from the delayed progenitor channel only becoming the majority contribution at low redshift. We can understand this by considering the right side of Fig. 2.2, were we reproduce Fig. 1.5. We can see that the prompt volumetric rate peaks at $z \sim 1.5$, corresponding to the observed peak in cSFH at $z \sim 2$. (Madau *et al.*, 2014), after which the rate of SNe Ia from the prompt progenitor channel decreases rapidly. Since the delayed progentior channel is less sensitive to the cSFH, we see that the rate of SNe Ia from the delayed progenitor channel decreases at a slower pace, leading to $f_1^{SN} \approx 0.6$ at $z = 0$.

Reparameterizing the Redshift-Dependent Rate

Note that in Eq. 2.48 that the cSFH χ takes the redshift $\tilde{z} = f^{-1}(t(z) - \tau)$ as input. This poses an issue for the computational tractability of the SNe Ia model, as the calculation of $z(t)$ is computationally expensive. The remainder of this section will focus on reparameterizing 2.48 in terms of a "delay redshift" $\tilde{z}$ instead of delay time

τ, due to $t(z)$ being computationally cheaper. To do this we define the following values

$$t = f(z) = T_0 - \int_0^z \frac{t_H}{(1+z')E(z')} dz', \tag{2.49}$$

$$\Delta t = t - \tau = f(z) - \tau, \tag{2.50}$$

$$\tilde{z} = f^{-1}(f(z) - \tau), \tag{2.51}$$

$$R_{Ia}(z) = \int_{\tau_0}^{\tau_1} \chi\left(f^{-1}(f(z) - \tau)\right)\Psi(\tau)d\tau + \int_{\tau_1}^{f(z)} \chi\left(f^{-1}(f(z) - \tau)\right)\Psi(\tau)d\tau. \tag{2.52}$$

Here Eq. 2.49 is the age of the Universe for a given redshift, which depends on the age T_0 at $z = 0$, the Hubble time $t_H = 1/H_0$, and the Hubble parameter redshift scaling function, $E(z)$. Eq. 2.51 is the "delay redshift" at a given time, and Eq. 2.52 is the volumetric SNe Ia rate from Section 1.2.3 restated in terms of z and $f(z)$. We first perform a change of variable in Eq. 2.52 from τ to Δt,

$$R_{Ia}(z) = -\int_{\Delta t(\tau_0)}^{\Delta t(\tau_1)} \chi\left(f^{-1}(\Delta t)\right)\Psi\left(f(z) - \Delta t\right)d\Delta t -$$
$$\int_{\Delta t(\tau_1)}^{\Delta t(f(z))} \chi\left(f^{-1}(\Delta t)\right)\Psi\left(f(z) - \Delta t\right)d\Delta t \tag{2.53}$$
$$= \int_0^{f(z)-\tau_1} \chi\left(f^{-1}(\Delta t)\right)\Psi\left(f(z) - \Delta t\right)d\Delta t +$$
$$\int_{f(z)-\tau_1}^{f(z)-\tau_0} \chi\left(f^{-1}(\Delta t)\right)\Psi\left(f(z) - \Delta t\right)d\Delta t \tag{2.54}$$

Using Eq. 2.49 and Eq. 2.50 we can define the Jacobian as

$$\frac{d\Delta t}{d\tilde{z}} = \frac{d}{d\tilde{z}}f(\tilde{z}) = -\frac{t_H}{((1+\tilde{z})E(\tilde{z})}, \tag{2.55}$$

and use this to perform a second change of variable from Δt to $\tilde{z}$.

$$R_{Ia}(z) = -t_H \int_{\tilde{z}(0)}^{\tilde{z}(f(z)-\tau_1)} \frac{\chi(\tilde{z})\Psi\left(f(z) - f(\tilde{z})\right)}{(1+\tilde{z})E(\tilde{z})} d\tilde{z} -$$
$$t_H \int_{\tilde{z}(f(z)-\tau_1)}^{\tilde{z}(f(z)-\tau_0)} \frac{\chi(\tilde{z})\Psi\left(f(z) - f(\tilde{z})\right)}{(1+\tilde{z})E(\tilde{z})} d\tilde{z} \tag{2.56}$$
$$= t_H \int_{\tilde{z}_0}^{\tilde{z}_1} \frac{\chi(\tilde{z})\Psi\left(f(z) - f(\tilde{z})\right)}{(1+\tilde{z})E(\tilde{z})} d\tilde{z} +$$
$$t_H \int_{\tilde{z}_1}^{\infty} \frac{\chi(\tilde{z})\Psi\left(f(z) - f(\tilde{z})\right)}{(1+\tilde{z})E(\tilde{z})} d\tilde{z}. \tag{2.57}$$

Eq. 2.57 shows the generic volumetric SNe Ia rate as a function of redshift, where the integral is taken with respect to a delay redshift $\tilde{z}$. The integration limits are a

function of the input redshift z and the DTD bifurcation limits τ_0 and τ_1 defined in Section 1.2.3,

$$\tilde{z}_0 = f^{-1}(f(z) - \tau_1), \tag{2.58}$$

$$\tilde{z}_1 = f^{-1}(f(z) - \tau_0), \tag{2.59}$$

$$\tilde{z}_{max} = f{-1}(0) = \infty. \tag{2.60}$$

Inserting the chosen cSFH and DTD from Section 1.2.3, we get a volumetric SNe Ia rate

$$R_{Ia}(z) = \frac{t_H K \eta f_p}{1 - f_p} \int_{\tilde{z}_0}^{\tilde{z}_1} \frac{\chi(\tilde{z}) \Psi(f(z) - f(\tilde{z}))}{(1 + \tilde{z}) E(\tilde{z})} d\tilde{z} +$$
$$t_H \eta \int_{\tilde{z}_1}^{\infty} \frac{\chi(\tilde{z}) \Psi(f(z) - f(\tilde{z}))}{(1 + \tilde{z}) E(\tilde{z})} \frac{1}{f(z) - f(\tilde{z})} d\tilde{z}, \tag{2.61}$$

and a redshift-dependent SNe Ia population weight given by

$$f_1^{SN}(z) = \frac{\int_{\tilde{z}_1}^{\infty} \frac{\chi(\tilde{z})\Psi(f(z)-f(\tilde{z}))}{(1+\tilde{z})E(\tilde{z})} \frac{1}{f(z)-f(\tilde{z})} d\tilde{z}}{\frac{K f_p}{1-f_p} \int_{\tilde{z}_0}^{\tilde{z}_1} \frac{\chi(\tilde{z})\Psi(f(z)-f(\tilde{z}))}{(1+\tilde{z})E(\tilde{z})} d\tilde{z} + \int_{\tilde{z}_1}^{\infty} \frac{\chi(\tilde{z})\Psi(f(z)-f(\tilde{z}))}{(1+\tilde{z})E(\tilde{z})} \frac{1}{f(z)-f(\tilde{z})} d\tilde{z}}. \tag{2.62}$$

Although Eq. 2.62 is seemingly more complicated than Eq. 2.48, the computational cost is considerably lower.

Data 3

Upcoming large-scale surveys such as LSST and Euclid are expected to discover upwards of 10^5 and 10^3 SNe yearly over a large redshift range (Wojtak *et al.*, 2019). This dwarfs the number of SNe Ia observed over the last 40 years, and is orders of magnitude higher than current transient surveys (Scolnic *et al.*, 2022). The expected SNe Ia rates open up the possibility of doing cosmological analyses using single surveys. This has of course historically not been the case. Instead, progress in SNe Ia analysis has come from compilations of multiple surveys (Jones *et al.*, 2019; Scolnic *et al.*, 2015; Scolnic *et al.*, 2022). The reason for this is that different surveys have been optimized to discover SNe in different redshift ranges. As outlined in Sections 1.1 and 1.2.1, cosmological and astrophysical analyses using SNe Ia benefit from leveraging measurements at different redshifts. Due to this, combining different surveys into compilation datasets currently lead to the tightest constraints on both cosmological parameters and SNe Ia rates.

In this thesis we make use of two different compilations of SNe Ia observations, SuperCal and Pantheon+ (Scolnic *et al.*, 2015; Scolnic *et al.*, 2022). The SuperCal compilation is an older compilation, which contributed to an increase in Hubble tension due to large reductions in systematics. This compilation was also used in (Wojtak *et al.*, 2023), making it instrumental in testing the extensions outlined in Section 2. The Pantheon+ compilation is the modern successor to SuperCal, including new surveys and observations, making use of updated photometric cross-calibrations, and updated light curve models. This compilation has been used for the state-of-the-art measurements of, as described in Section 1.4.1.

The Pantheon+ compilation will be the main focus of this thesis, leaving one wondering why the SuperCal compilation is included. There are two main reasons for this, the first being that SuperCal allows for comparison of BAYESNOVA with the results presented in (Wojtak *et al.*, 2023). The second reason is for a comparison of SuperCal and Pantheon+. As mentioned, Pantheon+ is a modern successor to SuperCal with updated preprocessing methods. It is relevant to compare the two datasets such that we can discern whether any resulting differences between observations in SuperCal and Pantheon+ are due simply to the inclusion of more SNe Ia observations, or instead are due to differences in preprocessing methods.

In addition to SuperCal and Pantheon+ we also include three additional derived datasets. The first is a reanalysis of SNe Ia global and local host properties used in (Jones *et al.*, 2018), hereafter J18. Cross-matching SuperCal with the J18 host properties allows for a combined analysis, as outlined in Chapter 2. In addition to the global and local host properties of J18, we also include host galaxy morphology measurements from the HyperLeda database. The final derived dataset is a compilation of observational determinations of the volumetric SNe Ia rate as used in (Wojtak *et al.*, 2019), allowing for combined constraints on population evolution as outlined in Chapter 2.

The outline of this section is as follows. Section 3.1 outlines the preprocessing pipeline used to construct the SuperCal and Pantheon+ sub-samples used in this work. Sections 3.2 and 3.3 describe the SuperCal and Pantheon+ compilations, respectively. Finally, Sections 3.4 and 3.5 describe the supplementary datasets used in this work.

3.1   Preprocessing Pipeline

We must preprocess the SuperCal or Pantheon+ compilations before we can make use of either in the BAYESNOVA framework. Preprocessing is necessary to ensure the quality and cosmological usefulness of the sub-samples used in this work, in addition to including supplementary observations. Preprocessing can be split up into 3 steps, which we refer to as the preprocessing pipeline:

1. Quality cuts applied to the SNe Ia light curve observables to ensure that SNe are sufficiently well modelled by SALT. Additional filters are also applied during this step.

2. Internal cross-matching of duplicate SNe Ia based on SNe IDs and sky-positions to enable the duplicate handling features of BAYESNOVA.

3. External cross-matching with J18 and HyperLeda to include observed global and local host galaxy properties, enabling the host property analysis features of BAYESNOVA.

Each of these steps are described in detail in the following subsections. Fiducial values of relevant variables are given when constant across all sub-samples in this work. Sub-sample specific values are given in their respective subsections, see Sections 3.2 and 3.3.

3.1.1 Quality Cuts & Filters

Both SuperCal and Pantheon+ have been preprocessed using a series of quality cuts to ensure the quality of the compilations (Scolnic *et al.*, 2015; Scolnic *et al.*, 2022). We reapply some of these cuts together with additional quality cuts to ensure high-quality and cosmologically useful sub-samples. Following (Wojtak *et al.*, 2023) we apply the following series of quality cuts:

1. $|x_1| < x_{1,\text{cut}}$: A standard quality cut on the SALT stretch parameter to ensure that the SNe Ia light curves are well-sampled and modelled by SALT. $x_{1,\text{cut}}$ is fixed to $x_{1,\text{cut}} = 3.$ for all sub-samples.

2. $|c_{\text{app}}| < c_{\text{app,cut}}$: A standard quality cut on the SALT apparent color parameter to ensure that the SNe Ia light curves are well-sampled and modelled by SALT. $c_{\text{app,cut}}$ is fixed to $c_{\text{app,cut}} = 0.3$ for all sub-samples.

3. $\sigma_{x_1} < \sigma_{\text{x}_1,\text{cut}}$: A standard quality cut on the uncertainty of the SALT stretch parameter. Ensures that pathological light curve fits are avoided and that the resulting covariance matrices are invertible. $\sigma_{\text{x}_1,\text{cut}}$ is fixed to $\sigma_{\text{x}_1,\text{cut}} = 1.5$ for all sub-samples.

4. $\text{P}_{\text{fit}} > \text{P}_{\text{fit,cut}}$: A standard quality cut on the χ^2 of the SALT light-curve fit. The value of $\text{P}_{\text{fit,cut}}$ is sub-sample dependent, and is in some cases survey dependent. This choice stems from different approaches in the literature, with studies using SuperCal use a constant $\text{P}_{\text{fit,cut}}$ and studies using Pantheon+ using a survey-dependent $\text{P}_{\text{fit,cut}}$ based on simulations.

5. $\sigma_{\text{t}_{\text{peak}}} < \sigma_{\text{t}_{\text{peak}},\text{cut}}$: A standard quality cut on the uncertainty of the SALT-derived peak time, ensuring proper measurement of light curve parameters. $\sigma_{\text{t}_{\text{peak}},\text{cut}}$ is fixed to $\sigma_{\text{t}_{\text{peak}},\text{cut}} = 2$ days for all sub-samples.

6. $\sigma_{\text{m}_{\text{Tripp}}} < \sigma_{\text{m}_{\text{Tripp}},\text{cut}}$: A standard quality cut to remove light curves with prohibitively large uncertainties on the corrected peak magnitude, approximated by the Tripp formula given in Eq. REF TRIPP FORMULA. The error is given by

$$\sigma_{\text{m}_{\text{Tripp}}} = \sqrt{\sigma_{\text{int}}^2 + \sigma_\mu^2 + \alpha^2 \sigma_{x_1} + \beta^2 c_{\text{app}}^2}. \tag{3.1}$$

We fix $\sigma_{\text{int}} = 0.12$ mag, $|\alpha| = 0.148$ mag, $|\beta| = 3.122$ and $\sigma_{\text{m}_{\text{Tripp}},\text{cut}} = 0.2$ mag for all sub-samples. The fiducial values of σ_{int}, α and β are chosen in accordance with FIDUCIAL VALUE CITATION HERE.

7. $\frac{\Delta m_B}{\sigma_{\text{m}_\text{Tripp}}} < \left(\frac{\Delta m_B}{\sigma_{\text{m}_\text{Tripp}}} \right)_{cut}$: A standard Hubble residual cut to remove potential con-taminants that are likely non-normal SNe Ia or have misidentified redshifts. $\Delta m_{B,i} = m_i - m_{\text{Tripp,i}}$ for the ith light curve, with $m_{\text{Tripp,i}}$ given by Eq. 1.16. The fiducial value of the intrinsic absolute magnitude is $M_{int} = -19.253$ mag (Brout *et al.*, 2022a; Riess *et al.*, 2022),, with α and β set to the same values as in the previous quality cut. σ_{m_Tripp} is given by Eq. 3.1. The cut-off value is set to $\left(\frac{\Delta m_B}{\sigma_{\text{m}_\text{Tripp}}} \right)_{cut} = 3.5$, following Brout *et al.*, 2022a. Fiducial values for this quality cut are constant across sub-samples.

In addition to the quality cuts above, we also employ a set of filters that vary across different sub-samples. These filters allow for the definition of sub-samples in specific redshift ranges across either the full sub-sample or based on surveys, as well as choosing which surveys are included in the sub-sample. The use of these filters are by definition sub-sample dependent.

3.1.2 Cross-Matching Duplicate SNe

Both SuperCal and Pantheon+ are compilations of multiple SNeIasurveys, which means that a single SNe Ia can have multiple independent observations. As outlined in Section 2.1, we take the approach of combining duplicate observations into a single effective observation under the assumption of surveys being independent. To do this, duplicates need to be uniquely identified, which is not the case for the SuperCal or Pantheon+ compilations. Different surveys have different naming schemes, which means we must cross-match SNe observations within the given compilation.

We make use of SNe IDs, peak times, positions and redshifts to cross-match duplicate observations within a given compilation. Two SNe Ia observations i and j are deemed to be duplicate observations either if they have the same SNe IDs or if they fulfill the following criteria:

$$|t_{\text{peak},i} - t_{\text{peak},j}| < \Delta t_{\text{peak,max}}, \tag{3.2}$$

$$|z_i - z_j| < \Delta z_{\text{max}}, \tag{3.3}$$

$$\text{sep}(P_i, P_j) < \Delta P_{\text{max}}. \tag{3.4}$$

Here t_{peak} is the B-band peak time, z is the CMB-frame redshift, P the sky-position (RA,DEC), sep(P_i,P_j) is the separation between two positions in arc-seconds and $\Delta t_{\text{peak,max}}$, Δz_{max}, ΔP_{max} are the corresponding cut-off values. For all sub-samples we set $\Delta t_{\text{peak,max}} = 10$ days, $\Delta z_{\text{max}} = 10^{-4}$ and $\Delta P_{\text{max}} = 1$ arc-second.

Cross-matching of duplicates using these constraints is outlined in Algorithm 1. The output is an $M \times N_{\text{obs}}$ boolean array, INDECES, where M is the no. of SNe that have duplicate observations and N_{obs} is the total no. of SNe Ia observations. Using this array, we can assign a unique duplicate ID to each group of duplicate SNe Ia observations defined by each row in INDECES.

Algorithm 1 Duplicate SNe Cross-Matching Algorithm

Require: $N_{\text{obs}} > 0$
Require: $\Delta t_{\text{peak,max}} \geq 0$
Require: $\text{sep}_{\text{max}} \geq 0$

$\quad i \leftarrow 0$
$\quad \text{Indeces} \leftarrow [\ ]$
$\quad \text{IDs} \leftarrow [\text{ID}_0, \ldots, \text{ID}_{N_{\text{obs}}}]$
$\quad \text{Redshifts} \leftarrow [z_0, \ldots, z_{N_{\text{obs}}}]$
$\quad T_{\text{peak}} \leftarrow [t_{\text{peak}}, 0, \ldots, t_{\text{peak},N_{\text{obs}}}]$
$\quad \text{Coords} \leftarrow [P_0, \ldots, PC_{N_{\text{obs}}}]$
$\quad \text{Condition} \leftarrow \text{True}$

$\quad$**while** Condition **do**

$\qquad \text{IDs}_{\text{tmp}} \leftarrow \text{IDs where not Indeces}$
$\qquad \text{Redshifts}_{\text{tmp}} \leftarrow \text{Redshifts where not Indeces}$
$\qquad T_{\text{peak,tmp}} \leftarrow T_{\text{peak}} \text{ where not Indeces}$
$\qquad \text{Coords}_{\text{tmp}} \leftarrow \text{Coords where not Indeces}$

$\qquad t_i \leftarrow T_{\text{peak,tmp}}[i]$
$\qquad z_i \leftarrow \text{Redshifts}_{\text{tmp}}[i]$
$\qquad P_i \leftarrow \text{Coords}_{\text{tmp}}[i]$
$\qquad \text{ID}_i \leftarrow \text{IDs}_{\text{tmp}}[i]$

$\qquad \text{Matches} \leftarrow |T_{\text{peak}} - t_{\text{peak},i}| < \Delta t_{\text{peak, max}}$
$\qquad \text{Matches} \leftarrow \text{Matches and } |\text{Redshifts} - z_i| < \Delta z_{\text{max}}$
$\qquad \text{Matches} \leftarrow \text{Matches and sep}(\text{Coords}, P_i) < \Delta P_{\text{max}}$
$\qquad \text{Matches} \leftarrow \text{Matches or IDs} = \text{ID}_i$

$\qquad$**if** $\text{sum}(\text{Matches}) > 1$ **then**
$\qquad\qquad$ Append Matches to Indeces
$\qquad$**else**
$\qquad\qquad i \leftarrow i + 1$
$\qquad\qquad \text{Condition} \leftarrow \text{len}(\text{IDs}_{\text{tmp}}) = i$
$\qquad$**end if**

$\quad$**end while**

3.1.3 Cross-Matching Host Galaxy Properties

As outlined in Chapter 2, host mass is one of the most commonly used empirical indicators of a step in SNe Ia luminosity during calibration. The SuperCal and Pantheon+ compilations contain stellar mass estimates for the host galaxies of observed SNe. In this work, however, we aim to explore the impact of including multiple different host properties both independently and jointly, as outlined in Chapter 2. The package HOSTPHOT (Müller-Bravo *et al.*, 2022) could be used to compile arperture photometry for each SNe Ia host galaxy across different catalogs, after which SED fitting could be used to extract global and local properties such as stellar mass, U-V color and sSFR. Host morphology could be extracted using a package such as PYAUTOGALAXY (Nightingale *et al.*, n.d.). This is sadly out of scope for the project.

Instead we will rely on previous analyses by J18 and HyperLeda for host galaxy properties. In this case we once again need to cross-match catalogs, although the approach used can be simplified as we do not have to take duplicates into account as in the previous section. Further details on the datasets can be found in Section 3.4.

To cross-match morphologies we simply query the HyperLeda database for matches to the provided host galaxy coordinates, and cross-match between the resulting catalog and our chosen SNe compilation by position, redshift, and where applicable, SNe Ia ID. For the remaining host properties provided by J18, we again match SNe to their corresponding host galaxies' properties by position, redshift, and where applicable, SNe Ia ID.

A SNe Ia and a host galaxy observation is deemed to be a match if they fullfill the following criteria:

$$|z_{SN} - z_{HOST}| < \Delta z_{max}, \tag{3.5}$$

$$\text{sep}\,(P_{SN}, P_{HOST}) < \Delta P_{max}. \tag{3.6}$$

Here z is the CMB-frame redshift, P the sky-position (RA,DEC), sep(P_{SN},P_{HOST}) is the separation between SNe Ia and host positions in arc-seconds and Δz_{max}, ΔP_{max} are the corresponding cut-off values. For all sub-samples we set $\Delta z_{max} = 10^{-4}$ and $\Delta P_{max} = 1$ arc-second. If a SNe Ia ID match between the chosen compilation and J18/HyperLeda is found, then the SNe Ia and host observation are deemed a match iregardless of the previous constraints. This is however not always applicable due

to the different naming schemes across the component surveys of SuperCal and Pantheon+.

3.2 SuperCal

The SuperCal catalog is a compilation of the Pan-STARRS1 (PS1), Hubble Space Telescope (HST), Sloan Digital Sky Survey (SDSS), Carnegie Supernova Project (CSP) and CfA 1-4 SNe (Scolnic *et al.*, 2015). Each of these surveys are independently calibrated, at times using significantly different methods. Analyses of systematics at the time found that $> 70\%$ of the total systematic uncertainty was due to inhomogeneous photometric calibration (Scolnic *et al.*, 2015). The purpose of the SuperCal catalog was to introduce the SuperCal cross-calibration method whereby multiple independently calibrated surveys can be placed on a single, consistent photometric system. The methodology centers around the untargeted PS1 survey, which is used as the reference photometric system to cross-calibrate the remaining surveys. No quality cuts have been applied to SNe light curve observables.

3.2.1 Sub-Samples

For this work we will be making use of a single sub-sample of the SuperCal catalog, the Hubble flow sub-sample, as defined in W23. This sub-sample is limited to the redshift range $0.023 < z < 0.15$, known as the Hubble flow, where the effects of peculiar velocities are minor in comparison to the expansion of the Universe. The Hubble flow sub-sample is necessary to compare the impact of changes and improvements outlined in Chapter 2 to the model presentend in (Wojtak *et al.*, 2023). This sub-sample is also used in Section 4.3 to test for any tensions between the SuperCal and Pantheon+ Hubble flow sub-samples. An overview of sub-sample statistics can be seen in Table 3.1. The sub-sample of the SuperCal catalog has been created using the preprocessing pipeline outlined in Section 3.1 with $P_{fit,cut} = 0.001$.

As can be seen in Table 3.1, the no. of SNe Ia with multiple light curve observations is relatively low. As expected, the majority of SNe have observed host galaxy stellar masses, with at least 92% of SNe Ia having well-defined host masses. The remaining host properties lie in the range of $21.1 - 39.5\%$, with a higher fraction of SNe having well-defined host properties in the Hubble flow. This is due to host properties being observed mainly at lower redshifts, thus increasing the fraction of observations within the lower redshift range of the Hubble flow sub-sample. The most frequently observed property besides global host mass within the Hubble flow sub-sample is host morphology T.

	Full	Hubble Flow
Range	$0.0008 < z < 1.06$	$0.023 < z < 0.148$
N_{LC}	737	236
N_{SN}	713	219
$N_{SN}^{Duplicate}$	22	15
f_T	0.122	0.381
$f_{M_*}^{global}$	0.920	0.941
f_{sSFR}^{global}	0.106	0.250
f_{U-V}^{global}	0.111	0.267
$f_{M_*}^{local}$	0.128	0.288
f_{sSFR}^{local}	0.090	0.211
f_{U-V}^{local}	0.111	0.267

TABLE 3.1.
Summary statistics for sub-samples of the SuperCal catalog used in this work, describing the redshift range, no. of light curves, SNe, and fraction of host galaxy properties observed. All sub-samples have been created following Section 3.1, using $P_{fit,cut} = 0.001$.

3.3 Pantheon+

The Pantheon+ catalog is the state-of-the-art combination of type Ia SNe surveys, and underlies the to-date most stringent late-time constraints on cosmological parameters from type Ia SNe (Scolnic *et al.*, 2022). The main improvements over the SuperCal catalog are improved photometric calibration as outlined in (Brout *et al.*, 2022b) and an increased no. of SNe due to the inclusion of modern surveys. In comparison to SuperCal, light curve observables are derived using updated SALT models. The catalog is comprised of 18 different surveys, increasing the total no. of observed unique SNe Ia observations to 1550 within a redshift range of $0 < z < 2.3$, allowing for joint constraints of H_0 and other cosmological parameters such as w and Ω_m. See Table 1 in (Scolnic *et al.*, 2022) for further details on specific surveys included.

In comparison to the SuperCal catalog, published light curve parameters are only available for the cosmological sample outlined in (Scolnic *et al.*, 2022) and (Brout *et al.*, 2022a). This sub-sample, which we will refer to as the Pantheon+ catalog moving forward, is created using similar quality cuts to the ones outlined in Section 3.1. The specific cuts and corresponding no. of discarded light curves are shown in Table 2 in (Scolnic *et al.*, 2022). Compared to the cuts we use in our pre-processing

pipeline and those underlying the SuperCal catalog, the main differences are the following:

1. P_{fit}: The minimum fit probability $P_{fit,cut}$ is survey dependent and derived via simulations, in comparison to the constant value employed here and in W23. Values of 0.01, 0.001 and 0.001 are used for DES, PS1 and SDSS, respectively. No cuts are used for the remaining surveys.

2. U-band sensitivity: SNe above $z > 0.8$ exhibit a large distance moduli dependence on the inclusion of the U band, which S22 are not able to calibrate via cross-calibration.

3. $T_{rest} < 5$: S22 require that a given light curve has atleast one observation within 5 days of the estimated peak brightness in the SNe Ia rest frame. This requirement is not used in previous analysis, but aims to increase the quality of derived light curve observables.

4. Chauvernet's criterion: Although we use the same σ-limit of 3.5 as in (Brout *et al.*, 2022a), the choice of fiducial Tripp calibration parameters is not stated in either (Scolnic *et al.*, 2022) or (Brout *et al.*, 2022a). As such there can be a difference between discarded SNe in this work and in the cosmological sample.

5. Valid BiasCor: SNe Ia light curves are discarded if their light curve observables fall within sparsely populated regions of the simulations used in S22 and B22 to estimate bias corrections. Such corrections are not performed in SuperCal.

6. Systematics: Light curves discarded due to the requirement that they pass all other cuts in Table B1a for a series of different systematic perturbations outlined in B22. Such perturbations are not performed in SuperCal.

As seen in Table 2 in (Scolnic *et al.*, 2022), these additional cuts can at most amount to a difference 151 in the no. of observed light curves between the SuperCal and Pantheon+ catalogs. Additional differences can be caused by changes in light curve observables due to updated photometric calibration and SALT models, leading to exclusion during standard quality cuts.

3.3.1 Sub-Samples

As mentioned earlier, the Pantheon+ catalog is the main focus of this work. Compared to the SuperCal catalog, the Pantheon+ catalog's extended redshift range and

no. of observed SNe allow us to constrain both cosmological parameters and test the redshift dependence of W23's two-population model. To do this we make use of 4 sub-samples of Pantheon+. The first two are the full sample and the Hubble flow sub-sample, defined in the same way as for Section 3.2. Summary statistic for these sub-samples can be found in Table 3.2. The last two sub-samples are volume limited sub-samples of Pantheon+. These sub-samples are necessary to accurately probe a redshift dependence under the assumption that any sub-populations of type Ia SNe are linked to the progenitor model mentioned in Section 1.2.2. This is due to a potential difference in intrinsic SNe properties between populations, which in turn would lead to a selection effect in magnitude-limited surveys via the apparent magnitude's dependence as seen in Eq. 1.16. Similarly a redshift dependence in observables can also be qualitatively seen in Fig. 3.1, which shows stretch and color observables for untargeted surveys in Pantheon+ with varying redshift cuts. Although it is possible to account for this selection effect via simulations akin to S22, we instead opt for constructing volume-limited sub-samples. Such simulations would require extension of the SNANA simulation code to include a possible redshift dependence in the intrinsic SNe property distributions, which we deem out of scope for this project.
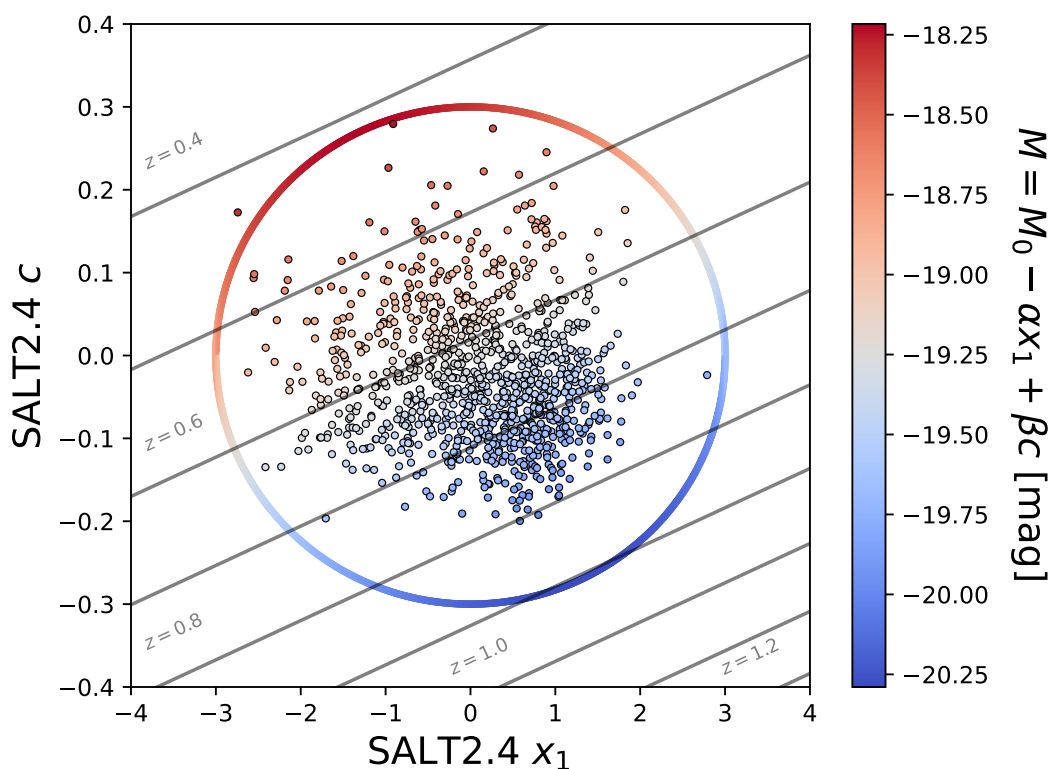
FIGURE 3.1.
SNe Ia apparent color versus stretch derived with SALT for untargeted surveys in Pantheon+. The color map shows the absolute magnitude given the color, stretch, and fiducial Tripp calibration parameter values. A bounding circle with $|c| < 0.3$ and $|x_1| < 3$, which bounds the majority of SNe Ia observed, shows the absolute magnitudes dependence on SNe Ia observables. Gray lines represent the corresponding cuts in the $c - x_1$ plane for a given z_{cut}

	Full	Hubble Flow	Fiducial	Conservative
Range	$0.0008 < z < 1.36$	$0.023 < z < 0.148$	$0.01 < z < 0.64$	$0.01 < z < 0.55$
N_{LC}	1274	398	741	420
N_{SN}	1199	358	740	420
$N_{SN}^{Duplicate}$	64	33	1	0
f_T	0.064	0.204	0.009	0.017
$f_{M_*}^{global}$	0.892	0.874	0.953	0.986
f_{sSFR}^{global}	0.095	0.221	0.042	0.074
f_{U-V}^{global}	0.097	0.226	0.043	0.076
$f_{M_*}^{local}$	0.137	0.302	0.069	0.121
f_{sSFR}^{local}	0.087	0.211	0.040	0.071
f_{U-V}^{local}	0.097	0.226	0.043	0.076

TABLE 3.2.
Summary statistics for sub-samples of the SuperCal catalog used in this work, describing the redshift range, no. of light curves, SNe, and fraction of host galaxy properties observed. All sub-samples have been created following Section 3.1, using $P_{fit,cut} = 0.001$.

We follow the methodology of (Nicolas *et al.*, 2021) to construct roughly volume-limited sub-samples of the Pantheon+ catalog. Assuming sufficient (and unbiased) spectroscopic follow-up for acquiring SNe Ia types and host galaxy redshifts, the observation selection effects of magnitude-limited surveys should be negligible below a given redshift at which even the faintest normal SNe Ia can be observed. Given such a survey can then be used to construct a volume-limited sub-sample using the relation

$$\mu(z_{cut}) = m_{i,limiting} - M_{B,max}$$

where $M_{B,max}$ is the maximum SNe Ia peak absolute magnitude in the B band and $m_{i,limiting}$ is the limiting magnitude / depth in the nearest band i to the rest frame B band in the redshift range of the survey. A value of $M_{B_{max}} = -18.0$ is assumed as in (Nicolas *et al.*, 2021).

The Pantheon+ catalog is a compilation of both targeted and untargeted surveys. Targeted surveys do not fulfill the unbiased criteria necessary for a volume-limited sub-sample, leaving only the untargeted surveys. The untargeted surveys present in Pantheon+ are SDSS, SNLS, PS1 and DES. Additionally we include the targeted Foundation survey, as it primarily is used as a follow up of low-redshift candidate SNe discovered by untargeted surveys. This results in 95% SNe in the Foundation survey having been discovered by untargeted surveys (Jones *et al.*, 2019).

Redshift ranges, filters covering the typical rest frame B band, corresponding limiting magnitudes and redshift cutoffs are shown in Table BLA. Redshift cutoffs are calculated assuming the fiducial cosmology defined in Section 1.1 assumed throughout this work. For all surveys except Foundation we report a fiducial and conservative cutoff redshift. The fiducial cutoff is derived from the deepest available limiting

magnitude of each survey, while the conservative cutoff is given by correspondingly conservative estimates.

The SDSS observed SNe Ia in the redshift range $0.05 < z < 0.35$. The corresponding filter for this range is the SDSS r filter, which has a 50% completeness limiting magnitude of 22.6 mag (Frieman *et al.*, 2008). This corresponds to a fiducial $z_{\text{cut}} = 0.27$, slightly higher than the value reported in (Nicolas *et al.*, 2021). During the first year of SDSS SNe Ia with $r < 20.5$ mag were favoured due to limited spectroscopic resources, corresponding to a redshift cutoff $z_{\text{cut}} = 0.15$. We adopt this as the conservative cutoff for SDSS.

The SNLS aquired SNe Ia in the redshift range $0.4 < z < 0.8$. Within this redshift range the rest-frame B band roughly corresponds to the SNLS i filter, which has a 5σ depth of 24.8 mag (*CFHTLS Final Release Executive Summary* n.d.). This corresponds to $z_{\text{lim}} = 0.64$, which we adopt as a fiducial cutoff. As in (Nicolas *et al.*, 2021), we use a conservative cutoff $z_{\text{lim}} = 0.55$.

PS1 observed SNe Ia in the range $0.02 < z < 0.6$, corresponding to the PS1 g filter. This filter has a 5σ limiting magnitude of 23.2 mag (Rest *et al.*, 2014; Chambers *et al.*, 2019), corresponding to a fiducial redshift cutoff $z_{\text{cut}} = 0.34$. Comparing with Fig. 6 of (Scolnic *et al.*, 2018), this cutoff redshift contains some bias due to selection effects. Based on this figure we adopt a conservative redshift cutoff $z_{\text{cut}} = 0.27$.

DES observed SNe Ia in a wider range from $0.1 < z < 0.8$, which roughly corresponds to the DES i-band filter. The DES-SN survey observed in eight "shallow" and two "deep" fields with corresponding 5σ limiting magnitudes of 23.5 and 24.5 mag, respectively. The observing fields of SNe Ia from the DES-SN survey are not reported in the Pantheon+ catalog. For the fiducial redshift cutoff we assume all SNe Ia are observed in the deep fields with a $z_{\text{cut}} = 0.57$. Correspondingly for the conservative redshift cutoff we assume all SNe Ia are observed in the shallow fields with a $z_{\text{cut}} = 0.39$.

Foundation is the only low-z survey to be included in the volume-limited sub-samples, and ranges from $0 < z < 0.1$. A limiting magnitude could not be readily found for the Foundation survey. Instead we assume a single redshift cutoff of $z_{\text{lim}} = 0.036$, corresponding to when the redshift distribution of the Foundation survey peaks.

The redshift distributions and number counts of SNe Ia observed by each survey can be seen in Fig. 3.2, along with the corresponding fiducial and conservative redshift cutoffs. Summary statistics for the fiducial and conservative sub-samples can be seen in Table 3.2.
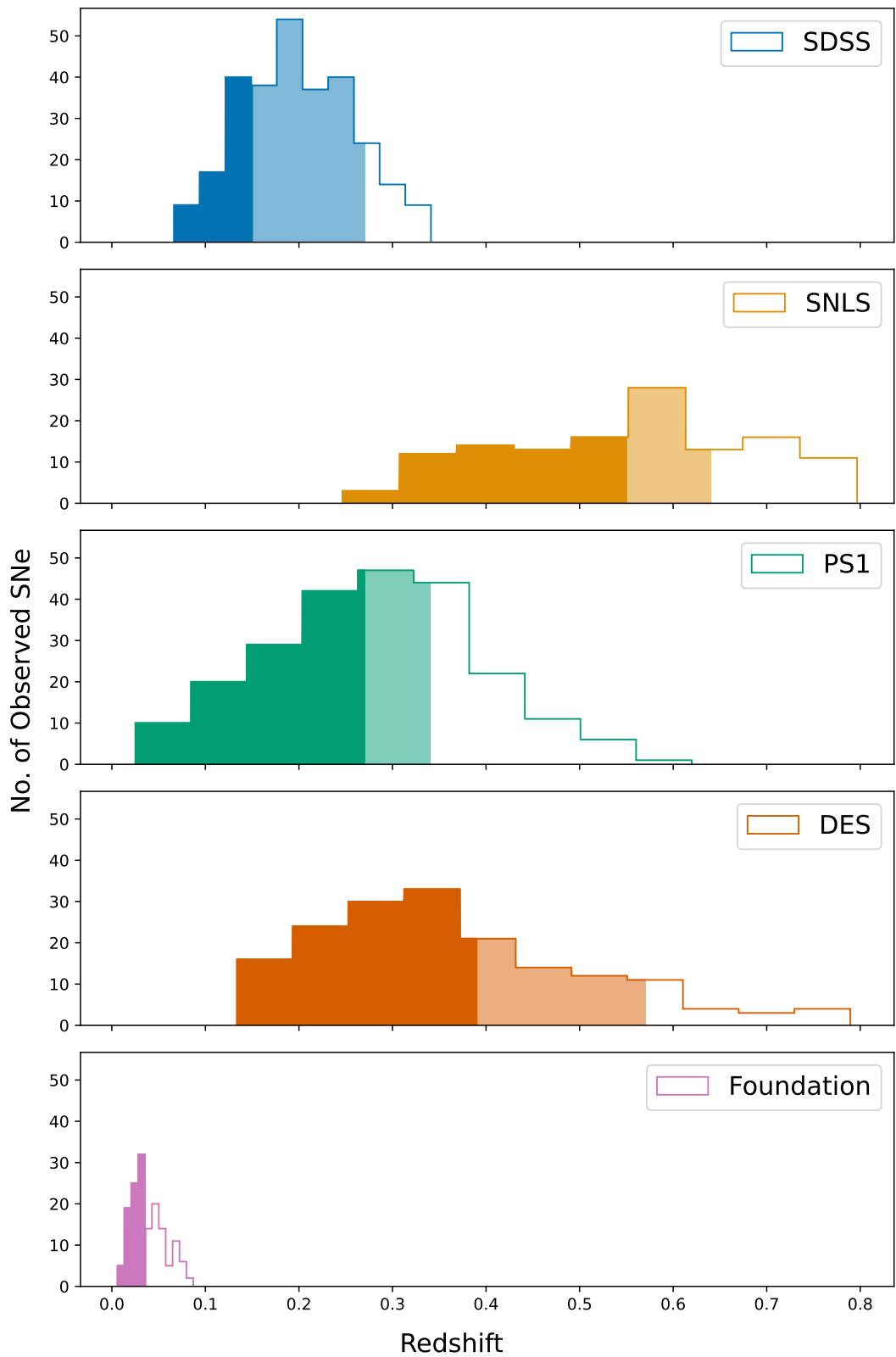
FIGURE 3.2.
Redshift distributions of untargeted surveys in Pantheon+. Colored regions correspond to SNe Ia included in the volume-limited sub-samples, with the fiducial and conservative sub-samples represented by the transparent and solid colored ranges, respectively.

As can be seen in Table 3.2, the no. of duplicates is higher than seen in Section 3.2, due to the inclusion of additional surveys. The no. of duplicates in the fiducial and conservative sub-samples is correspondingly low due to the lack of overlap between the untargeted surveys in Pantheon+. As expected, the majority of SNe have observed host galaxy stellar masses, with at least 87% of SNe Ia having well-defined host masses. The remaining host properties lie in the range of $1-30\%$, with a higher fraction of SNe having well-defined host properties in the Hubble flow. As in Section 3.2, this is due to host properties being observed mainly at lower redshifts, thus increasing the fraction of observations within the lower redshift range of the Hubble flow sub-sample. The most frequently observed property besides global host mass within the Hubble flow is local mass.

3.4 Host Galaxy Properties

As outlined in Section 1.2.1, empirical relations between SNe Ia and host galaxies have been used to decrease intrinsic scatter and improve SNe Ia standardization. The most prominent of these is the step in SNe Ia luminosity as a function of host galaxy mass. As such we want to explore the impact of host properties beyond host mass, using the methodology outlined in Chapter 2. Derivation of global and local host properties is out of scope for this project, as mentioned in Section 3.1.3, and we instead use to cross-matching with earlier works to construct a partial sample of measured host properties. Specifically we make use of the J18 catalog for global and local host properties and the HyperLeda database for host morphologies.

J18 is the resulting catalog of SNe Ia light curve observables and related global and local host properties from a study of the relation between type Ia SNe and host properties. The catalog contains 273 SNe Ia at $z < 0.1$, with host mass, sSFR and rest-frame U-V color measured globally and locally within a 1.5 kpc radius aperture around the related SN. The HyperLeda catalog provides host galaxy morphologies parameterised by the continuous variable T, which combines various indicators of galaxy morphology such as photometric structure, colour index and/or hydrogen content. The value of this metric can be mapped directly to the Hubble sequence with $T = -4$ for the earliest types (E) and $T = 10$ for the latest types such as irregular galaxies.

SNe Ia with observed host properties beyond global mass come from both targeted and untargeted surveys, as seen for the Pantheon+ Hubble Flow sub-sample in Table 3.3. This could introduce a bias in any observed intrinsic luminosity difference in the proposed two-population model. We choose to account for this in the same manner as J18; Split the Pantheon+ Hubble Flow sub-sample into two further sub-samples with and without host properties from targeted surveys, and by including bias cor-

rections as described in Section 1.4.2. The latter is only applicable when analyzing the Hubble Flow sub-sample, where we assume a redshift-independent weighting of the two sub-populations. As described in Section 1.4.2, this is due to bias corrections being produced under the assumption that intrinsic SNe Ia properties are redshift-independent. For a high-z analyses only the latter approach is applicable to account for any potential biases from targeted surveys.

	Full		Hubble Flow	
	Targeted	Untargeted	Targeted	Untargeted
M_*^{global}	211 (18.69%)	918 (81.31%)	132 (36.97%)	225 (63.03%)
$sSFR^{\text{global}}$	46 (46.46%)	53 (53.54%)	30 (38.96%)	47 (61.04%)
$U\text{-}G^{\text{global}}$	46 (45.1%)	56 (54.9%)	30 (37.97%)	49 (62.03%)
M_*^{local}	61 (42.07%)	84 (57.93%)	35 (33.02%)	71 (66.98%)
$sSFR^{\text{local}}$	39 (42.39%)	53 (57.61%)	26 (35.14%)	48 (64.86%)
$U\text{-}G^{\text{local}}$	46 (45.1%)	56 (54.9%)	30 (37.97%)	49 (62.03%)
T	7 (12.07%)	51 (87.93%)	51 (87.93%)	7 (12.07%)

TABLE 3.3.
Number (percentage) of observed host galaxy properties for SNe Ia from targeted and untargeted surveys for the Pantheon+ Full and Hubble flow sub-samples. The Fiducial and Conservative sub-samples are not shown, as they by definition only contain observations for SNe Ia from untargeted surveys.

As seen in Table 3.2, host properties besides global mass have relatively few observations compared to the total no. of SNe Ia in each sub-sample. The proposed methodology in Chapter 2 accounts for this by marginalizing out unobserved host properties. This can not account for the reduced constraining power that follows with low statistics, yet setting an arbitrary lower bound on the necessary no. of host property observations is unsatisfying. Instead we will in Section 5 make use of model comparison both via Bayes factors as well as the Bayesian model dimensionality as described in Section 1.3.3.

3.5   SN Ia Rates

The model extensions in Chapter 2 introduce a redshift dependent weighting between the proposed sub-populations of SNe Ia. This redshift dependence comes from the usage of models for volumetric SNe Ia rates as a function of redshift, which depends on the prompt fraction f_p and normalization η. Although the proposed model has the capability of constraining f_p, the normalization is removed when calculating weights as seen in Eq. 2.48. We include volumetric SNe Ia rate measurements to constrain η as well as explore potential increases in constraining power on f_p.

The data used is equivalent to that in (Wojtak *et al.*, 2019), which is a compilation of observational determinations of the volumetric type Ia SN rates from (Rodney *et al.*, 2014) and updated with results from the CANDELS survey. These observational measurements span the redshift range $0 < z < 2.5$, and were shown earlier in Fig. 1.5 together with the volumetric rate prediction from Eq. 2.62.

Observational measurements of the volumetric SNe Ia rate are derived mainly from untargeted surveys, which means there is significant overlap between the observations underlying the Pantheon+ catalog and the volumetric rate compilation used. In this work we assume the two to be independent, but more work needs to be done to account for covariance between the two datasets.

Reproducing Results

<div style="text-align: right">4</div>

BAYESNOVA can be seen as a framework to modularize and extend the model presented in Wojtak *et al.*, 2023. It is important to quantify the impact of each extension as well as the baseline model defined in Chapter 2 in comparison to Wojtak *et al.*, 2023 to ensure proper implementation. This is done by running each extension of the model on the SuperCal Hubble flow sub-sample defined in Section 3.2, and is the focus of Section 4.1. As mentioned earlier, however, is the Pantheon+ catalog. Since this catalog can be seen as a modern succesor of SuperCal, one would expect results between the two to be in agreement. This is explored in Section **??**, were we find a potential discrepancy between SuperCal and Pantheon+ similar to that found between SuperCal and Foundation in Wojtak *et al.*, 2023. We therefore in Section 4.3 use techniques outlined in Section 1.3.3 to quantify the tension between the SuperCal and Pantheon+ catalogs.

4.1 SuperCal

In this section we compare the impact of the model extensions in BAYESNOVA to the results in Wojtak *et al.*, 2023. The model results are calculated using the default prior and sampler settings described in Section **??**. The models that we compare with BAYESNOVA are:

- *Base*: BAYESNOVA implementation of the baseline model defined in Wojtak *et al.*, 2023, fit to the SuperCal Hubble flow dataset without reduction or removal of duplicate SNe Ia.

- *Base+Duplicates*: *Base*-model with duplicate SNe Ia observations reduced according to the methodology outline in Section 2.1.

- *Base+Duplicates+Variable*: *Base+Duplicates*-model with variable $E(B-V)$ prior integration limits, as described in Section **??**.

- *Base+Duplicates+Truncated*: *Base+Duplicates*-model with a truncated Gaussian R_B prior, as described in Section **??**.

As can be seen in Table 4.1, leaving duplicates untreated in the dataset has a large impact on the parameters that are recovered. The presence of duplicate observa-

model	Wojtak *et al.*, 2023		Base		Base+Duplicates		Base+Duplicates+Variable		Base+Duplicates+Truncated		Baseline	
	SNe Pop 1	SNe Pop 2	SNe Pop 1	SNe Pop 2	SNe Pop 1	SNe Pop 2	SNe Pop 1	SNe Pop 2	SNe Pop 1	SNe Pop 2	SNe Pop 1	SNe Pop 2
$\hat{M}_B$	$-19.49^{+0.05}_{-0.05}$	$-19.40^{+0.07}_{-0.07}$	$-19.37^{+0.06}_{-0.07}$	$-19.32^{+0.07}_{-0.2}$	$-19.41^{+0.07}_{-0.05}$	$-19.29^{+0.05}_{-0.07}$	$-19.41^{+0.08}_{-0.06}$	$-19.28^{+0.05}_{-0.06}$	$-19.49^{+0.04}_{-0.06}$	$-19.36^{+0.04}_{-0.08}$	$-19.54^{+0.07}_{-0.24}$	$-19.43^{+0.09}_{-0.23}$
$\hat{X}_1$	$-1.3^{+0.3}_{-0.2}$	$0.4^{+0.1}_{-0.1}$	$-0.9^{+0.4}_{-0.6}$	$0.5^{+0.2}_{-0.1}$	$-1.2^{+0.5}_{-0.3}$	$0.5^{+0.2}_{-0.1}$	$-1.4^{+0.2}_{-0.2}$	$0.4^{+0.1}_{-0.1}$	$-1.3^{+0.3}_{-0.2}$	$0.4^{+0.1}_{-0.1}$	$-1.4^{+0.3}_{-0.3}$	$0.4^{+0.1}_{-0.3}$
σ_{X_1}	$0.7^{+0.2}_{-0.1}$	$0.65^{+0.09}_{-0.09}$	$1.^{+0.2}_{-0.3}$	$0.6^{+0.1}_{-0.1}$	$0.8^{+0.2}_{-0.2}$	$0.61^{+0.09}_{-0.13}$	$0.7^{+0.1}_{-0.1}$	$0.66^{+0.10}_{-0.07}$	$0.7^{+0.2}_{-0.1}$	$0.64^{+0.10}_{-0.07}$	$0.7^{+0.2}_{-0.2}$	$0.68^{+0.19}_{-0.09}$
$\hat{c}_{int}$	$-0.04^{+0.04}_{-0.03}$	$-0.11^{+0.03}_{-0.04}$	$-0.06^{+0.02}_{-0.03}$	$-0.11^{+0.04}_{-0.03}$	$-0.05^{+0.03}_{-0.04}$	$-0.10^{+0.03}_{-0.04}$	$-0.06^{+0.03}_{-0.07}$	$-0.11^{+0.03}_{-0.05}$	$-0.02^{+0.02}_{-0.04}$	$-0.06^{+0.02}_{-0.04}$	$-0.04^{+0.04}_{-0.14}$	$-0.09^{+0.04}_{-0.10}$
$\sigma_{c_{int}}$	$0.08^{+0.01}_{-0.01}$	$0.043^{+0.008}_{-0.009}$	$0.06^{+0.02}_{-0.03}$	$0.04^{+0.02}_{-0.02}$	$0.08^{+0.01}_{-0.02}$	$0.04^{+0.01}_{-0.02}$	$0.07^{+0.02}_{-0.03}$	$0.04^{+0.01}_{-0.02}$	$0.09^{+0.01}_{-0.01}$	$0.059^{+0.009}_{-0.012}$	$0.08^{+0.02}_{-0.04}$	$0.06^{+0.01}_{-0.02}$
τ	$0.017^{+0.008}_{-0.010}$	$0.034^{+0.008}_{-0.009}$	$0.04^{+0.02}_{-0.01}$	$0.04^{+0.02}_{-0.01}$	$0.032^{+0.011}_{-0.009}$	$0.04^{+0.01}_{-0.01}$	$0.03^{+0.01}_{-0.01}$	$0.04^{+0.01}_{-0.01}$	$0.024^{+0.011}_{-0.008}$	$0.028^{+0.009}_{-0.008}$	$0.03^{+0.01}_{-0.01}$	$0.025^{+0.009}_{-0.008}$
α	$-0.19^{+0.03}_{-0.03}$		$-0.16^{+0.04}_{-0.03}$		$-0.19^{+0.03}_{-0.02}$		$-0.19^{+0.03}_{-0.02}$		$-0.20^{+0.03}_{-0.02}$		$-0.18^{+0.04}_{-0.03}$	
β	$3.1^{+0.3}_{-0.2}$		$3.0^{+0.3}_{-1.0}$		$3.1^{+0.3}_{-0.2}$		$3.2^{+0.3}_{-0.3}$		$2.9^{+0.2}_{-0.3}$		$2.7^{+0.3}_{-1.0}$	
$\hat{R}_B$	$4.1^{+0.6}_{-0.2}$		$3.9^{+0.6}_{-0.4}$		$4.1^{+0.0}_{-0.5}$		$3.9^{+0.5}_{-0.4}$		$6.0^{+1.3}_{-1.0}$		$5.0^{+2.0}_{-1.0}$	
σ_{R_B}	$1.0^{+0.3}_{-0.3}$		$1.0^{+0.4}_{-0.2}$		$1.0^{+0.5}_{-0.2}$		$1.0^{+0.4}_{-0.2}$		$0.5^{+0.2}_{-0.1}$		$0.5^{+0.2}_{-0.2}$	
γ	$3.0^{+1.0}_{-1.0}$		$2.0^{+1.2}_{-0.7}$		$2.1^{+1.1}_{-0.7}$		$2.4^{+2.2}_{-0.9}$		$1.9^{+1.3}_{-0.6}$		$3.0^{+4.}_{-2.0}$	
f_1^{SN}	$0.38^{+0.10}_{-0.09}$		$0.6^{+0.2}_{-0.2}$		$0.5^{+0.2}_{-0.1}$		$0.35^{+0.07}_{-0.09}$		$0.39^{+0.09}_{-0.08}$		$0.34^{+0.09}_{-0.13}$	
$\Delta\mathcal{Z}$	-		0.0		$-28.7^{+0.2}_{-0.2}$		$28.6^{+0.2}_{-0.2}$		$8165.5^{+0.2}_{-0.2}$		$8161.8^{+0.2}_{-0.2}$	
$\tilde{d}$	-		$27.0^{+1.0}_{-1.0}$		$31.0^{+2.0}_{-1.0}$		$28.6^{+0.2}_{-0.2}$		$25.1^{+0.8}_{-0.7}$		$25.8^{+0.5}_{-0.5}$	

TABLE 4.1.
Comparison between baseline results in Wojtak *et al.*, 2023 and model extensions introduced in Section 2. Parameter values are posterior medians, with errors given by the 16th and 86th percentiles. Bayes' factors $\Delta\mathcal{Z}$ are calculated wrt. the BAYESNOVA baseline model and are shown together with model BMDs $\tilde{d}$ for model comparison's sake.

tions drives the model towards specific regions of parameter space due to over-representation of certain SNe Ia, leading especially to worse constraints on f_1^{SN} and a low γ value. Due to this, the remaining models are evaluated with duplicates reduced.

Including duplicates, we see general agreement within 1σ between Wojtak *et al.*, 2023 and BAYESNOVA, except for the γ and f_1^{SN} parameters. This result can be attributed to the inclusion of SNe Ia that were not present in Wojtak *et al.*, 2023, due to some duplicates being filtered out.

Using a variable integration limit alleviates this minor tension however, increasing γ and decreasing f_1^{SN}. Including a truncated prior on R_B has a similar affect, albeit with $\hat{R}_B$ increasing to $\hat{R}_B = 6.0$, which in turn impacts color related parameters β, c_{int}, τ and γ. Although $\hat{R}_B$ is increased, constraints are correspondingly decreased. It is not currently clear why inclusion of the truncated R_B prior has this impact.
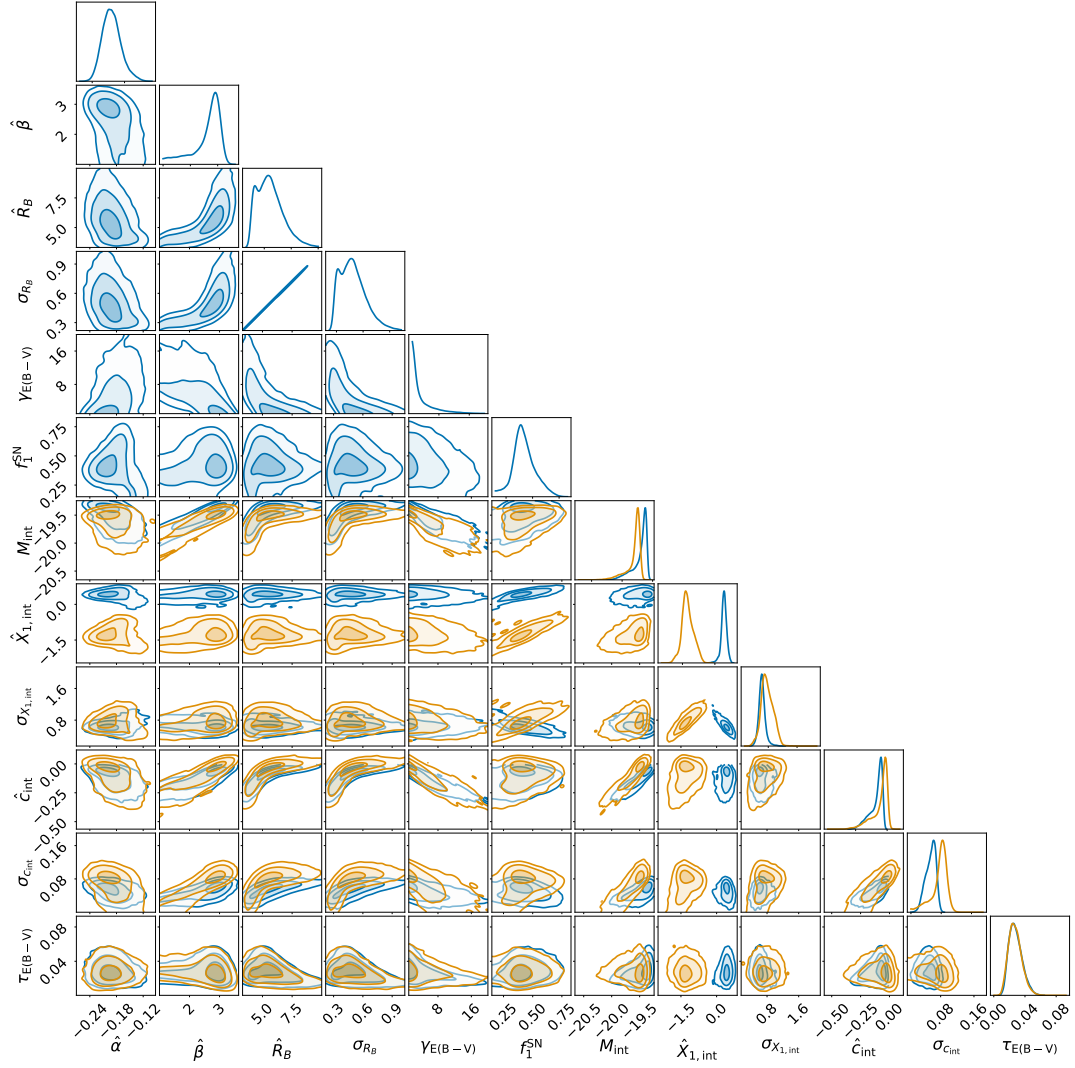
FIGURE 4.1.
Posterior distribution of baseline model fit to the SuperCal Hubble flow. Independent parameters are over-plotted in orange and blue for Population 1 and Population 2, respectively.

Finally we have the baseline model, combining all model extensions mentioned so far. We here find overall agreeance with Wojtak *et al.*, 2023, with increased errors on $\hat{R}_B$, β, γ and c_{int}, which can also be seen in Fig. 4.1. This is due to the impact of the truncated R_B prior. Regarding population-level parameters, the largest difference between this work's model and Wojtak *et al.*, 2023 is in the $\hat{c}_{int}$ and τ parameters, which are less distinct from each other compared to Wojtak *et al.*, 2023. This is perhaps not too surprising considering the higher value and errors of $\hat{R}_B$ and its relationship to the remaining parameters via Eq. 1.18

Due to the difference in data used (reduction vs. no reduction of duplicates), we only calculate Bayes' factors between BAYESNOVA models using reduced duplicate SNe Ia. Comparing Bayes' factors, we see that the baseline and truncated-prior models are strongly preferred by the data. The large difference is attributed to the truncated

prior normalization introduced in Eq. **??**. Comparing model dimensionalities, we see that the data generally supports $\tilde{d} \sim 25$ parameters for all variations of model priors. Although we can not clearly claim that the baseline model is preferable compared to the truncated-prior model based on these metrics, we chose to maintain usage of the baseline model due to arguments of physicality given in Section 2.

4.2   Pantheon+

Having shown that we can generally recover the results of Wojtak *et al.*, 2023 using BAYESNOVA, we move on to the main focus of this work, the Pantheon+ catalog. We fit the BAYESNOVA baseline model to the Pantheon+ Hubble flow sample described in Section 3.3 and compare with the results from fitting the SuperCal catalog. These results can be seen in Table 4.2 and in Fig. 4.2.

Model	Wojtak *et al.*, 2023		Baseline		Baseline	
Sub-sample	SuperCal Hubble Flow		SuperCal Hubble Flow		Pantheon+ Hubble Flow	
	SNe Pop 1	SNe Pop 2	SNe Pop 1	SNe Pop 2	SNe Pop 1	SNe Pop 2
$\hat{M}_B$	$-19.49^{+0.05}_{-0.05}$	$-19.40^{+0.07}_{-0.07}$	$-19.54^{+0.07}_{-0.24}$	$-19.43^{+0.09}_{-0.23}$	$-19.62^{+0.06}_{-0.07}$	$-19.53^{+0.07}_{-0.06}$
$\hat{X}_1$	$-1.3^{+0.3}_{-0.2}$	$0.4^{+0.1}_{-0.1}$	$-1.4^{+0.3}_{-0.3}$	$0.4^{+0.1}_{-0.3}$	$-1.1^{+0.2}_{-0.1}$	$0.49^{+0.08}_{-0.07}$
σ_{X_1}	$0.7^{+0.2}_{-0.1}$	$0.65^{+0.09}_{-0.09}$	$0.7^{+0.2}_{-0.2}$	$0.68^{+0.19}_{-0.09}$	$0.67^{+0.09}_{-0.07}$	$0.058^{+0.05}_{-0.05}$
$\hat{c}_{\text{int}}$	$-0.04^{+0.04}_{-0.03}$	$-0.11^{+0.03}_{-0.04}$	$-0.04^{+0.04}_{-0.14}$	$-0.09^{+0.04}_{-0.10}$	$-0.13^{+0.02}_{-0.03}$	$-0.16^{+0.02}_{-0.02}$
$\sigma_{c_{\text{int}}}$	$0.08^{+0.01}_{-0.01}$	$0.043^{+0.008}_{-0.009}$	$0.08^{+0.02}_{-0.04}$	$0.06^{+0.01}_{-0.02}$	$0.034^{+0.01}_{-0.01}$	$0.030^{+0.006}_{-0.005}$
τ	$0.017^{+0.008}_{-0.010}$	$0.034^{+0.008}_{-0.009}$	$0.03^{+0.01}_{-0.01}$	$0.025^{+0.009}_{-0.008}$	$0.039^{+0.007}_{-0.006}$	$0.038^{+0.007}_{-0.006}$
α	$-0.19^{+0.03}_{-0.03}$		$-0.18^{+0.04}_{-0.03}$		$-0.18^{+0.02}_{-0.01}$	
β	$3.1^{+0.3}_{-0.2}$		$2.7^{+0.3}_{-1.0}$		$1.3^{+0.4}_{-0.2}$	
$\hat{R}_B$	$4.1^{+0.6}_{-0.2}$		$5.0^{+2.0}_{-1.0}$		$3.8^{+0.2}_{-0.1}$	
σ_{R_B}	$1.0^{+0.3}_{-0.3}$		$0.5^{+0.2}_{-0.2}$		$0.27^{+0.02}_{-0.02}$	
γ	$3.0^{+1.0}_{-1.0}$		$3.0^{+4.}_{-2.0}$		$3.5^{+1.3}_{-0.8}$	
f_1^{SN}	$0.38^{+0.10}_{-0.09}$		$0.34^{+0.09}_{-0.13}$		$0.37^{+0.06}_{-0.05}$	
$\tilde{d}$	-		$25.8^{+0.5}_{-0.5}$		$21.0^{+1.1}_{-0.9}$	

TABLE 4.2.
Comparison between baseline results in Wojtak *et al.*, 2023 and model extensions introduced in Section 2. Parameter values are posterior medians, with errors given by the 16th and 86th percentiles. Bayes' factors $\Delta\mathcal{Z}$ are calculated wrt. the BAYESNOVA baseline model and are shown together with model BMDs $\tilde{d}$ for model comparison's sake.

Starting with similarities, we find similar trends across all parameters between SuperCal and Pantheon: Pop. 1 is intrinsically brighter than pop. 2, pop. 1 has lower stretch than pop. 2 and pop. 1 is intrinsically redder than pop. 2. For the shared parameters we find similar values for $\hat{\alpha}$, $\hat{R}_B$, and γ. Differences are, however, also

present, with the most prominent being the reduction in β. We see in Fig. 4.2 that this parameter is upper-bounded, tending towards $\hat{\beta} \sim 0$. Differences can also be found in other color-related parameters, with intrinsic colors being significantly bluer in Pantheon+ compared to SuperCal. We also find no difference in dust distribution, with $\tau_1 \approx \tau_2$. At the same time we find tighter constraints on the majority of these parameters, as one would expect due to the increased number of observed SNe Ia.
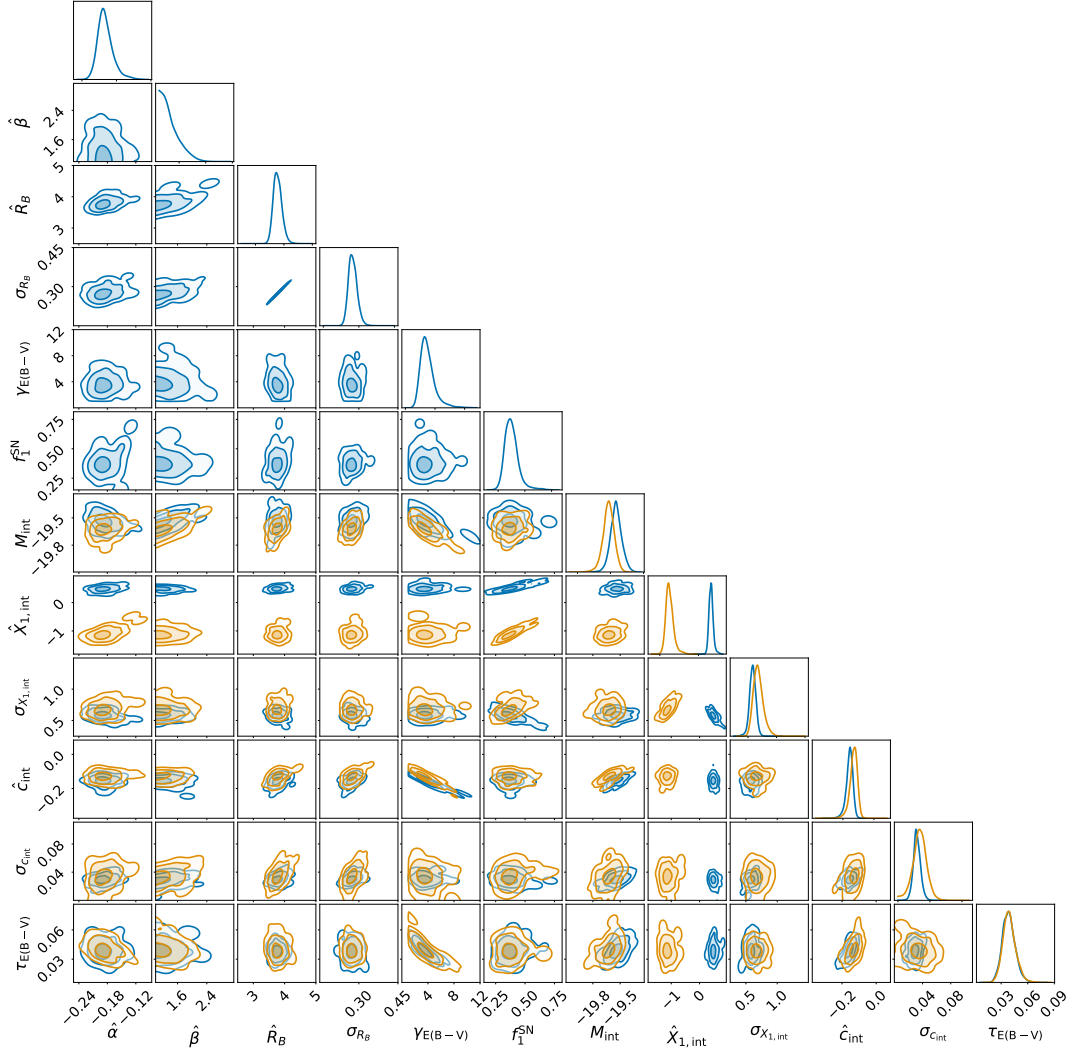
FIGURE 4.2.
Posterior distribution of baseline model fit to the Pantheon Hubble flow. Independent parameters are over-plotted in orange and blue for Population 1 and Population 2, respectively.

This result is somewhat similar to that found by Wojtak *et al.*, 2023 when comparing SuperCal with the Foundation survey, one of the surveys which make up Pantheon+. When performing this comparison, Wojtak *et al.*, 2023 find that $\hat{\beta}$ is unconstrained, and use a tighter prior based on results from SuperCal to ensure convergence. They argue that this is due to larger errors on the observed apparent colors c_{app} in combination with Foundation survey preferring tighter intrinsic color distributions. In our case we find that $\hat{\beta}$ is upper-bounded, trending towards the lower-bound $\hat{\beta} = 1$ of

the chosen prior. We also find that Pantheon+ tends towards tighter intrinsic color distributions.

4.3   SuperCal vs. Pantheon+

In the previous section we found differing results when fitting the baseline model to the SuperCal and Pantheon+ Hubble flow sub-samples. As outlined in Section 3.3, the Pantheon+ catalog is a modern sucessor of SuperCal, containing new SNe Ia observations and featuring an updated preprocessing pipeline. Due to this, the comparison in the previous section is not a 1-to-1 comparison and we must quantify if this difference is simply due to increased statistics or systematics introduced by new SNe Ia, new preprocessing methods or a combination thereof. In Fig. 4.1 we compare SNe Ia observables for SNe present in both the SuperCal and Pantheon+ Hubble flow sub-samples.
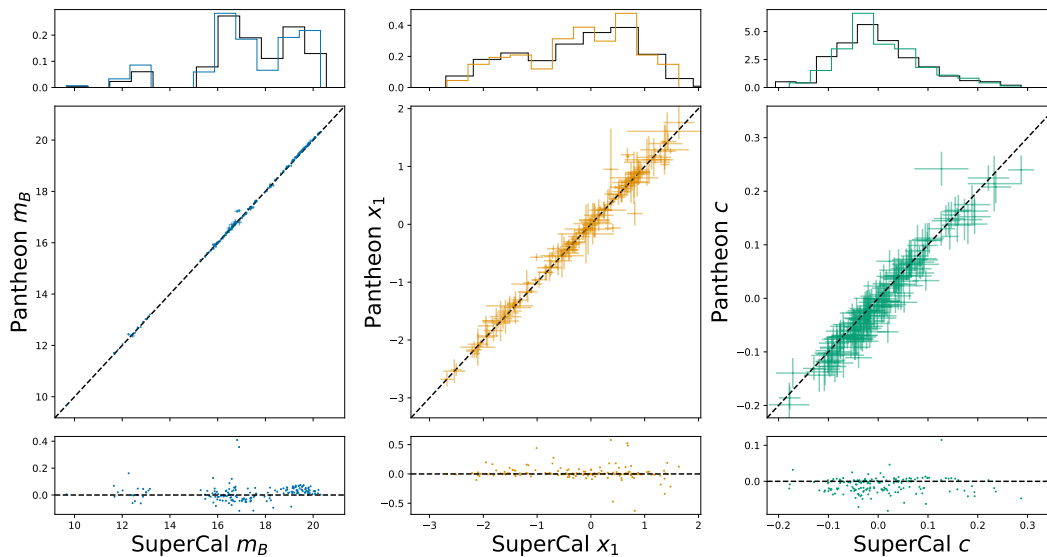
FIGURE 4.3.
Comparison of SNe Ia light curve observables for SNe Ia cross-matched between the SuperCal and Pantheon+ Hubble flow sub-samples.

We see that qualitatively there is good agreement between the SNe Ia common to both catalogs, with the largest deviations being seen in the apparent color. This is perhaps to be expected, since one of the major preprocessing changes between SuperCal and Pantheon+ are changes made to the photometric cross-calibration. We choose to make use of the suspicion metric outlined in Section 1.3.3 to quantify the degree of difference, or tension, between SuperCal and Pantheon. The hypotheses we want to compare are

- H_0: The SuperCal and Pantheon+ Hubble flow sub-samples can be described by the same posterior distributions,

- H_1: The SuperCal and Pantheon+ Hubble flow sub-samples can not be described by the same posterior distributions due to

  - H_1^A: changes made to the preprocessing pipeline,

  - H_1^B: and/or the exclusion of SNe Ia from Supercal and inclusion of new SNe Ia in Pantheon+.

We can test the null hypothesis H_0 versus the alternative H_1 using the suspicion metric. In this case we need to fit the baseline model to SuperCal and Pantheon+ independently, as well as to the union of the two datasets, after which the suspicion can be calculated according to Eq. 1.44. The two sub-hypotheses, H_1^A and H_1^B become relevant if significant tension is found between SuperCal and Pantheon. These alternative hypotheses allow us to determine any observed tension is due the updated preprocessing pipeline, the inclusion / exclusion of SNe Ia observations, or a combination of the two.

For H_1^A we define the sub-samples D_A^1 and D_A^2, where D_A^1 consists of observations in SuperCal for SNe Ia present in Pantheon+ and D_A^2 consists of observations in Pantheon+ for SNe Ia present in SuperCal. That is, D_A^1 and D_A^2 are the set of SNe Ia observations corresponding to cross-matched SNe Ia between the two catalogs. If the tension is at the same level as when comparing SuperCal and Pantheon+ directly then one would conclude that changes to the photometric calibration is at fault. If instead we find reduced or no evidence for tension between D_A^1 and D_A^2 would indicate that changes to the photometric calibration has not had a large impact on inference. In that case, we continue onwards to sub-hypothesis H_1^B.

For H_1^B we define the sub-samples D_B^1 and D_B^2, where D_B^1 is the SuperCal Hubble flow sub-sample and $D_B^2 = D_A^2 + S\,P$ is the set of Pantheon+ observations of SNe Ia that occur in SuperCal combined with the set of SNe Ia that occur in SuperCal but not in Pantheon+. In this sense we extend the cross-match between SuperCal and Pantheon+ to include SNe Ia that have been excluded by the Pantheon+ preprocessing pipeline. Reduced or no evidence for tension would in this case imply that the exclusion of SuperCal SNe Ia observations is the cause of the tension. If we instead find that tension persists, then this would imply that new, duplicate observations are at fault.

Applying the suspicion metric to compare H_0 and H_1, we find suspicion $\log S = 152.6 \pm 0.3$ and $d = 16.4^{+1.1}_{-0.9}$. The tension probability introduced in Section 1.3.3 is calculated using the χ^2-distributed variable $d - 2 \log S$, which was derived assuming a Gaussian likelihood, uniform priors and uncorrelated data. We break with all of these assumptions, which most likely is the cause of $d - 2 \log S < 0.$, which excludes the usage of a χ^2-test to calculate the tension probability. The suspiciously high concordance implied by the large value of $\log S$ is most likely due to the high correlation between the SuperCal and Pantheon+ samples, which we did not take into account due to current model limitations in BAYESNOVA. As such, we must conclude that the suspicion metric breaks down in the current use-case, and can *not* be used to determine the potential tension between the observed SuperCal and Pantheon+ results. We leave a repeat of this analysis, using the full covariance between datasets being compared, as future work.

Host Galaxy Properties

5

Although referred to throughout this thesis and implemented in BAYESNOVA, technical issues has prevented the inclusion of host-property related results. I hope to be able to present these results at the defence of this thesis, as well as include in an updated document in the future. As such, we defer inclusion and study of host properties according to Chapter 2 to future work.

SNe Ia Progenitor Constraints

<div style="text-align: right; font-size: 3em;">6</div>

A potential explanation for the two sub-populations of SNe Ia found using BAYESNOVA is due to the existence of atleast two distinct progenitor channels. Such distinct progenitor channels have been proposed by theoretical physicists, in the form of prompt and delayed progenitors, as outlined in Section 1.2.3. Although no direct detections of SNe Ia progenitors have been made, indirect constraints have been placed on these progenitors via the DTD. These constraints come mainly from measurements of volumetric- as well as individual galaxy SNe Ia rates. The well-known bimodality in SNe Ia stretch is thought to be linked to the underlying progenitors (Liu *et al.*, 2023), but no statistical models currently exist to model the joint DTD and stretch distribution. We have in Section 2.4 introduced an extension to the two-population model from Wojtak *et al.*, 2023 that allows for the SNe Ia population fraction f_1^{SN} to be redshift-dependent via Eq. 2.48. This redshift-dependence comes from the DTD-derived volumetric SNe Ia rate, whereby we link the two model sub-populations directly to the DTD. In this way we aim to jointly constrain the underlying sub-populations in SNe Ia light-curve observables as well as SNe Ia progenitors via the DTD.

6.1   SNe Ia Constraints

We first fit the baseline and redshift-dependent models to the fiducial Pantheon+ sub-sample introduced in Section 3.3.1. This sub-sample is constructed such that it is roughly volume-limited, so that we avoid the impact of selection effects on inference. As described in Section 2.4, the redshift-dependent SNe Ia model is only sensitive to the fraction of prompt SNe Ia f_{prompt} and insensitive to the DTD normalization η. We therefore fix $\eta = 1.02^{+0.27}_{-0.15} \times 10^{-4} h_{70}^2 \text{ yr}^{-1} \text{ M}_\odot^{-1}$ from (Wojtak *et al.*, 2019), while allowing f_{prompt} to be free.

We present the results of these model fits in the first two columns of Table **??**. We see that the redshift-dependent model is strongly supported by the data according to the Jeffrey's scale when compared with the baseline model, with $\Delta \log \mathcal{Z} = 52.88^{+0.08}_{-0.10}$. Comparing SNe Ia population parameter values, we see that the redshift-dependent

value has a less significant bimodality in SNe Ia stretch, with the mean population 1 stretch parameter being larger by roughly a factor two between the baseline and redshift-dependent models. Other than that, parameters are within 1σ between the two models. This difference in stretch may imply that the DTD-based population fraction is not expressive enough to fully capture the underlying stretch evolution in redshift. Alternatively it could imply that perhaps only part of the redshift dependence / bimodality is due to the presence of two distinct progenitor channels. This mismatch between observations and predictions is also clear in the left side of Fig. 6.1, where we compare the mean model stretch vs observed mean stretch as a function of redshift, with the fiducial sub-sample shown in blue. The mean stretch predicted by the model is given by

$$\langle \hat{X}_1 \rangle(z) = f_1^{SN}(z)\hat{X}_1 + (1 - f_1(z)^{SN})\hat{X}_2. \tag{6.1}$$

We see the largest deviation between observations and model predictions at low redshifts, which is to expected considering the the higher posterior value for $\hat{X}_1$ found when using the redshift-dependent model.

The posterior value of the prompt fraction $f_{\text{prompt}} = 0.67^{+0.05}_{-0.05}$ is consistent with measurements made in the past, such as by Rodney *et al.*, 2014 who find $f_{\text{prompt}} = 0.53^{+0.14}_{-0.36}$ and Wojtak *et al.*, 2019 who find $f_{\text{prompt}} = 0.63^{+0.07}_{-0.11}$. Our model increases constraining power on f_{prompt} by roughly a factor of 2, highlighting the benefit of using SNe Ia light curves directly to constrain SNe Ia progenitors.

Having shown that the redshift-dependent model is strongly supported by the data, we move on to the remaining high-z sub-samples. In the last two columns of Table 6.1 we present the resulting parameter constraints when fitting the redshift-dependent model to the conservative and full Pantheon+ sub-samples. Not unexpectedly we find essentially the same posterior parameters for the fiducial and conservative sub-samples. The largest difference is in the stretch parameters, were find $\Delta \hat{X}_1 = \hat{X}_1^{con} - \hat{X}_1^{fid} \approx -0.1$ and $\hat{X}_2 = \hat{X}_2^{con} - \hat{X}_2^{fid} \approx 0.1$, showing that the stretch parameters shift further apart. This difference is not significant considering the size of the errors, but may indicate that the fiducial sample is not fully volume limited. For the full Pantheon+ sub-sample we find a 3σ difference in $\hat{X}_1$, with $\hat{X}_1^{full} = -0.71 \pm 0.09$. Intrinsic colors are shifted towards redder values, and we find a large difference in the dust reddening shape parameter γ, with $\gamma^{full} = 2.7$ compared with $\gamma > 3$ for the remaining 3 models. This observed difference between the full and volume-limited sub-samples confirms that selection effects must be included if the full redshift-range is to be used. For completeness sake, we show the posterior population 1 fraction and mean stretch evolution for the conservative and full sub-samples in Fig. 6.1. We see that although the conservative and full sub-samples lead to lower mean stretch

Model	Baseline		Redshift-Dependent		Redshift-Dependent		Redshift-Dependent	
Sub-sample	Pantheon+ Fiducial		Pantheon+ Fiducial		Pantheon+ Conservative		Pantheon+ Full	
	SNe Pop 1	SNe Pop 2	SNe Pop 1	SNe Pop 2	SNe Pop 1	SNe Pop 2	SNe Pop 2	SNe Pop 2
$\hat{M}_B$	$-19.63^{+0.04}_{-0.04}$	$-19.56^{+0.05}_{-0.06}$	$-19.64^{+0.04}_{-0.04}$	$-19.56^{+0.05}_{-0.06}$	$-19.61^{+0.04}_{-0.05}$	$-19.56^{+0.06}_{-0.07}$	$-19.63^{+0.03}_{-0.03}$	$-19.52^{+0.03}_{-0.03}$
$\hat{X}_1$	$-0.45^{+0.09}_{-0.10}$	$0.61^{+0.05}_{-0.06}$	$-0.49^{+0.10}_{-0.10}$	$0.58^{+0.06}_{-0.06}$	$-0.6^{+0.1}_{-0.1}$	$0.65^{+0.06}_{-0.06}$	$-0.71^{+0.09}_{-0.09}$	$0.58^{+0.04}_{-0.04}$
σ_{X_1}	$0.80^{+0.05}_{-0.05}$	$0.47^{+0.04}_{-0.04}$	$0.80^{+0.05}_{-0.05}$	$0.48^{+0.04}_{-0.04}$	$0.79^{+0.06}_{-0.06}$	$0.45^{+0.05}_{-0.04}$	$0.83^{+0.05}_{-0.05}$	$0.48^{+0.03}_{-0.03}$
$\hat{c}_{\text{int}}$	$-0.13^{+0.01}_{-0.02}$	$-0.16^{+0.02}_{-0.02}$	$-0.13^{+0.01}_{-0.02}$	$-0.16^{+0.02}_{-0.02}$	$-0.13^{+0.02}_{-0.02}$	$-0.17^{+0.02}_{-0.02}$	$-0.121^{+0.009}_{-0.011}$	$-0.141^{+0.009}_{-0.010}$
$\sigma_{c_{\text{int}}}$	$0.042^{+0.004}_{-0.004}$	$0.012^{+0.007}_{-0.008}$	$0.043^{+0.005}_{-0.004}$	$0.013^{+0.007}_{-0.008}$	$0.040^{+0.006}_{-0.005}$	$0.014^{+0.007}_{-0.008}$	$0.045^{+0.004}_{-0.003}$	$0.021^{+0.004}_{-0.005}$
τ	$0.033^{+0.005}_{-0.004}$	$0.031^{+0.005}_{-0.005}$	$0.031^{+0.005}_{-0.005}$	$0.033^{+0.004}_{-0.004}$	$0.033^{+0.007}_{-0.006}$	$0.036^{+0.006}_{-0.005}$	$0.042^{+0.005}_{-0.005}$	$0.039^{+0.004}_{-0.004}$
α	$-0.20^{+0.01}_{-0.01}$		$-0.20^{+0.01}_{-0.01}$		$-0.19^{+0.01}_{-0.01}$		$-0.200^{+0.009}_{-0.009}$	
β	$1.13^{+0.2}_{-0.10}$		$1.13^{+0.2}_{-0.10}$		$1.2^{+0.2}_{-0.1}$		$1.09^{+0.1}_{-0.07}$	
$\hat{R}_B$	$3.9^{+0.1}_{-0.1}$		$3.9^{+0.1}_{-0.1}$		$3.9^{+0.1}_{-0.1}$		$3.89^{+0.10}_{-0.09}$	
σ_{R_B}	$0.29^{+0.02}_{-0.01}$		$0.29^{+0.02}_{-0.01}$		$0.29^{+0.02}_{-0.02}$		$0.29^{+0.01}_{-0.01}$	
γ	$4.0^{+1.3}_{-0.8}$		$3.9^{+1.0}_{-0.8}$		$3.9^{+1.4}_{-0.9}$		$2.7^{+0.5}_{-0.4}$	
f_{prompt}	$0.51^{+0.06}_{-0.06}$		$0.67^{+0.05}_{-0.05}$		$0.66^{+0.05}_{-0.06}$		$0.70^{+0.03}_{-0.04}$	
$\Delta \log \mathcal{Z}$	0.0		$52.88^{+0.08}_{-0.10}$		-		-	
$\tilde{d}$	$18.8^{+0.6}_{-0.4}$		$8.06^{+0.08}_{-0.07}$		$5.35^{+0.05}_{-0.05}$		$6.02.0^{+0.07}_{-0.06}$	

TABLE 6.1.
Comparison between the baseline redshift-dependent model fit to the fiducial Pantheon+ sub-sample (first two columns) as well as the redshift-dependent model fit to the conservative and full Pantheon+ sub-samples. Parameter values are posterior medians, with errors given by the 16th and 86th percentiles. Bayes' factors $\Delta \mathcal{Z}$ are calculated wrt. the BAYESNOVA baseline model, and is only calculated for the redshift-dependent model fit to the fiducial sub-sample. BMDs $\tilde{d}$ for model comparison's sake.

for population 1 they still struggle to capture the evolution of stretch at low redshift.

6.2 Joint Volumetric Rate / SNe Ia Constraints

We have shown that the DTD prompt fraction f_{prompt} can be constrained at a precision close to current best measurements. Due to how redshift-dependence is implemented in the two-population model, however, we can not constrain the DTD normalization η. By combining volumetric SNe Ia rate measurements (see Section 3.5) with SNe Ia catalog observations, we can jointly constrain SNe Ia sub-populations and the DTD parameters f_{prompt} and η. We present the results of these model fits in the first two columns of Table 6.2. We see that SNe Ia population parameters are essentially unchanged compared to Table 6.1. This is to be expected, since the DTD contributes to the SNe Ia population fraction, which only depends on the prompt fraction f_{prompt} and is independent of η.

Constraints on f_{prompt} are consistent with the previous result, implying that under the assumptions of the redshift-dependent model the light-curve parameters are suf-
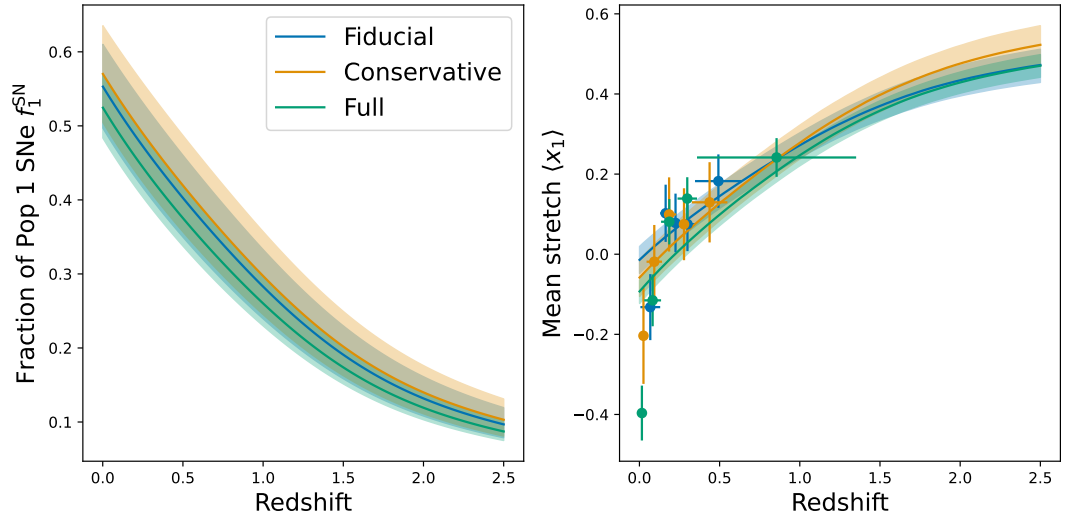
FIGURE 6.1.
Left: Redshift-dependent SNe Ia population 1 fraction for models fit to the fiducial, conservative and full Pantheon+ sub-samples. Lines show posterior medians while shaded regions show the 68% confidence interval. *Right*: Observed mean SNe Ia stretch compared to the predicted redshift evolution of mean population stretch, given by Eq. 6.1. Each sub-sample is divided into 5 bins of varying width such that each bin contains approximately the same no. of observations.

ficient to constrain the DTD progenitor fractions. The recovered normalizations are lower than but consistent with results in the literature, with $\eta = 1.60^{+0.25}_{-0.6} \frac{10^{-4}\,h^2_{70}}{\mathrm{yr\,M_\odot}}$ and $1.02^{0.27}_{-0.15} \frac{10^{-4}\,h^2_{70}}{\mathrm{yr\,M_\odot}}$ reported by Rodney *et al.*, 2014 and Wojtak *et al.*, 2019, respectively. We note again that our results have increased precision by a factor of roughly two, showing that the light-curve observables and volumetric rates are complementary when it comes to constraining the DTD normalization.

In Fig. 6.2 we compare the posterior volumetric rates with the volumetric SNe Ia rate measurements. We see that the volumetric rate follows a similar redshift evolution as reported in Wojtak *et al.*, 2019 and shown in Fig. 6.2, with the prompt channel producing the majority of SNe Ia at high redshift, and both channels contributing roughly equally at low redshift. Compared to Wojtak *et al.*, 2019, the volumetric rate is tightly constrained, with errors being small compared to that of observations. This could indicate that the majority of the constraining power comes from the SNe Ia light-curve observables, such that the volumetric rate observations do not contribute majorly beyond the normalization.
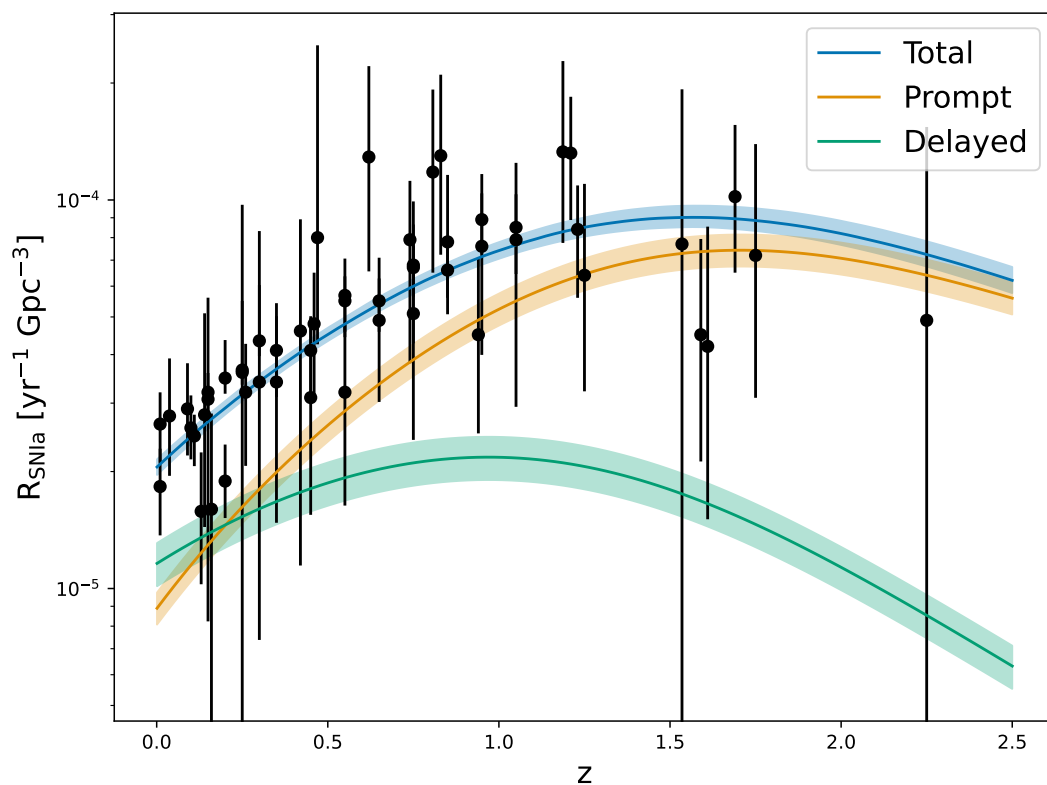
FIGURE 6.2.
Comparison of observed volumetric SNe Ia rates and the posterior volumetric rate obtained from a joint fit of the fiducial Pantheon+ sub-sample and volumetric rate observations. Solid lines show median values, while shaded regions show the 68% confidence interval. See Table 6.2 for parameter values f_{prompt} and η used.

| Model | Redshift-Dependent | | Redshift-Dependent | | Redshift-Dependent | |
| Sub-sample | Pantheon+ Fiducial | | Pantheon+ Conservative | | Pantheon+ Full | |
Supp. Data	Volumetric Rates		Volumetric Rates		Volumetric Rates	
	SNe Pop 1	SNe Pop 2	SNe Pop 1	SNe Pop 2	SNe Pop 2	SNe Pop 2
$\hat{M}_B$	$-19.63^{+0.04}_{-0.04}$	$-19.56^{+0.05}_{-0.06}$	$-19.61^{+0.04}_{-0.05}$	$-19.56^{+0.06}_{-0.07}$	$-19.56^{+0.03}_{-0.03}$	$-19.47^{+0.03}_{-0.03}$
$\hat{X}_1$	$-0.48^{+0.09}_{-0.09}$	$0.58^{+0.05}_{-0.05}$	$-0.6^{+0.1}_{-0.1}$	$0.65^{+0.06}_{-0.06}$	$-0.72^{+0.9}_{-0.9}$	$0.56^{+0.04}_{-0.04}$
σ_{X_1}	$0.80^{+0.05}_{-0.05}$	$0.49^{+0.04}_{-0.04}$	$0.79^{+0.06}_{-0.06}$	$0.45^{+0.04}_{-0.04}$	$0.84^{+0.04}_{-0.04}$	$0.50^{+0.03}_{-0.03}$
$\hat{c}_{\text{int}}$	$-0.13^{+0.01}_{-0.01}$	$-0.16^{+0.02}_{-0.02}$	$-0.13^{+0.02}_{-0.02}$	$-0.17^{+0.02}_{-0.02}$	$-0.117^{+0.09}_{-0.010}$	$-0.138^{+0.009}_{-0.010}$
$\sigma_{c_{\text{int}}}$	$0.043^{+0.005}_{-0.004}$	$0.013^{+0.007}_{-0.008}$	$0.040^{+0.006}_{-0.005}$	$0.014^{+0.007}_{-0.008}$	$0.044^{+0.004}_{-0.003}$	$0.021^{+0.004}_{-0.004}$
τ	$0.031^{+0.005}_{-0.005}$	$0.033^{+0.004}_{-0.004}$	$0.033^{+0.007}_{-0.006}$	$0.036^{+0.006}_{-0.005}$	$0.044^{+0.005}_{-0.005}$	$0.040^{+0.004}_{-0.004}$
α	$-0.20^{+0.01}_{-0.01}$		$-0.19^{+0.01}_{-0.01}$		$-0.198^{+0.08}_{-0.08}$	
β	$1.13^{+0.2}_{-0.10}$		$1.2^{+0.2}_{-0.1}$		$1.09^{+0.14}_{-0.07}$	
$\hat{R}_B$	$3.9^{+0.1}_{-0.1}$		$3.9^{+0.1}_{-0.1}$		$3.83^{+0.09}_{-0.09}$	
σ_{R_B}	$0.29^{+0.02}_{-0.01}$		$0.29^{+0.02}_{-0.02}$		$0.28^{+0.01}_{-0.01}$	
γ	$3.9^{+1.0}_{-0.8}$		$3.9^{+1.4}_{-0.9}$		$2.6^{+0.5}_{-0.4}$	
f_{prompt}	$0.66^{+0.04}_{-0.05}$		$0.65^{+0.05}_{-0.05}$		$065^{+0.04}_{-0.04}$	
$\eta\,[\frac{10^{-4}\,h_{70}^2}{\text{yr M}_\odot}]$	$0.78^{+0.1}_{-0.01}$		$0.80^{+0.1}_{-0.1}$		$0.79^{+0.9}_{-0.8}$	
$\tilde{d}$	$6.95^{+0.07}_{-0.07}$		$5.35^{+0.05}_{-0.05}$		$8.32^{+0.1}_{-0.10}$	

TABLE 6.2.
Comparison between redshift-dependent models fit to different datasets in combination with volumetric SNe Ia rate measurements. Parameter values are posterior medians, with errors covering the 68% confidence interval. Model BMDs $\tilde{d}$ shown for model comparison's sake.

Cosmological Constraints 7

We have so far focused on astrophysical aspect of modelling SNe Ia, quantifying the impact of catalog changes between SuperCal and Pantheon+, exploring the impact of including host properties, and constraining the SNe Ia progenitor DTD. In this section we increase the scale of the analysis, focusing on the usage of SNe Ia as cosmological probes. A SNe Ia sub-sample with a high redshift-range such as Pantheon+ allows for constraints to be put on the density parameters and equation for state described in Section 1.1. We will in this work test 3 different models: a FlatΛCDM model where the matter density $\Omega_{m,0}$ is free, a Flat$w$CDM model where $\Omega_{m,0} = 0.3$, and a FlatΛCDM model where both $\Omega_{m,0}$ and w_0 are free parameters. These 3 models are covered in Sections 7.1, ??, 7.3.1, respectively.

Strong support two SNe Ia sub-populations that evolve over redshift, as shown in the previous section, has implications for constraints on the mentioned cosmological parameters. We showed in the previous section that these two populations have different intrinsic luminosities, stretch parameters and colors. Standard cosmological SNe Ia surveys assume a single population of SNe when using the Tripp calibration, with some variation allowed via usage of the mass-step described in Section 1.2.1. If observed SNe Ia are produced by two distinct underlying populations, such an assumption would lead to SNe Ia that are intrinsically dimmer / redder / in dustier environments to be falsely assigned higher distance moduli. This in turn changes the relative distances of the SNe, and an lead to biases in constraints. To quantify this potential bias, we simulate 200 mock Pantheon+ catalogs containing 2000 SNe Ia each, with redshifts sampled uniformly in the range $0.01 < z < 2.5$. Light-curve observables m_B, x_1, and c_{app} are generated by sampling from the redshift-dependent two-population model defined in Chapter 2, with parameters chosen to those reported in Table 6.1 for the fiducial sub-sample. Cosmological parameters are fixed to those defined in Section 1.1, with $\Omega_{m,0} = 0.3$ and $w_0 = -1$. For each of the 200 mock catalogs we resample while allowing f_{prompt} to vary between $0.01 - 0.99$ with step sizes of $\Delta f = 0.01$. By doing so we have 200 mock catalogs for each value of f_{prompt}.

Given the simulated mocks, the potential bias can be estimated by fitting a single-population Tripp model as defined in Eq. 1.16, leaving the chosen cosmological parameters free. Note that this model has intrinsic scatter σ_{int} free, as this is only

fixed to 0 for the baseline model. We define the resulting percent bias in $\Omega_{m,0}$ and w_0 to be

$$\delta\Omega_{m,0} = \frac{\Omega_{m,0}^{\text{Fit}} - \Omega_{m,0}^{\text{True}}}{\Omega_{m,0}^{\text{True}}} \tag{7.1}$$

$$\delta w_0 = \frac{w_0^{\text{Fit}} - w_0^{\text{True}}}{w_0^{\text{True}}}. \tag{7.2}$$

Note that since $w_0^{\text{True}} = -1$ that positive values of δw_0 correspond to underestimated or overly negative w_0^{Fit}. Similarly, negative values of δw_0 correspond to overestimated or overly positive w_0^{Fit} with respect to w_0^{True}.

7.1 Constraining Matter Density

7.1.1 Simulations

The first model we consider is FlatΛCDM where the only free parameter is the matter density $\Omega_{m,0}$. We fit a single-population Tripp model given by Eq. 1.16 to the 200 sets of mock Pantheon+ catalogs, thereby measuring the percent-level bias as a function of f_{prompt}. The result of this is shown in Fig. 7.1. We see that $\delta\Omega_{m,0}$ is generally underestimated, with a symmetry around $f_{\text{prompt}} \approx 0.5$. This corresponds to equal contribution of the two sub-populations, leading to a bias of $\delta\Omega_{m,0} \approx -2\%$. One would expect the bias to reduce to 0 for $f_{\text{prompt}} = 0$ or $f_{\text{prompt}} = 0$, but this is not the case in Fig. 7.1. This can be explained by the fact that the simulated data include the effects of dust, which were not included in the simple Tripp model used to recover $\Omega_{m,0}$. Mandel *et al.*, 2017 show that that distance moduli are overestimated by 0.1 mag when SNe Ia apparent color is not deconvolved into intrinsic color and dust distribution. Assuming a FlatΛCDM model as we are now, this would correspond to an underestimation as we see in Fig. 7.1.

What then, is the contribution from the mixture of SNe Ia populations to this bias? The single-population model must account for underlying SNe Ia properties that evolve with time. As seen in Fig. 6.1, the proportion of population 2 SNe Ia increases as a function of redshift. This population of SNe Ia is intrinsically blue and has high stretch, compared to population 1. Modelling the SNe Ia stretch as coming from a single population when f_{prompt} would lead to a population stretch between the $\hat{X}_1$ and $\hat{X}_2$ in Table 6.1. This would in turn lead to overestimated luminosities for population 1 and vice-versa for population 2. Considering Eq. 1.9, this scenario could correspond to a Universe that became dominated by the accelerating expansion of the Λ-component at an earlier time, which would correspond to a lower value
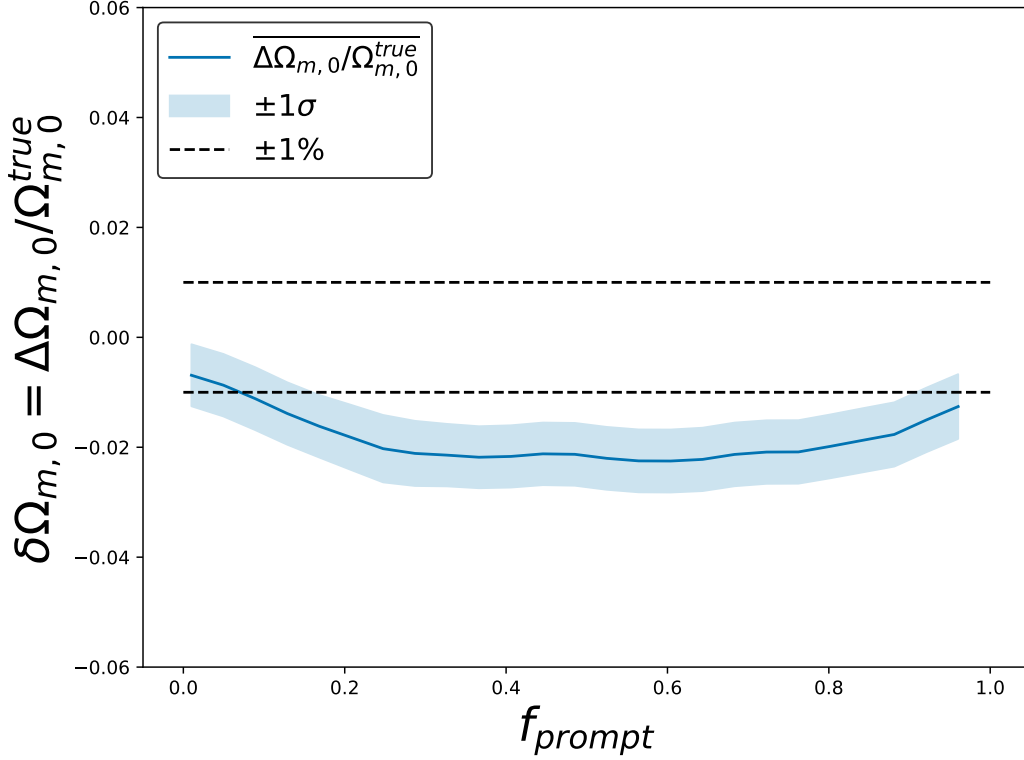
FIGURE 7.1.
Bias in $\Omega_{m,0}$ as a function of f_{prompt}. Colored lines depict the average bias across 200 simulations, smoothed using a Gaussian kernel with $\sigma = 1$. Shaded region shows $\pm 1\sigma$-interval, and dashed line shows $\pm 1\%$ from the true value

of $\Omega_{m,0}$. Considering the bias contribution from the two populations as well as from unmodelled dust both lead to underestimation, we expect this bias to be less significant when using a more physical model. We leave such an analysis, using the dust-extended Tripp model in Eq. 1.18 for future work.

7.1.2 Results

Having studied potential systematics in $\Omega_{m,0}$ using simulations, we now move onward to constraining the parameter using the Pantheon+ catalog. We present results for the fiducial and conservative sub-samples in Table 7.1. The full sub-sample is not evaluated fact that systematics caused by unaccounted for selection effects can obscure any shifts in the cosmological parameters due to the adopted two-population model. We have left out constraints on SNe Ia parameters, as they are all found to be within $< 1\sigma$ of the values found in Table 6.1.

As shown in Table 7.1, we find values of $\Omega_{m,0}$ higher than that measured by Brout *et al.*, 2022a, $\Omega_{m,0} = 0.326 \pm 0.16$, which we would expect based on our previous simulation study. The size of our errors means that we, however, are still consistent

Model	Redshift-Dependent		Redshift-Dependent	
Sub-sample	Pantheon+ Fiducial		Pantheon+ Conservative	
	SNe Pop 1	SNe Pop 2	SNe Pop 1	SNe Pop 2
f_{prompt}	$0.64^{+0.04}_{-0.05}$		$0.65^{+0.05}_{-0.05}$	
$\Omega_{m,0}$	$0.37^{+0.02}_{-0.02}$		$0.36^{+0.03}_{-0.03}$	
$\Delta \log \mathcal{Z}$	$5.33^{+0.06}_{-0.06}$		$4.12^{+0.06}_{-0.07}$	
$\tilde{d}$	$3.05^{+0.04}_{-0.03}$		$8.3^{+0.11}_{-0.10}$	

TABLE 7.1.
Comparison between the redshift-dependent model fit to the fiducial, conservative and full Pantheon+ sub-samples with $\Omega_{m,0}$ as a free parameter. We show only the marginalized population fraction and cosmological parameters for the readers' sake, as remaining SNe Ia and dust parameters are equivalent $< 1\sigma$ of those found Table 6.1. Parameter values are given posterior medians, with errors given by the 16th and 86th percentiles. Bayes' factors $\Delta \mathcal{Z}$ are calculated wrt. the redshift-dependent models with fiducial cosmology presented in Table 6.1. BMDs $\tilde{d}$ are shown for model comparison's sake.

with the results presented in Brout *et al.*, 2022a, and no evidence is found for any bias in the Pantheon+ results.

7.2 Constraining The Dark Energy Equation of State

7.2.1 Simulations

The second model we consider is Flat$w$CDM where the only free parameter is the dark energy equation of state parameter w_0. As before, we fit a single-population Tripp model given by Eq. 1.16 to the 200 sets of mock Pantheon+ catalogs, thereby measuring the percent-level bias as a function of f_{prompt}. The result of this is shown in Fig. 7.2.

Similar to before, we find $\delta w_0 \lesssim 0$ with an apparent symmetry around $f_{\text{prompt}} \approx 0.5$. This corresponds to equal contribution of the two sub-populations, leading to a bias of $\delta w_0 \approx -1\%$, although $\delta w_0 = 0$ is within 3σ at all times. Ignoring the contributions of unaccounted for dust, we can attribute the slight negative bias similarly to the FlatΛCDM case, where instead the biases in distance moduli are accounted for by w_0. Since the bias is negative, this corresponds to $w_0^{f\text{it}} > -1$. A value of $-1 < w_0 < -1/3$ corresponds to a Universe that becomes dark energy dominated at an earlier
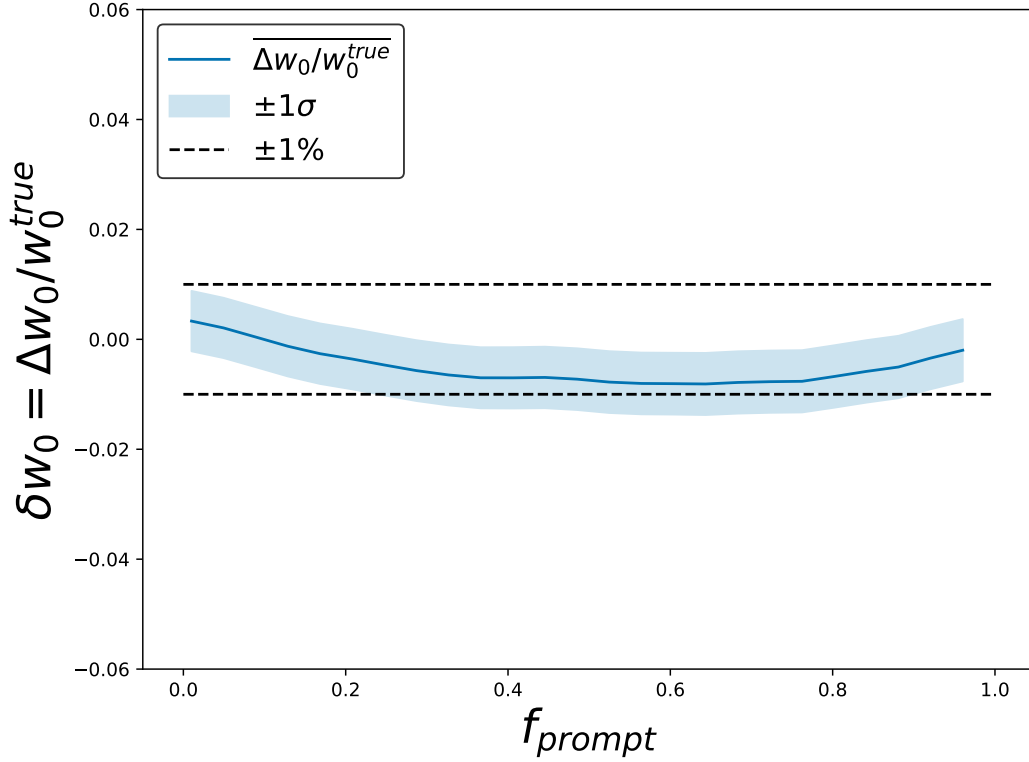
FIGURE 7.2.
Bias in w_0 as a function of f_{prompt}. Colored lines depict the average bias across 200 simulations, smoothed using a Gaussian kernel with $\sigma = 1$. Shaded region shows $\pm 1\sigma$-interval, and dashed line shows $\pm 1\%$ from the true value

time. In this way, the single-population model can account for the impact of the two underlying sub-populations by overestimating the value w_0. If we consider Eq. 1.9, we see that w_0 enters in the exponent of the scale factor for the Λ-component, $a^{-3(1+w)}$. This may explain why the observed bias is small, since a minor change in the exponent will lead to large change as a function of a.

7.2.2 Results

Having shown that a weak bias may be present in constraints of w_0, we will now attempt to constrain this parameter using the Pantheon+ catalog. We present results for the fiducial and conservative sub-samples in Table 7.2. The full sub-sample is not evaluated due to the fact that systematics caused by unaccounted for selection effects can obscure any shifts in the cosmological parameters due to the adopted two-population model. We have left out constraints on SNe Ia parameters, as they are all found to be within $< 1\sigma$ of the values found in Table 6.1.

We find $w_0 = -0.84 \pm 0.04$ and $w_0 = -0.83 \pm 0.03$ for the fiducial and conservative sub-samples, respectively. These values are marginally lower than the value reported

| Model | Redshift-Dependent | | Redshift-Dependent | |
| Sub-sample | Pantheon+ Fiducial | | Pantheon+ Conservative | |
	SNe Pop 1	SNe Pop 2	SNe Pop 1	SNe Pop 2
f_{prompt}	$0.66^{+0.05}_{-0.06}$		$0.67^{+0.03}_{-0.04}$	
w_0	$-0.84^{+0.04}_{-0.04}$		$-0.83^{+0.03}_{-0.03}$	
$\Delta \log \mathcal{Z}$	$3.01^{+0.06}_{-0.06}$		$4.92^{+0.07}_{-0.06}$	
$\tilde{d}$	$2.29^{+0.03}_{-0.03}$		$9.2^{+0.1}_{-0.1}$	

TABLE 7.2.
Comparison between the redshift-dependent model fit to the fiducial and conservative Pantheon+ sub-samples with w_0 as a free parameter. We show only the marginalized population fraction and cosmological parameters for the readers' sake, as remaining SNe Ia and dust parameters are equivalent $< 1\sigma$ of those found Table 6.1. Parameter values are given posterior medians, with errors given by the 16th and 86th percentiles. Bayes' factors $\Delta \mathcal{Z}$ are calculated wrt. the redshift-dependent models with fiducial cosmology presented in Table 6.1. BMDs $\tilde{d}$ are shown for model comparison's sake.

by Brout *et al.*, 2022a in their joint analysis, but consistent within $< 2\sigma$. As such we find no evidence of any shifts in the dark energy equation of state when using a two population model. It is interesting to note that the value does slightly shift to higher values, as we would expect the opposite based on the previous simulation study.

7.3 Joint Constraints

7.3.1 Simulations

Last but not least, we consider a Flat$w$CDM where both the matter density, $\Omega_{m,0}$, and the dark energy equation of state, w_0, parameters are allowed to vary. As before, we fit a single-population Tripp model given by Eq. 1.16 to the 200 sets of mock Pantheon+ catalogs, thereby measuring the joint percent-level bias as a function of f_{prompt}. The result of this is shown in Fig. 7.3.

In this joint-model scenario, we see a negative bias in both $\Omega_{m,0}$ and w_0. Unexpectedly, these biases are both roughly a factor 2 larger than the individual biases found in the previous simulation experiments, with $\delta\Omega_{m,0} \approx -4\%$ and $\delta w_0 \approx -2\%$ at peak. The location of the largest bias is also shifted to $f_{\mathrm{prompt}} \approx 0.4$, vs $f_{\mathrm{prompt}} \approx 0.5$ as seen earlier. The physical reasoning behind the underestimation of $\Omega_{m,0}$ and overestimation of w_0 is the same as in the earlier sections, with the biases corresponding
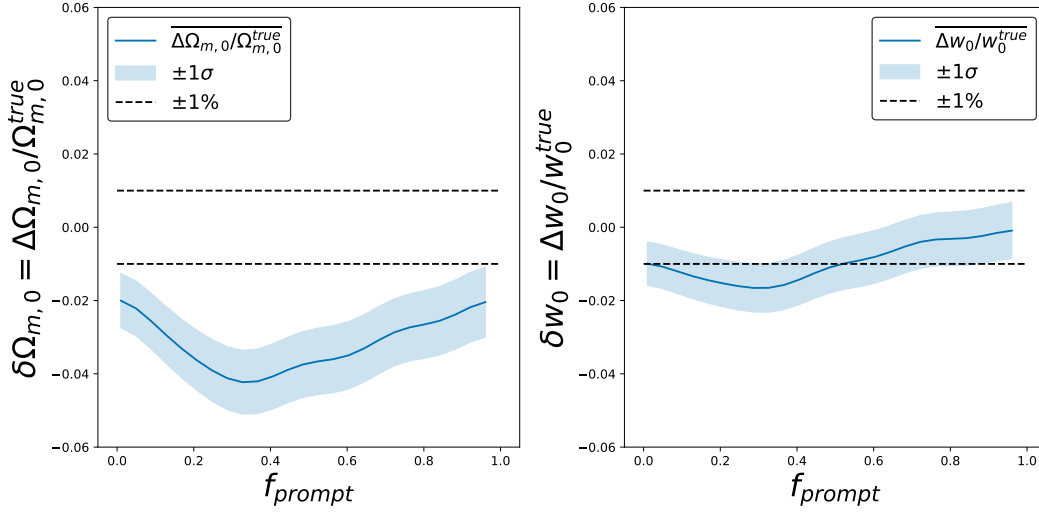
FIGURE 7.3.
Left: Bias in $\Omega_{m,0}$ as a function of f_{prompt}. *Right*: Bias in w_0 as a function of f_{prompt}. Colored lines depict the average bias across 200 simulations, smoothed using a Gaussian kernel with $\sigma = 1$. Shaded region shows $\pm 1\sigma$-interval, and dashed line shows $\pm 1\%$ from the true value.

to a Universe dominated by expansion at an earlier time to account for biased distance moduli. When both parameters are free, one would expect that the individual contributions from each are reduced, not increased as we see in this case. This may also be an artifact of the analysis, as we instead should consider the joint bias in the $\Omega_{m,0} - w_0$ space, instead of bias on the marginalized parameters as we are currently doing. We leave a deeper analysis of this interesting interplay between cosmological parameters for further study in the future.

7.3.2 Results

We now turn towards constraining $\Omega_{m,0}$ and w_0 on the Pantheon+ catalog. We present results for the fiducial, conservative and full sub-samples in Table 7.3. We have left out constraints on SNe Ia parameters, as they are all found to be within $< 1\sigma$ of the values found in Table 6.1.

We find that the fiducial and conservative sub-samples agree with the constraints given by Brout *et al.*, 2022a within $< 1\sigma$. Compared to the previous two models, the constraints presented in Table 7.3 are a factor 2 less precise. This can be explained by the degeneracy in $\Omega_{m,0}$ and w_0 as shown in Fig. 7.4, in combination with the reduced redshift range in the fiducial and conservative sub-samples.
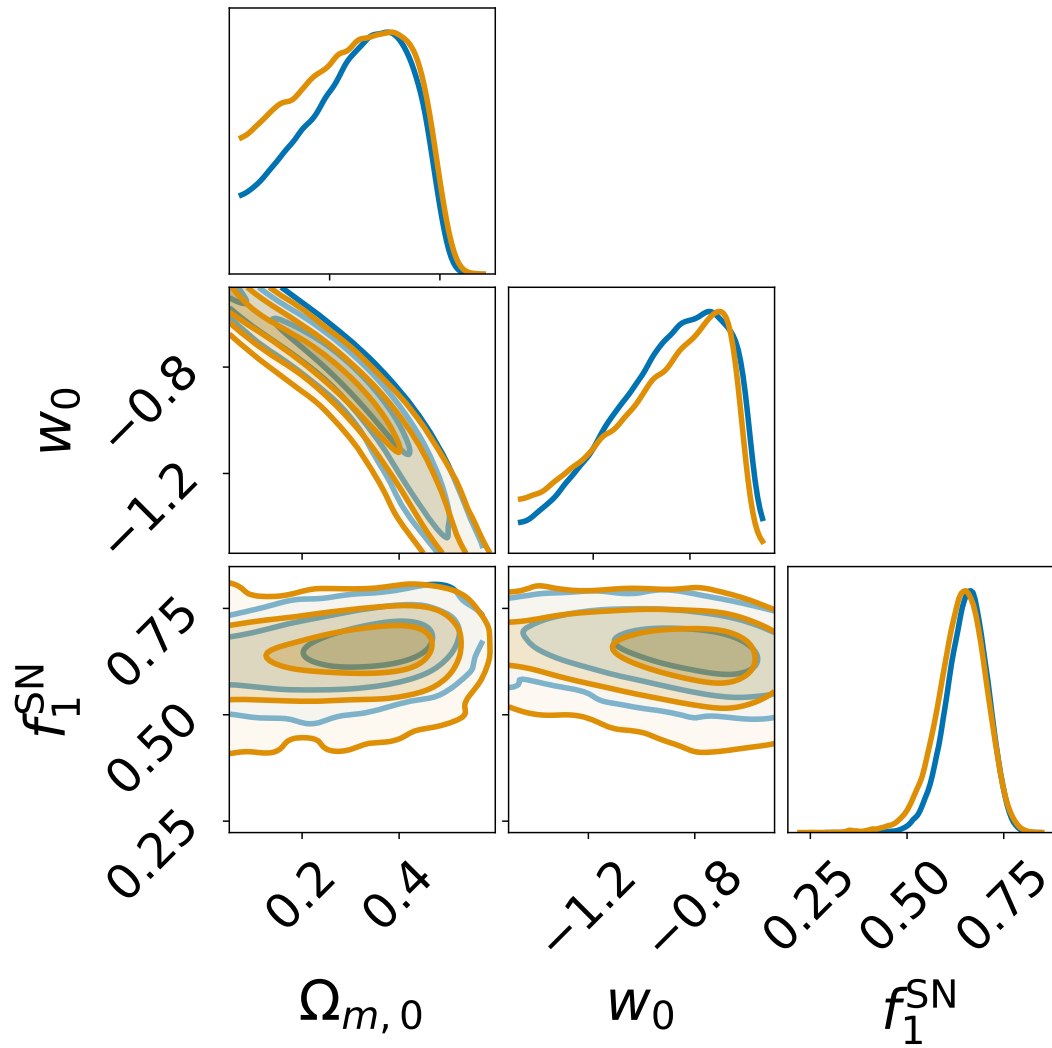
FIGURE 7.4.
Posterior distributions for DTD prompt fraction, $\Omega_{m,0}$ and w for the fiducial and conservative Pantheon+ sub-samples. These are shown in blue and orangerespectively.

Model	Redshift-Dependent		Redshift-Dependent	
Sub-sample	Pantheon+ Fiducial		Pantheon+ Conservative	
	SNe Pop 1	SNe Pop 2	SNe Pop 1	SNe Pop 2
f_{prompt}	$0.66^{+0.05}_{-0.06}$		$0.64^{+0.06}_{-0.07}$	
$\Omega_{m,0}$	$0.3^{+0.1}_{-0.2}$		$0.3^{+0.1}_{-0.2}$	
w_0	$-0.9^{+0.2}_{-0.3}$		$-0.9^{+0.2}_{-0.3}$	
$\Delta \log \mathcal{Z}$	$5.08^{+0.10}_{-0.09}$		$4.3^{+0.34}_{-0.09}$	
$\tilde{d}$	$4.45^{+0.05}_{-0.05}$		$4.78^{+0.06}_{-0.04}$	

TABLE 7.3.
Comparison between the redshift-dependent model fit to the fiducial and conservative Pantheon+ sub-samples with $\Omega_{m,0}$ and w_0 as free parameters. We show only the marginalized population fraction and cosmological parameters for the readers' sake, as remaining SNe Ia and dust parameters are equivalent $< 1\sigma$ of those found Table 6.1. Parameter values are given posterior medians, with errors given by the 16th and 86th percentiles. Bayes' factors $\Delta\mathcal{Z}$ are calculated wrt. the redshift-dependent models with fiducial cosmology presented in Table 6.1. BMDs $\tilde{d}$ are shown for model comparison's sake.

Summary & Conclusion

8

We have in this work touched upon a large fraction of the SNe Ia field, as it pertains to cosmology. We introduced how SNe Ia are used to constrain cosmological parameters, but also how issues currently exist wrt. their usage as cosmological probes. Specifically this refers to intrinsic dispersion in SNe Ia, as well as the potential relation between SNe Ia systematics and the Hubble tension, as discussed in Section 1.4.2. Wojtak *et al.*, 2023 introduced a novel hierarchical two-population model which allows for the existence of two sub-populations of SNe Ia. We have in this work taken this model and generalized it in the form of the Python package BAYESNOVA.

We have in Chapter 2 introduced a several extensions to make the model more physical, such as extensions to the latent priors on the extinction coefficient and dust redddening. We compared results derived by Wojtak *et al.*, 2023 and BAYESNOVA on the SuperCal catalog, finding some discrepancies but overall agreeance. Further work is needed here to fully quantify what causes these differences, although experiments during this thesis have shown that it may be due to slight differences in the preprocessing pipeline introduced in Chapter 3. We have then moved on to the modern SNe Ia catalog, again comparing with the results of Wojtak *et al.*, 2023. We here find some larger differences in posterior values, especially for the color, stretch and Tripp parameter β. We attempted to use modern Bayesian methodology to determine the cause of this tension, but where unsuccessfull due to the assumption that SuperCal and Pantheon+ are independent. Future work will attempt to determine the cause of these differences, potentially by implementing the full covariance matrix of Scolnic *et al.*, 2022 in BAYESNOVA.

We aimed to study the impact of host properties in the framework of a two-population model, and this has beeen implemented in BAYESNOVA. As discussed in Chapter 2, this is one avenue of improving constraints on the presence of SNe Ia two-populations. Technical issues with sampling these high-dimensional posteriors has however prevented these results from making their way into this thesis. We hope to present these results at the upcoming defence, as well as include them in an updated version of this document in the future.

The main extension to Wojtak *et al.*, 2023 is the inclusion of redshift dependence in the relative weighting of the two SNe Ia sub-populations. This is done by making

use of the SNe Ia DTD and volumetric rates, linking the populations of this observational light-curve based model to theoretical SNe Ia progenitor channels. This serves as a way to use light-curve observables directly to constrain SNe Ia, and we have shown in Chapter 6 that we find results consistent with the latest constraints but at a higher level of precision. Some issues persist, with the posterior predictive distribution of SNe Ia stretch being impacted by this model extension. Further work will be dedicated to studying this further.

Finally, we have in this work applied this redshift-dependenet two-population model to constraining cosmological parameters using high-redshift SNe Ia surveys such as Pantheon+.

Bibliography

Alenlöv, Johan, Arnaud Doucet, and Fredrik Lindsten (Oct. 2019). *Pseudo-Marginal Hamiltonian Monte Carlo*. arXiv: 1607.02516 [stat].

Betancourt, Michael (n.d.). *Hierarchical Modeling*. https://betanalpha.github.io/assets/case_studies/

Bloom, Joshua S. *et al.* (Jan. 2012). "A Compact Degenerate Primary-Star Progenitor of SN 2011fe". In: *The Astrophysical Journal* 744.2, p. L17. arXiv: 1111.0966 [astro-ph].

Briday, M. *et al.* (Jan. 2022). "Accuracy of Environmental Tracers and Consequences for Determining the Type Ia Supernova Magnitude Step". In: *Astronomy & Astrophysics* 657, A22.

Brout, Dillon and Daniel Scolnic (Mar. 2021). "It's Dust: Solving the Mysteries of the Intrinsic Scatter and Host-Galaxy Dependence of Standardized Type Ia Supernova Brightnesses". In: *The Astrophysical Journal* 909.1, p. 26. arXiv: 2004.10206 [astro-ph].

Brout, Dillon *et al.* (Feb. 2022a). *The Pantheon+ Analysis: Cosmological Constraints*. arXiv: 2202.04077 [astro-ph].

Brout, Dillon *et al.* (Oct. 2022b). "The Pantheon+ Analysis: SuperCal-fragilistic Cross Calibration, Retrained SALT2 Light-curve Model, and Calibration Systematic Uncertainty". In: *The Astrophysical Journal* 938.2, p. 111.

CFHTLS Final Release Executive Summary (n.d.). https://www.cfht.hawaii.edu/Science/CFHTLS/cfht

Chambers, K. C. *et al.* (Jan. 2019). *The Pan-STARRS1 Surveys*. arXiv: 1612.05560 [astro-ph].

Di Valentino, Eleonora, Olga Mena, Supriya Pan, Luca Visinelli, Weiqiang Yang, Alessandro Melchiorri, David F Mota, Adam G Riess, and Joseph Silk (July 2021). "In the Realm of the Hubble Tension—a Review of Solutions [*]". In: *Classical and Quantum Gravity* 38.15, p. 153001.

Draine, B.T. (Sept. 2003). "Interstellar Dust Grains". In: *Annual Review of Astronomy and Astrophysics* 41.1, pp. 241–289.

El-Badry, Kareem *et al.* (June 2023). *The Fastest Stars in the Galaxy*. arXiv: 2306. 03914 [astro-ph].

Frieman, Joshua A. *et al.* (Jan. 2008). "THE SLOAN DIGITAL SKY SURVEY-II SUPERNOVA SURVEY: TECHNICAL SUMMARY". In: *The Astronomical Journal* 135.1, pp. 338–347.

Hamuy, Mario, M. M. Phillips, Robert A. Schommer, Nicholas B. Suntzeff, José Maza, and R. Avilés (Dec. 1996). "The Absolute Luminosities of the Calan/Tololo Type Ia Supernovae". In: *The Astronomical Journal* 112, p. 2391. arXiv: astro-ph/ 9609059.

Handley, Will and Pablo Lemos (July 2019a). "Quantifying Dimensionality: Bayesian Cosmological Model Complexities". In: *Physical Review D* 100.2, p. 023512.

– (Aug. 2019b). "Quantifying Tensions in Cosmological Parameters: Interpreting the DES Evidence Ratio". In: *Physical Review D* 100.4, p. 043504.

Hillebrandt, W., M. Kromer, F. K. Röpke, and A. J. Ruiter (Feb. 2013). *Towards an Understanding of Type Ia Supernovae from a Synthesis of Theory and Observations*. arXiv: 1302.6420 [astro-ph].

Hogg, David W., Adrian M. Price-Whelan, and Boris Leistedt (May 2020). *Data Analysis Recipes: Products of Multivariate Gaussians in Bayesian Inferences*. arXiv: 2005. 14199 [astro-ph, physics:physics, stat].

Hoyle, F (n.d.). "NUCLEOSYNTHESIS IN SUPERNOVAE". In: *ApJ...* ().

Joachimi, B., F. Köhlinger, W. Handley, and P. Lemos (Mar. 2021). "When Tension Is Just a Fluctuation: How Noisy Data Affect Model Comparison". In: *Astronomy & Astrophysics* 647, p. L5.

Jones, D. O. *et al.* (Nov. 2018). "Should Type Ia Supernova Distances Be Corrected for Their Local Environments?" In: *The Astrophysical Journal* 867.2, p. 108.

Jones, D. O. *et al.* (Aug. 2019). "The Foundation Supernova Survey: Measuring Cosmological Parameters with Supernovae from a Single Telescope". In: *The Astrophysical Journal* 881.1, p. 19.

Jones, David O., Adam G. Riess, and Daniel M. Scolnic (Oct. 2015). "RECONSIDERING THE EFFECTS OF LOCAL STAR FORMATION ON TYPE Ia SUPERNOVA COSMOLOGY". In: *The Astrophysical Journal* 812.1, p. 31.

Keeley, Ryan E. and Arman Shafieloo (July 2022). "On The Distribution of Bayesian Evidences". In: *Monthly Notices of the Royal Astronomical Society* 515.1, pp. 293–301. arXiv: 2111.04231 [astro-ph].

Kelly, Brandon C. (Aug. 2007). "Some Aspects of Measurement Error in Linear Regression of Astronomical Data". In: *The Astrophysical Journal* 665.2, pp. 1489–1506.

Lemos, Pablo, Fabian Köhlinger, Will Handley, Benjamin Joachimi, Lorne Whiteway, and Ofer Lahav (Aug. 2020). "Quantifying Suspiciousness within Correlated Data Sets". In: *Monthly Notices of the Royal Astronomical Society* 496.4, pp. 4647–4653.

Li, Weidong, Ryan Chornock, Jesse Leaman, Alexei V. Filippenko, Dovi Poznanski, Xiaofeng Wang, Mohan Ganeshalingam, and Filippo Mannucci (Apr. 2011). "Nearby Supernova Rates from the Lick Observatory Supernova Search - III. The Rate-Size Relation, and the Rates as a Function of Galaxy Hubble Type and Colour: Nearby Supernova Rates from LOSS - III". In: *Monthly Notices of the Royal Astronomical Society* 412.3, pp. 1473–1507.

Liu, Zheng-Wei, Friedrich K. Roepke, and Zhanwen Han (May 2023). *Type Ia Supernova Explosions in Binary Systems: A Review*. arXiv: 2305.13305 [astro-ph].

Llorente, F., L. Martino, E. Curbelo, J. Lopez-Santiago, and D. Delgado (Jan. 2023). "On the Safe Use of Prior Densities for Bayesian Model Selection". In: *WIREs Computational Statistics* 15.1. arXiv: 2206.05210 [stat].

Madau, Piero and Mark Dickinson (Aug. 2014). "Cosmic Star Formation History". In: *Annual Review of Astronomy and Astrophysics* 52.1, pp. 415–486. arXiv: 1403.0007 [astro-ph].

Mandel, Kaisey S., Daniel Scolnic, Hikmatali Shariff, Ryan J. Foley, and Robert P. Kirshner (June 2017). "The Type Ia Supernova Color-Magnitude Relation and Host Galaxy Dust: A Simple Hierarchical Bayesian Model". In: *The Astrophysical Journal* 842.2, p. 93. arXiv: 1609.04470 [astro-ph, stat].

Mannucci, F., M. Della Valle, N. Panagia, E. Cappellaro, G. Cresci, R. Maiolino, A. Petrosian, and M. Turatto (Apr. 2005). "The Supernova Rate per Unit Mass". In: *Astronomy & Astrophysics* 433.3, pp. 807–814.

Maoz, D. and F. Mannucci (2012). "Type-Ia Supernova Rates and the Progenitor Problem: A Review". In: *Publications of the Astronomical Society of Australia* 29.4, pp. 447–465.

Maoz, Dan, Filippo Mannucci, and Gijs Nelemans (Aug. 2014). "Observational Clues to the Progenitors of Type-Ia Supernovae". In: *Annual Review of Astronomy and Astrophysics* 52.1, pp. 107–170. arXiv: 1312.0628 [astro-ph].

Müller-Bravo, Tomás E. and Lluís Galbany (Aug. 2022). *HostPhot: Global and Local Photometry of Galaxies Hosting Supernovae or Other Transients*. arXiv: 2208.08117 [astro-ph].

Murakami, Yukei S., Adam G. Riess, Benjamin E. Stahl, W. D'Arcy Kenworthy, Dahne-More A. Pluck, Antonella Macoretta, Dillon Brout, David O. Jones, Dan M. Scolnic, and Alexei V. Filippenko (May 2023). *Leveraging SN Ia Spectroscopic Similarity to Improve the Measurement of H_0*. arXiv: 2306.00070 [astro-ph].

Nesseris, Savvas and Juan Garcia-Bellido (Aug. 2013). "Is the Jeffreys' Scale a Reliable Tool for Bayesian Model Comparison in Cosmology?" In: *Journal of Cosmology and Astroparticle Physics* 2013.08, pp. 036–036. arXiv: 1210.7652 [astro-ph, physics:hep-ex, physics:physics].

Nicolas, N., M. Rigault, Y. Copin, R. Graziani, G. Aldering, M. Briday, Y.-L. Kim, J. Nordin, S. Perlmutter, and M. Smith (May 2021). "Redshift Evolution of the Underlying Type Ia Supernova Stretch Distribution". In: *Astronomy & Astrophysics* 649, A74.

Nightingale, James., Richard Hayes, and Matthew Griffiths (Feb. 2021). "PyAutoFit: A Classy Probabilistic Programming Language for Model Composition and Fitting". In: *Journal of Open Source Software* 6.58, p. 2550.

Nightingale, James W *et al.* (n.d.). "PyAutoGalaxy: Open-Source Multiwavelength Galaxy Structure & Morphology". In: ().

Nugent, Peter E. *et al.* (Dec. 2011). "Supernova 2011fe from an Exploding Carbon-Oxygen White Dwarf Star". In: *Nature* 480.7377, pp. 344–347. arXiv: 1110.6201 [astro-ph].

Perlmutter, S. *et al.* (June 1999). "Measurements of Omega and Lambda from 42 High-Redshift Supernovae". In: *The Astrophysical Journal* 517.2, pp. 565–586. arXiv: astro-ph/9812133.

Phillips, M. M. (Aug. 1993). "The Absolute Magnitudes of Type IA Supernovae". In: *The Astrophysical Journal* 413, p. L105.

Popovic, Brodie, Dillon Brout, Richard Kessler, and Daniel Scolnic (Dec. 2021). *The Pantheon+ Analysis: Forward-Modeling the Dust and Intrinsic Colour Distributions of Type Ia Supernovae, and Quantifying Their Impact on Cosmological Inferences*. arXiv: 2112.04456 [astro-ph].

Pruzhinskaya, M V, A K Novinskaya, N Pauna, and P Rosnet (Nov. 2020). "The Dependence of Type Ia Supernovae SALT2 Light-Curve Parameters on Host Galaxy Morphology". In: *Monthly Notices of the Royal Astronomical Society* 499.4, pp. 5121–5135.

Rest, A. *et al.* (Oct. 2014). "COSMOLOGICAL CONSTRAINTS FROM MEASUREMENTS OF TYPE Ia SUPERNOVAE DISCOVERED DURING THE FIRST 1.5 Yr OF THE Pan-STARRS1 SURVEY". In: *The Astrophysical Journal* 795.1, p. 44.

Riess, Adam G. *et al.* (Sept. 1998). "Observational Evidence from Supernovae for an Accelerating Universe and a Cosmological Constant". In: *The Astronomical Journal* 116.3, pp. 1009–1038.

Riess, Adam G. *et al.* (July 2022). "A Comprehensive Measurement of the Local Value of the Hubble Constant with 1 Km/s/Mpc Uncertainty from the Hubble Space Telescope and the SH0ES Team". In: *The Astrophysical Journal Letters* 934.1, p. L7. arXiv: 2112.04510 [astro-ph].

Rigault, M. *et al.* (Dec. 2020). "Strong Dependence of Type Ia Supernova Standardization on the Local Specific Star Formation Rate". In: *Astronomy & Astrophysics* 644, A176.

Rodney, Steven A. *et al.* (June 2014). "TYPE Ia SUPERNOVA RATE MEASUREMENTS TO REDSHIFT 2.5 FROM CANDELS: SEARCHING FOR PROMPT EXPLOSIONS IN THE EARLY UNIVERSE". In: *The Astronomical Journal* 148.1, p. 13.

Schlafly, E. F. *et al.* (Apr. 2016). "THE OPTICAL–INFRARED EXTINCTION CURVE AND ITS VARIATION IN THE MILKY WAY". In: *The Astrophysical Journal* 821.2, p. 78.

Scolnic, D. *et al.* (Dec. 2015). "SUPERCAL: CROSS-CALIBRATION OF MULTIPLE PHOTOMETRIC SYSTEMS TO IMPROVE COSMOLOGICAL MEASUREMENTS WITH TYPE Ia SUPERNOVAE". In: *The Astrophysical Journal* 815.2, p. 117.

Scolnic, D. M. *et al.* (May 2018). "The Complete Light-curve Sample of Spectroscopically Confirmed Type Ia Supernovae from Pan-STARRS1 and Cosmological Constraints from The Combined Pantheon Sample". In: *The Astrophysical Journal* 859.2, p. 101. arXiv: 1710.00845 [astro-ph].

Scolnic, Dan *et al.* (Oct. 2022). "The Pantheon+ Analysis: The Full Dataset and Light-Curve Release". In: *The Astrophysical Journal* 938.2, p. 113. arXiv: 2112.03863 [astro-ph].

Smith, Mathew *et al.* (Aug. 2012). "THE SDSS-II SUPERNOVA SURVEY: PARAMETERIZING THE TYPE Ia SUPERNOVA RATE AS A FUNCTION OF HOST GALAXY PROPERTIES". In: *The Astrophysical Journal* 755.1, p. 61.

Thorp, Stephen, Kaisey S Mandel, David O Jones, Sam M Ward, and Gautham Narayan (Oct. 2021). "Testing the Consistency of Dust Laws in SN Ia Host Galaxies: A BAYESN Examination of Foundation DR1". In: *Monthly Notices of the Royal Astronomical Society* 508.3, pp. 4310–4331.

Thrane, Eric and Colm Talbot (2019). "An Introduction to Bayesian Inference in Gravitational-Wave Astronomy: Parameter Estimation, Model Selection, and Hierarchical Models". In: *Publications of the Astronomical Society of Australia* 36, e010. arXiv: 1809.02293 [astro-ph].

Tripp, Robert (n.d.). "A Two-Parameter Luminosity Correction for Type Ia Supernovae". In: ().

Vehtari, Aki, Andrew Gelman, Tuomas Sivula, Pasi Jylänki, Dustin Tran, Swupnil Sahai, Paul Blomstedt, John P. Cunningham, David Schiminovich, and Christian Robert (Nov. 2019). *Expectation Propagation as a Way of Life: A Framework for Bayesian Inference on Partitioned Data*. arXiv: 1412.4869 [stat].

Wang, X. *et al.* (July 2009). "IMPROVED DISTANCES TO TYPE Ia SUPERNOVAE WITH TWO SPECTROSCOPIC SUBCLASSES". In: *The Astrophysical Journal* 699.2, pp. L139–L143.

Wiseman, P., M. Sullivan, M. Smith, and B. Popovic (Feb. 2023). *Further Evidence That Galaxy Age Drives Observed Type Ia Supernova Luminosity Differences*. arXiv: 2302.05341 [astro-ph].

Wojtak, Radosław and Jens Hjorth (Aug. 2022). "Intrinsic Tension in the Supernova Sector of the Local Hubble Constant Measurement and Its Implications". In: *Monthly Notices of the Royal Astronomical Society* 515.2, pp. 2790–2799. arXiv: 2206.08160 [astro-ph].

Wojtak, Radosław, Jens Hjorth, and Christa Gall (Aug. 2019). "Magnified or Multiply Imaged? – Search Strategies for Gravitationally Lensed Supernovae in Wide-Field Surveys". In: *Monthly Notices of the Royal Astronomical Society* 487.3, pp. 3342–3355.

Wojtak, Radosław, Jens Hjorth, and Jacob Osman Hjortlund (Feb. 2023). *Two-Population Bayesian Hierarchical Model of Type Ia Supernovae*. arXiv: 2302.01906 [astro-ph].